



## **Deliverable D4.1.2 – Innovations on component level (interim report)**

**Partners WP4 Task 4.1**  
**LUH, WMC, AAU, FhG-H, DTU, FhG-DA, UOL, FhG-KS, RAW**

**August, 2014**

<b>Agreement n.:</b>	<b>308974</b>
<b>Duration</b>	<b>November 2012 – October 2017</b>
<b>Co-ordinator:</b>	<b>Danmarks Tekniske Universitet</b>
<b>Supported by:</b>	



The research leading to these results has received funding from the European Community's Seventh Framework Programme FP7-ENERGY-2012-1-2STAGE under grant agreement No. 308974 (INNWIND.EU).

---

### **PROPRIETARY RIGHTS STATEMENT**

This document contains information, which is proprietary to the "INNWIND.EU" Consortium. Neither this document nor the information contained herein shall be used, duplicated or communicated by any means to any third party, in whole or in parts, except with prior written consent of the "INNWIND.EU" consortium.

---

# Document information

<b>Document Name:</b>	Deliverable D4.1.2. – Innovations on component level (interim report)
<b>Confidentiality Class</b>	Public
<b>Document Number:</b>	Deliverable D 4.1.2
<b>Author:</b>	Niklas Scholle, Luka Radulović (LUH) Tim Westphal (WMC) Lars Bo Ibsen (AAU) Martin Kohlmeier (FhG-H) Vladimir Fedorov, Maria Sanz (DTU) Jennifer Pöllmann (FhG-DA) Bernd Kuhnle (UOL) Philipp Brosche (FhG-KS) Thomas von Borstel (RAW)
<b>Review:</b>	Niklas Scholle, Luka Radulović
<b>Date:</b>	2014-08-31
<b>WP:</b>	4 Offshore Foundations and Support Structures
<b>Task:</b>	4.1 Innovations on component level for bottom-based structures

## 1 TABLE OF CONTENTS

Partners WP4 Task 4.1 LUH, WMC, AAU, FhG-H, DTU, FhG-DA, UOL, FhG-KS, RAW .....	1
August, 2014 .....	1
<b>1 Table of contents.....</b>	<b>3</b>
<b>2 Introduction .....</b>	<b>6</b>
References.....	6
<b>3 Innovative Material.....</b>	<b>7</b>
References.....	7
3.1 Sandwich material for tubes (LUH) .....	8
3.1.1 Bearing capacity of sandwich cylinder .....	8
Axial load bearing capacity .....	8
Ductility Behaviour of Sandwich components with UHPC core.....	9
Bending load bearing capacity .....	10
Plastic moment capacity .....	11
Elastic moment capacity .....	12
Bond behaviour under bending.....	14
3.1.2 Conclusion .....	16
References.....	17
3.2 Sandwich material for connections and joints (WMC) .....	18
3.2.1 Experimental programme on bonded steel joints .....	18
3.2.2 Experimental Results .....	20
3.2.3 Discussion of the potential of bonded joints .....	24
3.2.4 Conclusions and recommendations.....	24
References.....	25
<b>4 Soil &amp; foundation.....</b>	<b>26</b>
4.1 Suction-bucket foundations (AAU).....	28
4.1.1 Identification and discussion of innovations on component level .....	28
4.1.2 Preliminary studies of innovations on component level .....	36
4.1.3 Results presentation .....	41
4.1.4 Interim conclusion and assumed impact of innovations on component level .....	43
4.1.5 Required experimental investigations on innovations on component level .....	49
REFERENCES .....	49
4.2 Soil-structure interaction / axial pile loading (FhG-H) .....	52
4.2.1 Motivation .....	52
4.2.2 Approach.....	52
4.2.3 A support structure model for time domain analysis (Model A) .....	52
4.2.4 A finite element model of the pile foundation for quasi static analyses (Model B).....	54
4.2.5 Numerical model verification.....	56
4.2.6 Identification and discussion of innovations on component level .....	58
4.2.7 Interim conclusion and assumed impact of innovations on component level .....	58
4.2.8 Required experimental investigations on innovations on component level .....	59
References.....	61
4.3 Innovative Foundations (DTU) .....	62
4.3.1 Piles for Jackets.....	62

Loads experienced by the piles .....	62
Possible innovations based on the problem definition .....	63
Aeroelastic model of the reference wind turbine on jacket foundation .....	64
Results comparing piles with Plugs versus unplugged piles .....	66
Conclusions on Piles for Jackets at 10 MW .....	69
4.3.2 Universal Articulated Joint as an innovative foundation .....	70
MOORING SYSTEM .....	70
Articulated Joint .....	71
Platform Assembly .....	74
CYLINDER .....	74
BUOYANCY CHAMBER .....	75
Conclusions regarding the floating spar with the universal joint .....	76
Required experimental investigations on innovations on component level .....	76
References .....	76
<b>5 Load mitigation .....</b>	<b>77</b>
References .....	77
5.1 Passive damping devices (FhG-DA) .....	78
5.1.1 Identification and discussion of innovations on component level .....	78
5.1.2 Preliminary studies of innovations on component level .....	79
Fitted Model Parameters .....	80
Modal Analysis and model comparison .....	81
Model Comparison with Modal Assurance Criterion .....	83
Design of the Vibration Absorber .....	84
Model with Vibration Absorber .....	84
5.1.3 Interim conclusion and assumed impact of innovations on component level .....	85
Modal Analysis of the Model with Vibration Absorber .....	85
Harmonic Response Analysis of the Model with Vibration Absorber .....	86
5.1.4 Required experimental investigations on innovations on component level .....	89
References: .....	89
5.2 Semi-active and active damping devices (UOL) .....	90
5.2.1 Identification and discussion of innovations on component level .....	90
Implementation of the reference structure in GH Bladed .....	90
Tower and Rotor-Nacelle-Assembly .....	90
Analysis of dynamic behaviour and comparison with other codes .....	91
Results .....	91
Total structure (coupled modes) .....	93
Reference control for the reference turbine .....	94
Aero-elastic simulations of the reference structure in GH Bladed .....	95
Influence of natural frequency on fatigue loading .....	96
Share of wind and wave loading of the overall fatigue damage .....	97
5.2.2 Identification of innovations .....	99
5.2.3 Preliminary studies of innovations on component level .....	100
Comparison of old and new reference control .....	100
Control features .....	101
5.2.4 Interim conclusion and assumed impact of innovations on component level .....	102
References .....	102

5.3	Load-mitigating controls (FhG-KS).....	104
5.3.1	Speed exclusion zone.....	104
5.3.2	Peak Shaving.....	104
5.3.3	Active tower damping.....	107
	References.....	111
<b>6</b>	<b>Manufacturing (Ramboll) .....</b>	<b>113</b>
6.1	Jacket Transition Piece Concepts.....	113
6.1.1	Evaluation .....	117
6.1.2	Concept Study.....	118
6.1.3	Conclusion .....	121
6.2	Jacket Assembly Concepts and Cost Optimization.....	122
6.2.1	Fabrication cost model.....	122
6.2.2	Assembly concepts.....	124
6.2.3	Conclusion .....	125

## 2 INTRODUCTION

Levelised cost of energy (LCOE) is one of the main decision drivers for or against offshore wind exploitation. Recent projects indicated actual LCOEs of around 165 € per MWh [2-01]. A reduction is highly desired, if not even necessary, for a further deployment of offshore wind energy. A study by the Crown Estate [2-01] indicates possible reduction up to under 100 € per MWh until 2020, which would be a reduction of 37.5%. Various fields were identified, which might contribute achieving this goal. Innovations regarding the support structure were one of those. Therefore, a reduction of costs of at least 20% is aimed for in the description of work during the course of this project [2-02] to significantly contribute to the realisation of the goal in cost reduction. Furthermore, risks and possibilities will be assessed.

The prospects of completely new concepts are expected to be minor, wherefore the focus in task 4.1. is on "Innovations on component level". Relevant topics for future cost-effective, mass-producible designs were identified, such as new foundation types (without grout and/or piling), soil-structure-interaction of large piles or suction buckets, innovative transition piece designs or designs using hybrid materials never employed in wind energy before. In addition, design integration using jacket-specific controls and innovative fabrication and installation processes shall complete the overall cost saving potentials.

The following fields of interest, illustrated by, are found in the sections of this report:

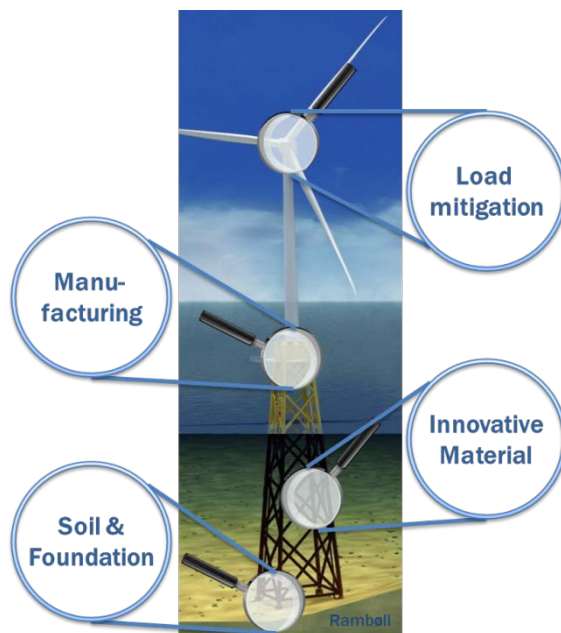


Figure 2.1-1: Subfields in task 4.1.

### Innovative materials:

Hybrid materials, such as sandwich structures are introduced in section 3 by the partners Leibniz University of Hannover (LUH) and Knowledge Centre Wind turbine Materials and Constructions (WMC).

### Soil & foundation:

Improvements in the modelling and numerical simulation of the soil structure interaction as well as innovative support structure and foundation designs are treated in section 4 by the Fraunhofer Institute IWES Hannover (FhG-H), the Danish Technical University (DTU) and Aalborg University (AAU).

### Load mitigation:

Concepts for load mitigation, such as jacket-specific and structural control are investigated in section 5 by the Fraunhofer Institutes LBF Darmstadt (FhG-DA) and IWES Kassel (FhG-KS), as well as by the Danish Technical University (DTU) and ForWind Oldenburg (UOL).

### Manufacturing:

Rambøll (RAMBOLL) is focusing on innovations in manufacturing, mass-production and installation in section 6.

The references used in the partners' contributions are listed directly subsequent to the particular subsection.

## References

- [2-01] The Crown Estate, "Offshore Wind Cost Reduction: Pathways Study", 2012  
 [2-02] InnWind.eu, "Annex I - "Description of Work"", Grant agreement no: 308974, 2012

### 3 INNOVATIVE MATERIAL

The goal of section 3 is the investigation of innovative hybrid materials with the aim of cost reduction through reduced material use and reduced fabrication costs. Reducing material use requires optimization of material use and the use of materials with higher loading capacity. High strength steels can withstand higher stresses and enable the use of thinner walled members. However, the minimum wall thickness does not only depend on the allowable stress, but also on the resistance against buckling or wrinkling. A way to circumvent this limit is to move to a sandwich structure especially with regard to large water depths and longer span width of chords and braces.

Another challenge when moving to higher strength materials is to achieve sufficient joint strength. Often the joints are the critical parts in a truss structure, especially when considering fatigue loading. In a welded structure the fatigue life of the structure is commonly governed by the fatigue life of the welds. Welding also proposes a challenge in the use of high strength steels, as the weld fatigue strength hardly improved for higher strength steels. Therefore, to utilize the higher (fatigue) strength of such steels better joining methods have to be developed.

University of Hannover (LUH) is focusing on numerical and experimental investigation of sandwich tubes of as well as on developing pre-design methods for sandwich tubes and their application on the chords and braces of the INN WIND.EU reference jacket design [3-01]. In the present deliverable the previously developed methods for the estimation of bearing capacity of sandwich towers for wind energy converters are presented, see Keindorf [3-02]. These methods represent the starting point for investigation of the bearing capacity of chord and braces of the jacket in Innwind.eu project. In addition, the investigations of ductility behaviour of sandwich components with an ultra-high performance concrete (UHPC) core carried out by Lindschulte in [3-03] are discussed.

While sandwich tubular construction can provide a structurally efficient solution by circumventing buckling limits, joining of sandwich steel structures provides a challenge. The aim of the preliminary experimental program of WMC is to evaluate the potential of bonded joints for joining tubular steel sections. For this purpose static and fatigue experiments are performed on bonded steel specimens.

#### References

- [3-01] INN WIND.EU Design report - Reference Jacket, "InnWind\_DesignReport\_ReferenceJacket\_Rev00.docx", Internal teamsite, uploaded 2014-01-16, accessed 2014-08-12
- [3-02] Keindorf, C., "Tragverhalten und Ermüdungsfestigkeit von Sandwichtürmen für Windenergieanlagen", Dissertation, Institute for Steel Construction, Leibniz University Hannover, 2010, (in German).
- [3-03] Lindschulte, N., "Drucktragverhalten von Rohren aus Ultrahochfestem Beton mit Stahlblechummantelung", Dissertation, Institute of Building Materials Science, Leibniz University Hannover, 2013, (in German).

### 3.1 Sandwich material for tubes (LUH)

To be suitable for use as structural components of supporting structures of OWT, sandwich tubes must have bearing capacity comparable to those of steel tubes. Considering that the present European and national codes are not covering fully this type of structural element, general methods for estimating the bearing capacity of different types of sandwich tubes developed in Keindorf [LUH01] will be presented in this deliverable. Additionally, outcomes of these methods applied to a 90 m high tower for wind turbines with an outer diameter of 5.5 m, constructed with different types of sandwich tube (Figure 3.1-2), will be shown. In addition to different types of core material, different steel grades (S235, S355, S460 and S690) of steel used for the outer and inner face of sandwich tubes, have been used in Keindorf [LUH01]. The aim was to determine which combination of core material and steel grade would lead to the greatest benefits in terms of bearing capacity (and afterwards stability) of the tower. The methods developed in Keindorf [LUH01] represent the starting point for investigating bearing capacity of chord and braces of the jacket in Innwind.eu project.

Additionally the present deliverable contains results from the investigation of ductility behaviour of Sandwich components with an ultra-high performance concrete (UHPC) core carried out by Lindschulte in [LUH02].

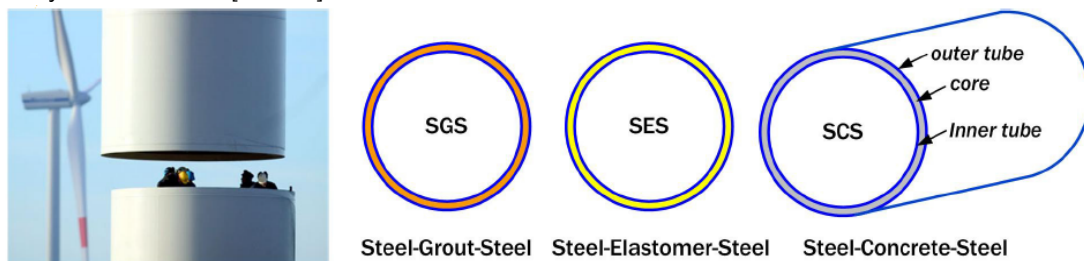


Figure 3.1-1: Steel and different types of sandwich structures for towers

#### 3.1.1 Bearing capacity of sandwich cylinder

##### Axial load bearing capacity

Based on EN 1994-1-1, which gives design rules for steel and concrete composite structure, the following expression have been used in Keindorf [LUH01] to estimate the axial load bearing capacity of sandwich structures:

$$N_{pl,Rk} = A_{-1} * f_{ck,-1} + A_0 * f_{ck,0} + A_1 * f_{ck,1} \quad \text{Eq. 3.1-1}$$

where:

- $N_{pl,Rd}$  - Axial capacity of fully plasticized sandwich section
- $A_{-1}$  - Cross-sectional area of the inner steel face
- $A_{+1}$  - Cross-sectional area of the outer steel face
- $A_0$  - Cross-sectional area of the core
- $f_{ck,-1}$  - Characteristic strength of steel of the inner steel face
- $f_{ck,+1}$  - Characteristic strength of steel of the outer steel face
- $f_{ck,0}$  - Characteristic strength of core material

The outcomes of the application of Eq. 3.1-1 on a cross-section of the steel and sandwich tower with a length of  $H = 90$  m and an outer diameter of  $D = 5.5$  m, are given in Table 3.1-1. The thickness of the steel tubes as well as the thicknesses of the layers of the sandwich tubes can be found also in Table 3.1-1. The considered cross section represents the bottom section of the wind turbine tower developed in Keindorf [LUH01].

**Table 3.1-1: Comparison of the axial load bearing capacity of steel and sandwich cylinders (taken from [LUH01])**

Cross-section	$M_{pl,Rk}$ according to Eq. 3.1-7 in [MNm]			
	S235	S355	S460	S690
Steel type	S235	S355	S460	S690
Steel thickness $t_{st}$ [mm]	50	32	24	16
ST	184 (100%)	190 (103%)	190 (104%)	190 (104%)
Layer thickness $t_{-1}/t_0/t_{+1}$ [mm]	24/80/24	16/80/16	12/80/12	8/80/8
SES ( $f_{ck,0} = 18$ MPa)	207 (112%)	211 (107%)	211 (115%)	211 (115%)
SGS ( $f_{ck,0} = 100$ MPa)	318 (173%)	322 (125%)	322 (175%)	322 (175%)
SCS ( $f_{ck,0} = 50$ MPa)	251 (136%)	255 (139%)	255 (139%)	255 (139%)

An increase of the bearing capacity of the sandwich sections with respect to the steel ones can be observed. This increase reaches 75% in case of sandwich cylinder with grout core and with steel type S690 (SGS 690 in Table 3.1-1). Anyway these values are obtained without considering stability problems of the tubes which would reduce the bearing capacity of the steel tubes, especially on the case of S460 and S690 due to their small thickness.

#### Ductility Behaviour of Sandwich components with UHPC core

Ultra-high performance concrete (UHPC) is characterized by compressive strength that is comparable to structural steel. This property can be used advantageous for lightweight thin-walled construction elements such as sandwich components. Hereby, a sufficient ductile behaviour is of crucial importance, which is not guaranteed because of the brittle fractural behaviour of plain UHPC. Based on experimental tests of thin-walled UHPC columns with hollow profile (steel-covered in- and outside), the axial load bearing behaviour could be determined in [LUH02]. Though, the investigations of Lindschulte [LUH02] were focussed on minimization of the steel cover, the experimental results can make a contribution on the Innwind.eu specific investigations.

**Table 3.1-2 Overview of the tube specimens from [LUH03]**

Specimen	steel outside			UHPC <sup>(1)</sup>			steel inside			$p_s$ (%) $A_s / A_c$
	$t_{s,o}$	$D_{s,o}$	$f_{y0.2}$ (N/mm <sup>2</sup> )	spacing (in points)			$t_{s,i}$	$D_{s,i}$	$f_{y0.2}$ (N/mm <sup>2</sup> )	
K-180-15-0.8	0.8	182	230	$t_{s,a}$	$D_{b,m}$	$D_{b,m}/t_b$	1.0	150	175	11
K-180-15-1.0	1.0	182	175	15	165	11	1.0	150	175	13
K-180-15-1.5	1.5	183	230	15	165	11	1.0	150	175	17
K-180-20-1.5	1.5	183	230	15	160	8	1.0	140	175	13
K-170-15-4.5	4.5	178	235	15	155	10	3.5	140	235	55

{1} UHPC: grain size: 0.5 mm; fom,cube: 210 N/mm<sup>2</sup> (heat treatment: 90 °C / 48 h)

The aim of the investigations documented in [LUH03] is to identify the percentage of steel which is necessary to serve as minimum covering for ductile structural behaviour of UHPC tube-constructions. Figure 3.1-2 and Figure 3.1-3 show the load bearing behaviour of the performed tube specimens under uniaxial load. With increasing steel thickness of the outer sheet, the residual strength level rises up from 300 kN to 600 kN (Figure 3.1-2). Within these percentages of steel there are obviously no influences to the ultimate load. This is also confirmed by the transverse strain values from the outer steel tube, measured using local strain gauges. Usage of a steel covers with comparatively larger thickness has led to an increase in the residual strength level as well as the ultimate load (Figure 3.1-3). The concrete core reaches approx. 30 % more than the uniaxial compressive strength of the concrete.

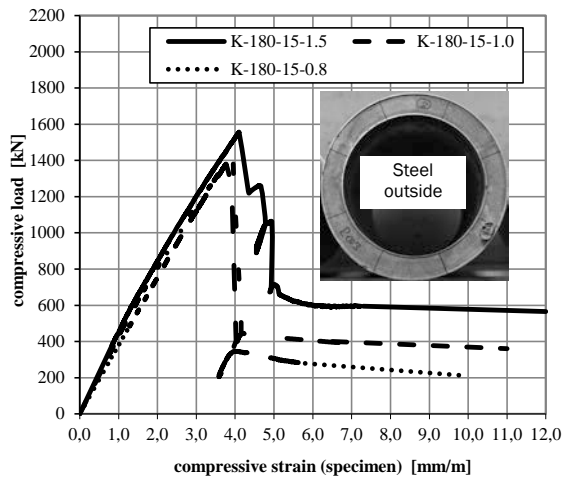


Figure 3.1-2: Load bearing behaviour - increasing thickness of steel ( $t_b$ : 15 mm,  $t_{s,o}$ : 0.8 to 1.5 mm) from [LUH03]

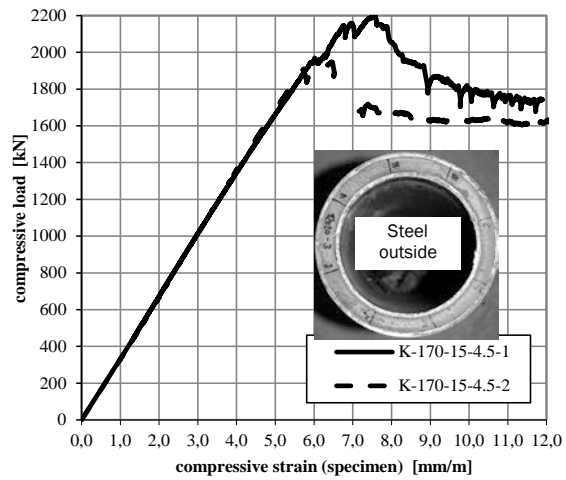


Figure 3.1-3: Load bearing behaviour of confined concrete tubes ( $t_b$ : 15 mm,  $t_{s,o}$ : 4.5 mm) from [LUH03]

To characterize the ductility of the specimens, an energy-based method according to [LUH05] can be used. The index  $I_5$  determines the ratio between the energy when the maximum load is arrived ( $x$ ) and the complete energy corresponding to the threefold of strain ( $3 \cdot x$ ). An index of  $I_5 = 5$  represents an ideal plastic material, while  $I_5 = 1$  corresponds to an ideal elastic-brittle behaviour. The details of this calculation are shown in Figure 3.1-4 for the specimen K180-20-1.5. The strain of the maximum load is determined assuming that the linear elastic behaviour is limited to approx.  $0.75 \cdot N_u$ .

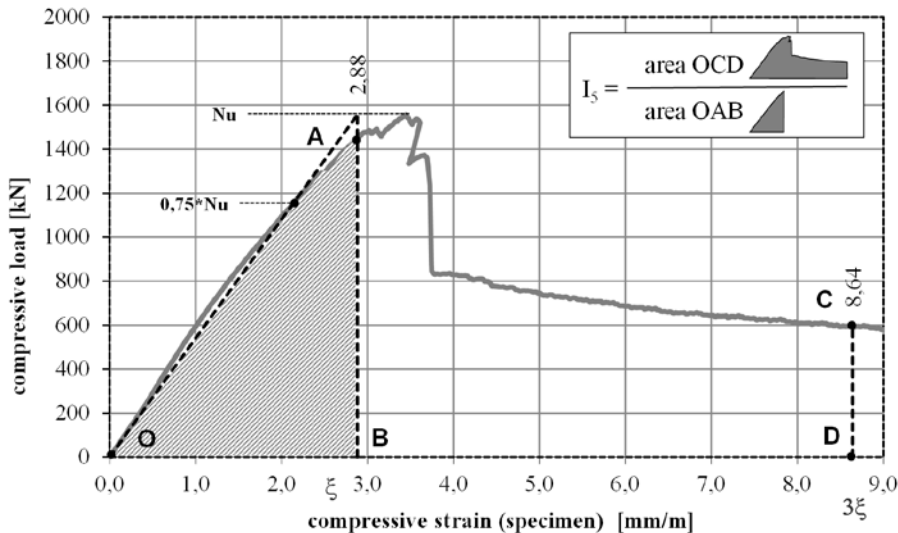


Figure 3.1-4: Calculation details for the Ductility index  $I_5$  [LUH05]; Specimen: K-180-20-1.5 from [LUH03]

The experimental results show a dependency between ductility index  $I_5$  and the arrangement of the internal and external steel plates. Lindschulte determines in [LUH02] that the necessary effective amount of steel  $(A_s \cdot f_y) / (A_c \cdot f_c)$  should be at least 35% to gain a ductile structural behaviour.

### Bending load bearing capacity

Besides axial load the bending moment has an important role in loading of onshore and offshore supporting structures. Although the present European and national codes (NORSOK

standard N-004 and DIN EN ISO 19902) define bearing capacity under bending load for grouted steel piles, in Keindorf [LUH01] has been demonstrated that the procedures defined in these codes cannot be applied to sandwich tubes. Therefore, Keindorf [LUH01] developed procedures in order to define correct plastic and elastic moment capacity of the sandwich cylinders. These procedures will be presented in the following subchapters together with the results obtained by applying them on a section of a wind turbine tower. In the same way the procedures will also be used to define of the bearing capacity of the chords and braces of the jacket defined in Innwind.eu project.

### Plastic moment capacity

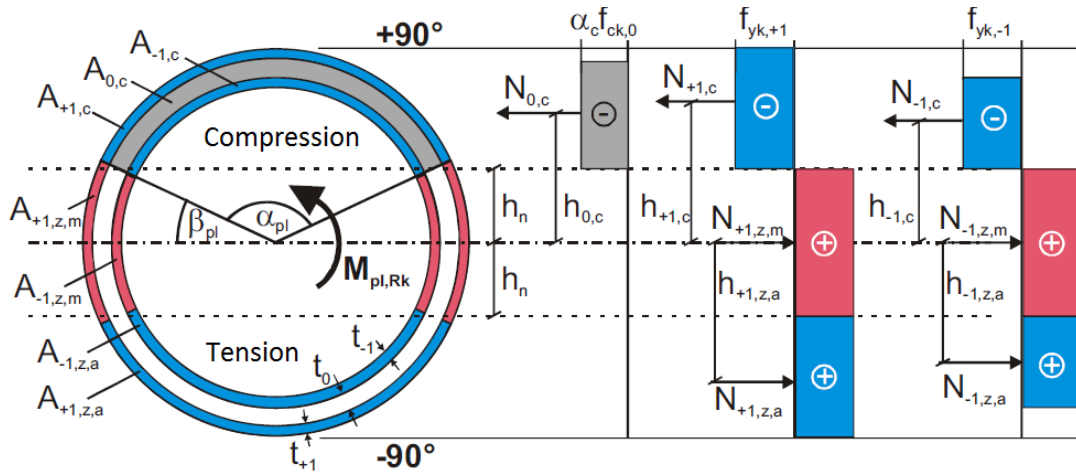


Figure 3.1-5: Fully plasticized cross section under bending load (taken from Keindorf [LUH01])

The Figure 3.1-5 shows a fully plasticized cross section of a sandwich cylinder under bending load. In order to have force equilibrium the total axial force has to be equal to zero:

$$\sum N = 0 = (N_{0,c} + N_{+1,c} + N_{-1,c}) - (N_{+1,z,m} + N_{-1,z,m} + N_{+1,z,a} + N_{-1,z,a}) \quad \text{Eq. 3.1-2}$$

Due to symmetry Eq. 3.1-2 can be simplified:

$$\sum N = 0 = (N_{0,c}) - (N_{+1,z,m} + N_{-1,z,m}) \quad \text{Eq. 3.1-3}$$

The cross sectional areas under tension and under compression along with the angle  $\alpha_{pl}$  which defines the neutral axis (Figure 1.1) can be calculated according to Eq. 3.1-4 and Eq. 3.1-5:

$$A_{i,c} = \frac{\pi}{4} * (D_i^2 - d_i^2) * \frac{\alpha_{pl}}{360} \quad \text{with } i = -1,0,1 \quad \text{Eq. 3.1-4}$$

$$\alpha_{pl} = \left[ \frac{A_0 * \alpha_c f_{ck,0}}{360 * (A_{+1} * f_{yk,+1} + A_{-1} * f_{yk,-1})} + \frac{2}{360} \right]^{-1} \quad \text{Eq. 3.1-5}$$

where:

$\alpha_c = 1$  – long-term load reduction factor assumed equal to 1 as in case of concrete-filled steel pipes

In order to determine the plastic bending moment of the cross section, the lever arms of already mentioned cross sectional areas (Figure 3.1-5) have to be calculated. This can be done according to Eq. 3.1-6.

$$h_{i,c} = \frac{30 * (D_i^3 - d_i^3)}{A_i} * \frac{1}{\alpha} * \sin\left(\frac{\alpha_{pl}}{2}\right) \quad \text{with } i = -1,0,1 \quad \text{Eq. 3.1-6}$$

Finally, the plastic moment capacity can be calculated with Eq. 3.1-7:

$$M_{pl,Rk} = \alpha_c f_{ck,0} * A_{0,c} * h_{0,c} + 2 * (f_{yk,+1} * A_{+1,c} * h_{+1,c} + f_{yk,-1} * A_{-1,c} * h_{-1,c}) \quad \text{Eq. 3.1-7}$$

The outcomes of the application of Eq. 3.1-7 on a cross-section of the steel and sandwich tower with a length of  $H = 90$  m and an outer diameter of  $D = 5.5$  m, are given in Table 3.1-3. As already mentioned, the considered cross section represents the bottom section of the wind turbine tower developed in Keindorf [LUH01]. An equivalent procedure can be applied also to the chords and braces of the Innwind.eu jacket.

**Table 3.1-3: Comparison of the plastic moment capacity of steel and sandwich cylinders (taken from Keindorf [LUH01])**

Cross-section	$M_{pl,Rk}$ according to Eq. 3.1-7 in [MNm]			
Steel type	S235	S355	S460	S690
Steel thickness $t_{st}$ [mm]	50	32	24	16
ST	319 (100%)	330 (103%)	331 (104%)	332 (104%)
Layer thickness $t_{-1}/t_0/t_{+1}$ [mm]	24/80/24	16/80/16	12/80/12	8/80/8
SES ( $f_{ck,0} = 18$ MPa)	331 (104%)	340 (107%)	341 (107%)	342 (107%)
SGS ( $f_{ck,0} = 100$ MPa)	389 (122%)	399 (125%)	400 (125%)	402 (126%)
SCS ( $f_{ck,0} = 50$ MPa)	358 (112%)	368 (115%)	369 (116%)	370 (116%)

An increase of the plastic bending moment of the sandwich sections with respect to the steel ones can be observed. This increase reaches 25% in case of sandwich cylinder with grout core and with steel type S355 (SGS 355 in Table 3.1-4). The positive effects are only due to the use of core materials as the steel thickness in the steel sections and sandwich section (considering the same steel type) remains almost the same.

However, the components of the supporting structures of wind turbines should always remain in the elastic range. Thus, the following subchapter will present a procedure for estimating elastic moment capacity of the sandwich sections, developed by Keindorf [LUH01].

### Elastic moment capacity

In Figure 3.1-6 the strain and stress distribution along a sandwich cross section under elastic bending load has been represented. In the case of elastic moment capacity only the most outer fibers of the outer steel face in the region under the tension reach yielding, see Figure 3.1-6 ( $f_{yk,+1}$  at point  $-90^\circ$ ). The stresses in the rest of the section can be obtained from the strain distribution, assuming valid Bernoulli-Hypotheses that flat surfaces remain flat.

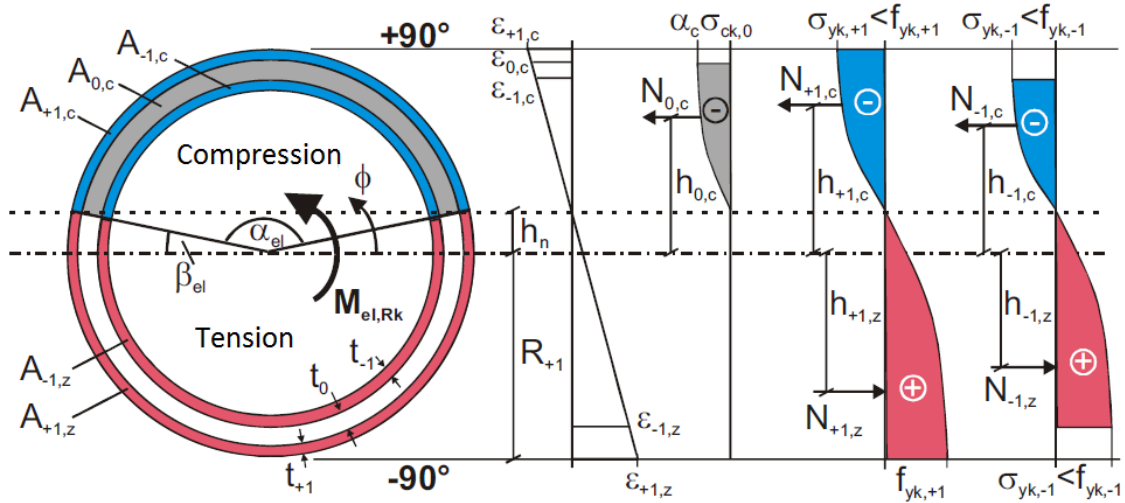


Figure 3.1-6: Strain and stress distribution along the cross section under elastic bending load (taken from Keindorf [LUH01])

As in the case of plastic moment capacity, due to equilibrium conditions, the total axial force has to be equal to zero:

$$\sum N = 0 = (N_{0,c} + N_{+1,c} + N_{-1,c}) - (N_{+1,z,m} + N_{-1,z,m}) \quad \text{Eq. 3.1-8}$$

In order to obtain the internal forces of the cross section given in Eq. 3.1-8, the stresses along the circular surfaces have to be integrated (Eq. 1.8).

$$N_{i,c}(\beta_{el}) = \frac{R_i^2 - r_i^2}{2} \int_{\beta_{el}}^{\pi - \beta_{el}} \sigma_i(\phi, \beta_{el}) d\phi \quad \text{with } i = -1, 0, 1 \quad \text{Eq. 3.1-9}$$

The stress distribution given as the function  $\sigma_i(\phi, \beta_{el})$  in Eq. 3.1-9, can be described as following:

$$\sigma_i(\phi, \beta_{el}) = \frac{\varepsilon_{i,z}(\beta_{el}) * E_i}{1 + \sin(\beta_{el})} * (\sin(\phi) - \sin(\beta_{el})) \quad \text{with } i = -1, 0, 1 \quad \text{Eq. 3.1-10}$$

As already mentioned, the stresses are derived from the strain distribution which is defined in relation to the yielding strain of the most outer fibers of the outer steel face in the region under the tension,  $\varepsilon_{+1,z}$  (Eq. 3.1-11).

$$\varepsilon_{i,z}(\beta_{el}) = \varepsilon_{+1,z} * \frac{R_i - R_i \sin(\beta_{el})}{R_{+1} - R_{+1} \sin(\beta_{el})} \quad \text{with } i = -1, 0, 1 \quad \text{Eq. 3.1-11}$$

The stress and strain distributions in Eq. 3.1-9 and Eq. 3.1-10 depend on the value of angle  $\beta_{el}$  which defines the position of the neutral axis. This angle must be derived through an iterative procedure applied to Eq. 3.1-8.

Finally, the elastic moment capacity of a sandwich section can be determined according to Eq. 3.1-12 and Eq. 3.1-13:

$$M_{el,Rk} = M_{el,+1} + M_{el,0} + M_{el,-1} \quad \text{Eq. 3.1-12}$$

$$M_{el,Rk} = \frac{R_{+1} + r_{+1}}{2} * N_{+1,c}(\beta_{el}) + \frac{R_0 + r_0}{2} * N_{0,c}(\beta_{el}) + \frac{R_{-1} + r_{-1}}{2} * N_{-1,c}(\beta_{el}) \quad \text{Eq. 3.1-13}$$

The entire derivation of the elastic moment capacity (according to Eq. 3.1-13) together with an iterative procedure for determining angle  $\beta_{el}$  has been developed in MathCAD by Keindorf [LUH01]. The outcomes of this MathCAD routine for the steel and sandwich section with an outer diameter of  $D = 5,5$  m are given in Table 3.1-4.

**Table 3.1-4: Comparison of the elastic moment capacity of steel and sandwich cylinders (taken from Keindorf [LUH01])**

Cross-section	$M_{pl,Rk}$ according to Eq. 3.1-13 in [MNm]			
	S235	S355	S460	S690
Steel type	S235	S355	S460	S690
Steel thickness $t_{st}$ [mm]	50	32	24	16
ST	250 (100%)	259 (104%)	260 (104%)	261 (104%)
Layer thickness $t_{-1}/t_0/t_{+1}$ [mm]	24/80/24	16/80/16	12/80/12	8/80/8
SES ( $f_{ck,0} = 18$ MPa)	241 (96%)	248 (99%)	249 (100%)	250 (100%)
SGS ( $f_{ck,0} = 100$ MPa)	276 (110%)	305 (122%)	320 (128%)	321(128%)
SCS ( $f_{ck,0} = 50$ MPa)	262 (105%)	284 (114%)	285 (114%)	286 (114%)

It can be observed that the sandwich sections with elastomer core have smaller elastic moment capacity than the steel sections. This is due to the fact that the stresses in the elastomer core are very small when the entire section is in elastic range. Thus, almost all stresses are distributed along the outer and inner steel face. Given that the outer diameter of all sections is the same, the outer and inner steel faces of the sandwich section have smaller elastic moment capacity than the corresponding steel section.

On the other hand, the sandwich sections with grout and concrete core show an increase of the elastic moment capacity with respect the one observed in the steel sections. The increase reaches 28% in case of sandwich cylinder with grout core and with steel type S460 (SGS 460 in Table 3.1-4). As in the case of the plastic moment capacity, this increment is due only to the use of core materials, since the total steel thickness in a sandwich section is equal to the thickness of the steel section with the same steel type.

### Bond behaviour under bending

Another important aspect that should be taken into account when dealing with sandwich cylinders under bending is the bond behaviour between the inner and outer steel face and the core material. This is particularly important in the region of the sandwich sections that are under pressure. In this region the core material participates in moment capacity of the section (Figure 3.1-6, area  $A_{0,c}$ ) and it should be ensured that it works together with the inner and outer steel face.

In Table 3.1-5 the difference between the stresses in the inner and outer steel face of already seen sandwich sections (SES, SGS and SCS) under the action of corresponding elastic bending moments from Table 1.2, is given. The given values represent the difference between stresses in the portion of the section under pressure – point  $+90^\circ$  in Figure 3.1-6. In order to have two steel faces working together, this difference should be balanced by a shear stress developed on the interface between the core material and the steel faces. The expected shear stress at the interface must be anyway smaller than the bond shear strength of the core material. In the following, the definition of this shear stress in a sandwich section of a wind turbine tower under bending load, developed in Keindorf [LUH01], will be presented. As in the case of previously described moment capacities, the obtained definition can be also applied to the chords and braces of the Innwind.eu jacket.

Table 3.1-5: Difference between the stress in the inner and outer steel face of the sandwich section (taken from Keindorf [LUH01])

Cross-section	Difference between the stresses in inner and outer steel face $\Delta\sigma_{+1,-1} = \sigma_{+1} - \sigma_{-1}$ in [MPa]							
	S235		S355		S460		S690	
Steel type	S235		S355		S460		S690	
Steel thickness $t_{st}$ [mm]	50		32		24		16	
ST	215	0	345	0	460	0	690	0
Layer thickness $t_{-1}/t_0/t_{+1}$ [mm]	24/80/24		16/80/16		12/80/12		8/80/8	
SES ( $f_{ck,0} = 18$ MPa)	216	9	333	12	445	15	668	22
SGS ( $f_{ck,0} = 100$ MPa)	225	9	345	12	460	15	690	22
SCS ( $f_{ck,0} = 50$ MPa)	216	9	333	12	444	16	668	22
	225		345		460		690	22

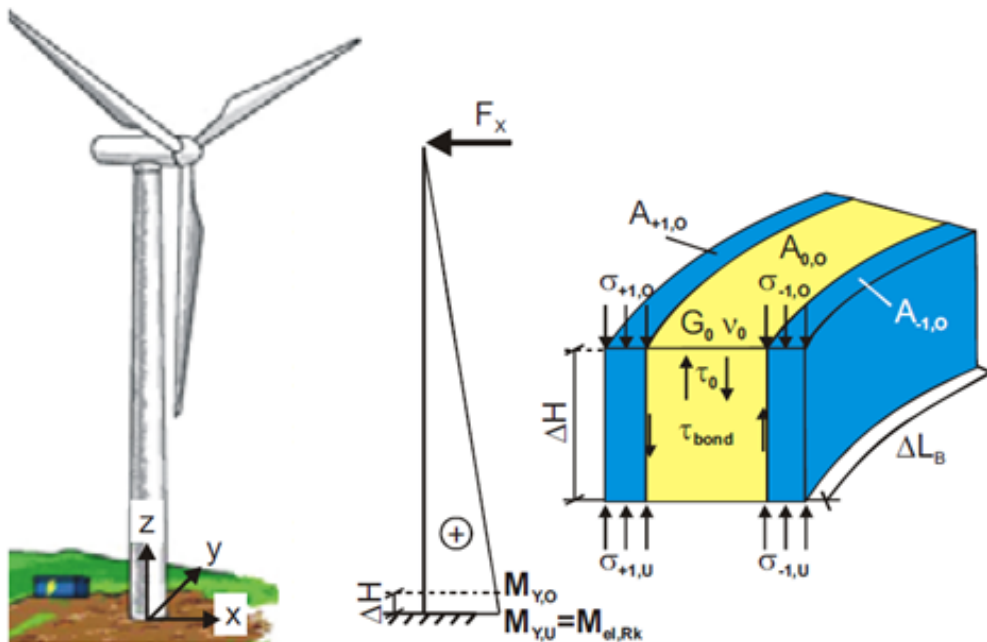


Figure 3.1-7: Bond stresses in a sandwich section of a wind turbine tower under bending load (taken from Keindorf [LUH01])

In Keindorf [LUH01], the shear stress on the interface has been determined by using the mechanical model depicted in Figure 3.1-7. The force  $F_x$  has been applied at the hub height so that the maximal elastic moment developed at the bottom section of the tower,  $M_{y,U} = M_{el,Rk}$  (Eq. 3.1-14)

$$M_{y,U} = F_x * H = M_{el,Rk} \quad \text{Eq. 3.1-14}$$

Subsequently, a unit portion of the tower's bottom with height  $\Delta H = 1$  and  $\Delta L_b = 1$  is considered (Figure 3.1-7 right). The bending moment at the height  $\Delta H$  can be calculated with Eq. 3.1-15.

$$M_{y,0} = M_{y,U} * \frac{H - \Delta H}{H} = M_{el,Rk} \quad \text{Eq. 3.1-15}$$

By using Eq. 3.1-16, the axial forces acting on the upper (O) and lower (U) section of the unit element can be determined and consequently the difference between the forces acting on the outer and inner steel face can be estimated (Eq. 3.1-17).

$$N_{i,j} = \sigma_{i,j} * A_{i,j} \quad \text{with } i = -1, +1 \text{ and } j = U, O \quad \text{Eq. 3.1-16}$$

$$\Delta N_{+1,-1} = \Delta N_U + \Delta N_O = (\Delta N_{+1,U} + \Delta N_{-1,U}) + (\Delta N_{+1,O} + \Delta N_{-1,O}) \quad \text{Eq. 3.1-17}$$

To equilibrate  $\Delta N_{+1,-1}$ , shear stress on the interfaces between the core material and steel faces develops. Considering that the area of the inner interface is smaller than the area of the outer one, a higher shear stress value can be observed on it. This stress can be calculated with Eq. 3.1-18.

$$\tau_{bond} = \frac{\Delta N_{+1,-1}}{A_{m,-1}} = \frac{\Delta N_{+1,-1}}{\Delta H * \Delta L_{B,-1}} \quad \text{Eq. 3.1-18}$$

**Table 3.1-6: Shear stress on the interface of the core material and the inner steel face according to Eq. 3.1-18 (taken from Keindorf [LUH01])**

Cross-section	Shear stress on the interface of the core material and the inner steel face according to Eq. 3.1-18 in [MPa]			
Steel type	S235	S355	S460	S690
Layer thickness $t_{-1}/t_0/t_{+1}$ [mm]	24/80/24	16/80/16	12/80/12	8/80/8
SES ( $f_{ck,0} = 18$ MPa)	0.79	0.75	0.72	0.68
SGS ( $f_{ck,0} = 100$ MPa)	0.76	0.71	0.69	0.66
SCS ( $f_{ck,0} = 50$ MPa)	0.76	0.72	0.69	0.66

In Table 3.1-6, values of the shear stress on inner interface of different sandwich sections are calculated according to Eq. 3.1-18. As already stated, the obtained shear stress must be smaller than the bond shear strength of the core material. For example, a grout material used for SGS 460 must have a bond shear strength greater than 0.69 MPa. Considering grouts given in Deliverable 4.1.1, the grout Densit Decorit S5 with  $\tau_{bond} = 3.64$  MPa clearly offers very good bonding behaviour for any considered SGS cylinder, whereas the grout MC S-Fix with  $\tau_{bond} = 0$  MPa can not be used as a core material due to non existing bond shear strength.

The necessary bond characteristics of core materials can be determined in the same way also for chords and braces of a jacket supporting structure. Thus, by applying the mechanical model given in Figure 3.1-7 and by calculating the shear stress according to Eq. 3.1-18 minimal requirements in terms of bond shear strength can be estimated.

### 3.1.2 Conclusion

As shown in the previous chapters, models/approaches describing the load bearing behaviour of sandwich structures already exist. However, they have been developed for thin-walled compression members [LUH02] or tower sections [LUH01] and do not consider any load combinations. The purposed application of the sandwich components in this research project as a brace or chord in a Jacket of a 10MW OWEC differs from the applications of the investigations of [LUH02] and [LUH01] and component-related load conditions have to be considered. The established structural models have to be checked considering the new purposed application. A Jacket as a substructure of an OWEC is characterized by special loading situations. Due to restraint moments a combination of moment and normal force appears in the brace and chord components. A model representing the bearing capacity of sandwich components under this specific load situation has not been established so far. As part of the project Innwind.eu such a model shall be investigated. To achieve this model, a test plan will be created and specimen of

sandwich components will be tested statically under eccentric compressive load. Using selected experimental tests accompanied by numerical investigations the structural behaviour of sandwich components under eccentric compressive load shall be described and a descriptive model approach shall be formulated.

## References

- [LUH01] Keindorf, C.: “Tragverhalten und Ermüdungsfestigkeit von Sandwichtürmen für Windenergieanlagen”, Dissertation, Institute for Steel Construction, Leibniz University Hannover, 2010, (in German).
- [LUH02] Lindschulte, N.: “Drucktragverhalten von Rohren aus Ultrahochfestem Beton mit Stahlblechummantelung”, Dissertation, Institute of Building Materials Science , Leibniz University Hannover, 2013, (in German).
- [LUH03] Lindschulte, N.; Lohaus, L.: Structural Behaviour of UHPC Tube-Constructions with Minimal Steel Covering, Proceedings of fib Symposium, Tel Aviv, 22.-24. April 2013, pp. 661-664
- [LUH04] Attard, M. M.; Foster, J. F.: Ductility of High Strength Concrete Columns, Uniciv Report 344, University of New South Wales, 1995, Sydney, Australia.

### 3.2 Sandwich material for connections and joints (WMC)

While sandwich tubular construction can provide a structurally efficient solution by circumventing buckling limits, joining of sandwich steel structures provides a challenge. This can be for practical reasons, e.g. because of the two faces welding may be impossible for the inner face, simply because it is inaccessible. But also the fatigue strength that can be achieved may be an even more limiting factor than it is for conventional welded steel structures. The circumvention of buckling limits raises the allowable stress levels for the structures, which will result in fatigue becoming a more dominant design driver. Therefore high strength joining methods are needed.

In [WMC01] bonded joints were identified as a promising joining method for sandwich tubular steel structures. An important reason is that the two face layers of the sandwich provide a large area for stress transfer. Bonded joints can be made in many configurations, using one or two sides of the surface layers for bonding, and can even be combined with welding, see Figure 3.2-1

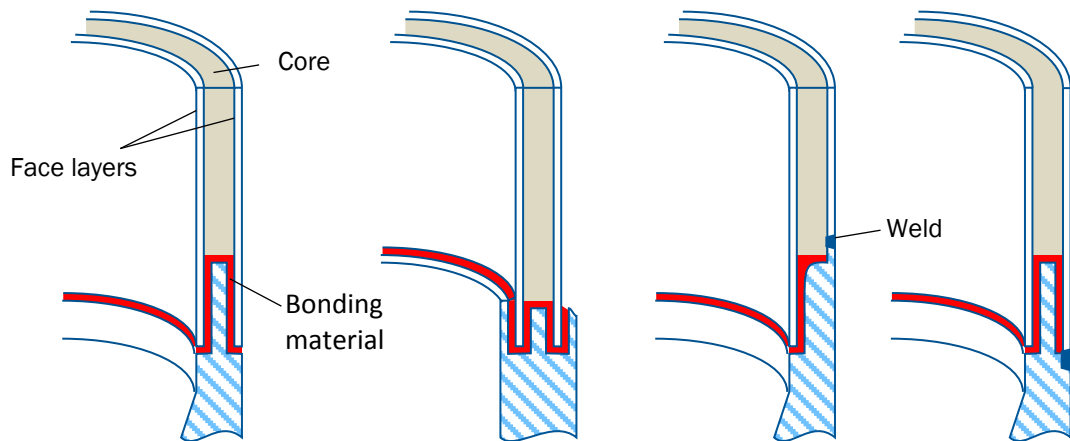


Figure 3.2-1: Joint concepts for sandwich steel structures

#### 3.2.1 Experimental programme on bonded steel joints

The aim of the preliminary experimental programme is to evaluate the potential of bonded joints for joining tubular steel sections. For this purpose static and fatigue experiments are performed on bonded steel specimens. In these experiments the load bearing capacity of bonded joints is evaluated, based on the achievable stress levels in the steel tubes. By comparing the stress levels in the steel tube the results can be related to joint strengths for e.g. welding.

For the experiments scaled single walled tubular specimens are used. The single walled geometry is used because of easy specimen fabrication and because the load bearing capacity of sandwich tubular joints is expected to be virtually identical to the load bearing capacity of the two individual walls.

The preliminary tests are based on tubes with 4 mm wall thickness and a bondline thickness of 5 mm. Overlap lengths are varied in the experiments. The nominal dimensions of the inner and outer tube are listed in Table 3.2-1. The specimen geometry is shown in Figure 3.2-2

Table 3.2-1: Nominal dimensions of the steel tubes

	Outer diameter	Wall thickness	Steel grade
Inner tube	82.5	4.0	S355J2H
Outer tube	101.6	4.0	S355J2H

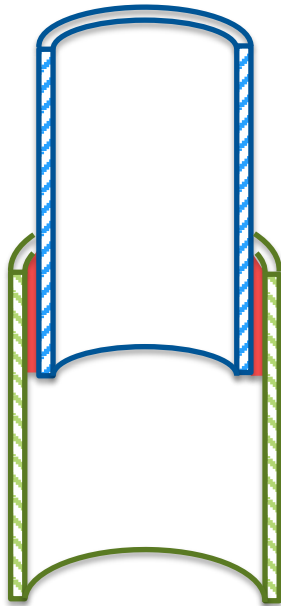


**Figure 3.2-2: Specimen geometry**

For the first experimental programme an epoxy based adhesive, Momentive EPIKOTE™ Resin MGS® BPR 135G-Series with EPIKURE™ Curing Agent MGS® BPH 134G-137G was used. This adhesive was selected because of the suitability for steel to steel bonding and because considerable experimental data on the mechanical properties was available from previous research.

The tubes for the specimens were cut to size and then machined in a lathe to assure perpendicularity of the faces. The tubes were grit blasted for surface preparation.

To assure concentric bonding of the specimens a disk was used inside the larger tube with a centring shoulder for the inner tube. Adhesive was then injected in the concentric cavity between the tubes. After injection a ring was used around the inner tube with a centring shoulder for the outer tube to assure concentricity at to other end of the joint.

Three bond geometries have been evaluated in the experiments. For the first tests series a 50 mm overlap length was used. The joints were finished with straight edges, without fillet. The second geometry used a 100 mm overlap length, again with straight edges. The third geometry again used a 50 mm overlap length, but now a

45° degree fillet of adhesive was used at both joint edges.

For the first geometry, with 50 mm overlap, the shape of the centring rings on either end of the joint resulted in a small recess of approximately one mm in the adhesive (the adhesive was slightly lower the ends of the steel tubes). After fabrication of these specimens the centring rings were adapted and a new series of specimens without recess was made.

For testing a 400 kN test machine and a 1000 kN test machine were used. The test setup is shown in Figure 3.2-3. On one end of the specimen a spherical washer was used to avoid the introduction of bending moment into the specimen. Thus the specimens were tested with pure axial loading.

The 400 kN maximum load capacity roughly corresponds with the static strength of the inner tube. At a nominal cross sectional area of 986 mm<sup>2</sup> a maximum load of 400 kN corresponds to a stress approximately of 400 MPa. The minimum yield strength for the steel is 355 MPa.

The preliminary experiments focus on the static and fatigue behaviour of the joints. The tests are done in compression. For the fatigue tests a load ratio (ratio of minimum to maximum load) of  $R = 10$  was used. For the shear stress on the adhesive this results in a stress ratio of  $R = 0.1$ , which it would also be in a tensile test setup with load ratio  $R = 0.1$ . Despite this the results of these compression tests are not expected to identical to what would be obtained in tensile tests, because of the different stress field at the joint edges and the poisson effect in the tubes. However, for tensile loading no large differences in load levels and fatigue behaviour are expected compared to compressive loading.



**Figure 3.2-3: Experimental setup**

### 3.2.2 Experimental Results

The static test results for all joint geometries are listed in Table 3.2-2. Next to the force and the shear stress in the tube, also the corresponding stress level in the inner steel tube is given. This stress level is used to quantify to what level the steel properties are utilized. Ideally the joint should not be the weakest point and failure should occur in the steel tube(s). The stress level in the steel tube can also be used to compare the performance of the joint to other joining methods, e.g. welding.

For 50 mm overlap the results of the two test series are given, the first series with a recess in adhesive and the second series with straight joint edges. Contrary to expectations the average strength of the specimens with straight edges is lower than the average strength of the specimens with recess. The cause of this difference is not yet known.

It can be seen that for the 50 mm overlap length the stress level in the tubes approaches the yield strength of the steel. For 100 mm overlap length indeed in some specimens failure (yielding) of the steel tube occurred, see Figure 3.2-4.



Figure 3.2-4: Yielding of the top tube

The fourth set of specimens has a bond geometry with again a 50 mm overlap of the steel tubes, but with a 45 degree fillet of the adhesive on either end of the joint, see Figure 3.2-5. For this test series no bond failure occurred for any of the specimens. All specimens exhibited yielding of the inner tube, after which the tests were stopped.

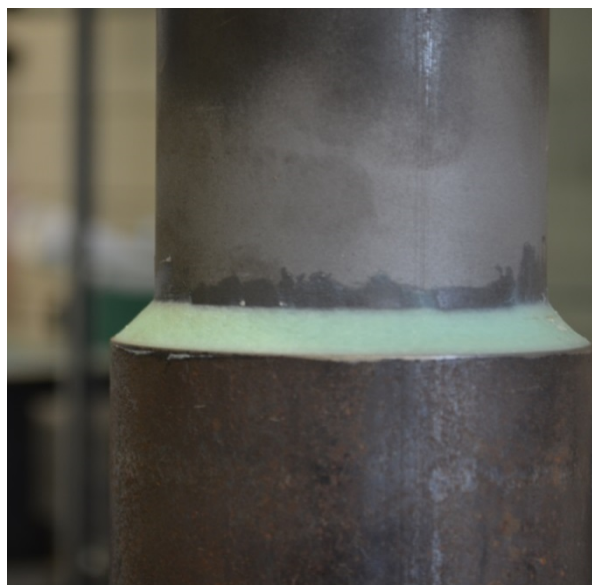
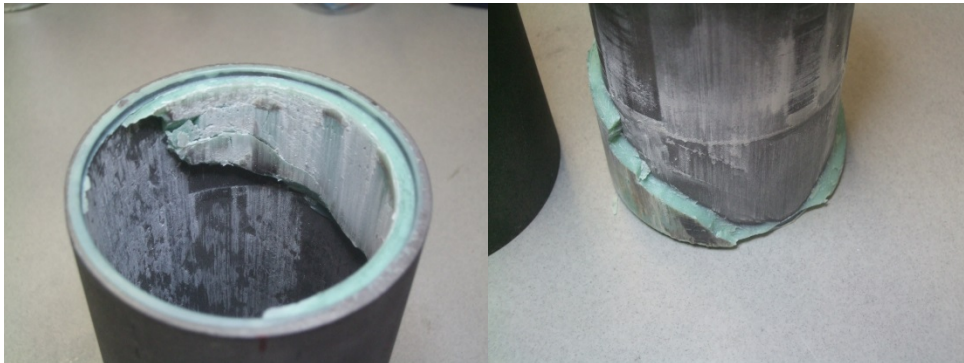


Figure 3.2-5: Specimen with 45 degree fillet

If failure of the bond occurred, the failure occurred at the surface of the steel tubes. A typical failure mode is shown in Figure 3.2-6. The failure at the steel surface indicates that the weakest part of the joint is the adhesion to of the epoxy bonding paste to the steel surface.

Table 3.2-2: Results of the static tests on bonded tubes.

Joint geometry / Specimen number	Load	Adhesive Shear stress	Inner tube stress	Remarks
	[kN]	[kN]	[MPa]	
<b>50mm overlap with recess</b>				
TB05HXIC02	239	18.6	246	
TB05HXIC03	244	19.3	251	
TB05HXIC04	303	23.0	314	
TB05HXIC20	264	19.2	270	
TB05HXIC23	296	21.9	308	
<b>Average</b>	<b>269</b>	<b>20.4</b>	<b>278</b>	
<b>50 mm overlap</b>				
TB05HXC05	247	19.0	251	
TB05HXC06	217	16.3	223	
TB05HXC15	205	15.9	213	
TB05HXC16	179	14.0	183	
TB05HXC19	245	19.1	255	
<b>Average</b>	<b>219</b>	<b>16.9</b>	<b>225</b>	
<b>100 mm overlap</b>				
TB010HXC10	400	15.8	397	No bond failure
TB010HXC11	326	13.6	340	
TB010HXC12	358	13.8	367	no bond failure
TB010HXC13	293	11.3	305	
TB010HXC21				not tested
<b>Average</b>	<b>344</b>	<b>13.6</b>	<b>352</b>	
<b>50 mm overlap with fillet</b>				
TB05HXFC25	351	27.2	346	No bond failure
TB05HXFC26	355	27.5	370	No bond failure
TB05HXFC27	357	28.1	365	No bond failure
TB05HXFC28	350	27.4	363	No bond failure
TB05HXFC29	356	28.1	371	No bond failure
<b>Average</b>	<b>354</b>	<b>27.7</b>	<b>363</b>	



**Figure 3.2-6: Typical failure mode for the bonded tubes**

For the evaluation of the fatigue performance of the joints fatigue experiments have been performed on specimens with 50 mm overlap length with straight edges. Tests have been completed at 3 load levels, with target cycle counts of 1,000, 100,000 and 1 million cycles. Two tests have been completed at each load level, 6 tests in total. The test results are listed in Table 3.2-3.

In Figure 3.2-7 the S-N curve based on these test results is given for the adhesive average shear stress plotted to the cycles to failure. The S-N curve based on the corresponding stress level in the inner tube is given in Figure 3.2-8. The slope of the S-N curve is very flat, with a slope parameter of 16. Given the limited number of experiments, the limited stress range over which is tested and the high scatter in fatigue life there is, however, a large uncertainty in this slope parameter.

**Table 3.2-3: Results of the fatigue tests on bonded tubes**

Joint geometry / Specimen number	Load	Adhesive Shear stress	Inner tube stress	Cycles to failure
	[kN]	[kN]	[MPa]	[-]
<b>50mm overlap</b>				
TB05HXF07	128	10.0	133	1305
TB05HXF08	103	8.0	104	10554
TB05HXF09	129	10.0	137	25
TB05HXF14	85	6.5	87	1095485
TB05HXF17	103	8.0	106	380392
TB05HXF18	84	6.5	86	37969

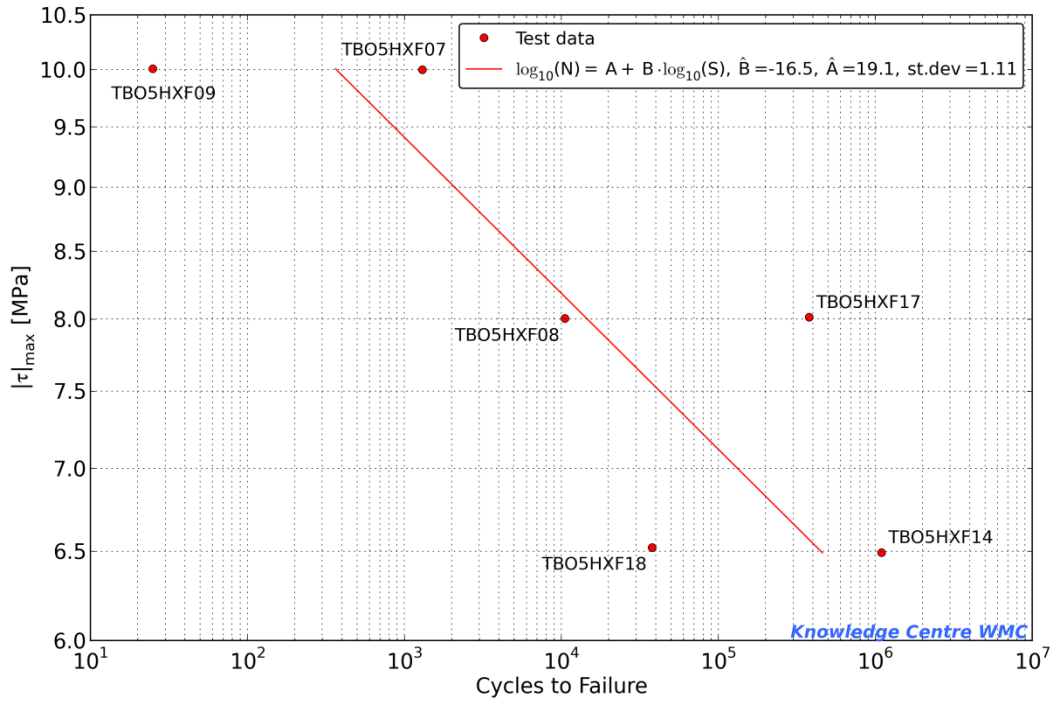


Figure 3.2-7: S-N curve based on the adhesive shear stress vs cycles to failure

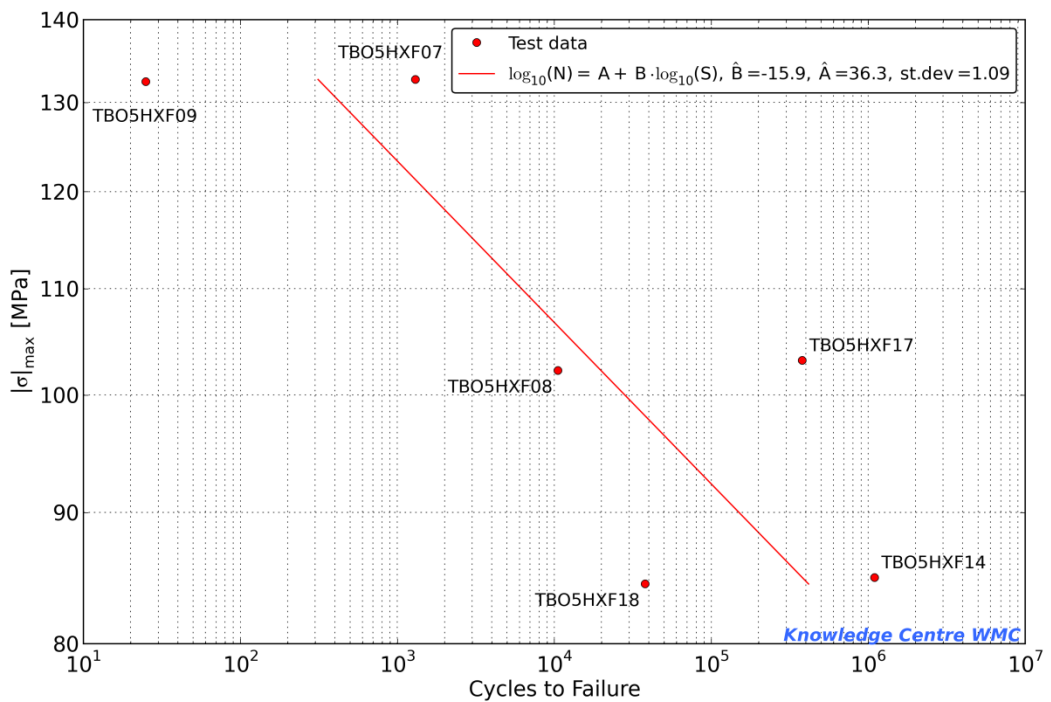


Figure 3.2-8: S-N curve based on stress in the steel tube vs cycles to failure

### 3.2.3 Discussion of the potential of bonded joints

The experiments show that the potential of bonding as a joining method for heavily loaded steel structures. When the static tests are considered it can be seen that already with a 50 mm overlap length considerable joint strength is achieved. With a stress level in the steel tubes in the order of 250 MPa the joint strength already approaches the yield strength of the steel tubes.

For further improvement of the joint strength changes to the bondline geometry to reduce stress concentrations proved more effective than increasing the overlap length. For the specimens with 100 mm overlap length in some cases the yield stress of the steel tubes was exceeded, but high scatter in the results was found. For the joint geometry with 50 mm overlap and fillet the joint strength exceeded the strength of the steel tube for all specimens. It should be noted that the scatter in the joint strength cannot be judged in this case, as no bond failures occurred. But these experiments showed that an efficient joint with full utilization of the load bearing capacity of the steel tubes can be achieved at an overlap to wall thickness ratio of  $\sim 1:10$ .

The experiments highlight the sensitivity of the joint strength to the geometry of the bondline. Going from a straight edge to a fillet give a considerable increase in joint strength. This sensitivity, and also the scatter in the test results of the specimens with straight edges, indicates that consistent manufacturing will be important to assure a consistent joint strength.

Also in the fatigue experiments promising results were achieved. Although the S-N curve from these experiments is considerably below e.g. the C class S-N for welded structures [WMC02], the experiments were performed on a preliminary, non-optimized joint geometry, which exhibited the poorest performance of the geometries tested in the static test series. Therefore it can be expected that a significant improvement of the fatigue performance can be achieved with an improved joint geometry.

Furthermore the S-N curve is very flat with a slope parameter of 16. Although there is still considerable uncertainty in this parameter because of the limited set of test results, this is a value that is not uncommon for composites. It is much flatter than the slope for welded joints, which is in the range from 3 to 5. Therefore bonded joints can be expected to perform especially well compared to welded joints at higher number of cycles. High cycle counts can be expected for offshore support structures, with the combination of wave and wind loading.

Up to now only a single adhesive has been used for the experiments. The current adhesive is an epoxy based adhesive. This adhesive has a relatively high stiffness and the material itself has a high strength, but it may be that adhesives based on another chemistry may have better adhesion to the steel surface. Also the high stiffness may have a detrimental effect on the joint strength. A lower stiffness adhesive may lead to a more even stress distribution and less sensitivity to stress concentrations.

In these series of experiments only axial loading was applied to the specimens, without any bending moments. Bending moments may have a detrimental effect on the performance of these joints. Bending of the joint may result in peel stresses at the edges of the joint which could lead to failure at lower stress levels.

### 3.2.4 Conclusions and recommendations

In the preliminary experiments described here the potential of bonding as a joining technique for tubular steel structures was evaluated. The results indicate that bonding could be a viable joining technique, with a static load bearing capacity that can exceed the strength of the steel tubes at acceptable overlap lengths. In these experiments single walled specimens were tested, for sandwich tubes it is expected that similar ratios of surface layer thickness to overlap length will be sufficient. The relatively thin surface layers will then be beneficial as they correspond to short overlap lengths.

A limited series of fatigue experiments was performed. There is considerable room for improvement and the experiments should be expanded to optimized joint geometries to truly

evaluate the potential in fatigue. The results indicate that the S-N curve for bonded joints is very flat. This needs to be confirmed with more experiments and experiments to higher number of cycles to increase the confidence on the S-N exponent.

Only a single adhesive was evaluated here and other adhesives need to be screened as there may well be adhesives that surpass the performance of the epoxy based adhesive used here. The adhesion to steel will affect the joint strength, but also the stiffness will be of importance as it will affect the stress concentrations at the joint edges. To investigate this influence and also for optimization of the joint geometry the work must be assisted by numerical modelling of the joint.

The behaviour under other loading conditions than pure axial loading needs to be investigated. For wind turbine support structures the loading will in practice always exist out of a combination of bending and axial loading. The sensitivity of the joints to a bending component therefore needs to be evaluated, both numerically and experimentally.

Finally, the behaviour in a sandwich construction needs to be investigated. Although the behaviour is not expected to be considerably different when applied to a sandwich structure, the different boundary conditions may affect the stress state at the joint edges and thus the strength of the joint. To investigate this, a numerical study should be able to provide considerable insight.

## References

[WMC01] INN WIND.EU Deliverable 4.1.1 – „Innovations on component level for bottom based structures“, October 2013

[WMC02] BS 7608-1993 – „Code of practice for Fatigue design assessment of steel structures“, 1993

## 4 SOIL & FOUNDATION

The development of innovative components of support structures for larger offshore wind turbines requires a broad understanding of the static and dynamic behaviour of the sub-structure and its components. Furthermore, the foundation and the soil behaviour are of special importance with regard to their underlying nonlinear and interacting processes. The soil-structure interaction is of major interest for the development of innovations with respect to the foundation design.

The processes in the pile-soil or bucket-soil interface and its surrounding zone are not yet fully understood in detail, which is caused by the fact that combined (horizontal and vertical) or cyclic loading effects, or acting pore water pressure are seldom considered simultaneously. Further investigations of the physically non-linear processes might result in better predictions and even limit the risk of capacity degradation over long term loading periods.

Innovations on component level usually result in foundation designs that are not yet fully captured by current rules and guidelines. Missing data has to be generated by numerical analyses and validated by experimental tests. The applicability of novel design methods and their underlying data and algorithms has to be validated for the application at larger scales. In a first step, the applicability and the potential advantage of innovations is evaluated and quantified by validated numerical modelling. The innovations on component level for soil and foundation are presented within the following three sections.

Suction bucket foundations are investigated with respect to their application in multi-pod type foundations. According to the resulting loading response of this type of support structure the suction bucket is analysed with focus on its compressive and tensile bearing capacity. Different methodologies for the bearing capacity estimation are presented. Furthermore, cyclic and monotonic pull-out tests at large models in the laboratory of Aalborg University are reported. With regard to the enhancement of the resistance to pull-out load, the potential of the developed testing rig and the objectives of further recommended tests are described in detail.

Frame type sub structures can be referred to as hydrodynamically transparent due to their low structural area to occupied volume ratio. These structures are supported by long slender piles below the soil. The soil-pile interaction of such frame structures is complex, but is usually modelled in several standards [Ref] as comprising of 1) lateral stiffness, 2) axial stiffness and 3) tip resistance. While in monopile type structures, it is the lateral soil-structure bending interaction that is predominantly participating in the overall structural dynamics, for frame type structures, it is the axial movement and the push-in resistance at the pile bottom tip that contributes most to the structural dynamics.

For a 4-legged jacket structure, one or more of the jacket legs may be axially loaded in tension with the remaining legs in compression, based on the wind direction relative to the turbine. This implies that one or more of the jacket piles is being pushed into the soil, while the other jacket legs experience a pull-out load. Due to the non-isotropic nature of the pile-soil interaction and the nonlinear load-displacement relations, the pile displacements are not the same at each of the 4-legs. Further the axial displacement of the pile can couple with the bending deflection. These interactions need to be investigated when determining the length and thickness of the piles in the design process and care should be taken that the design pile length is robust to the model uncertainties in the soil model. This has been achieved herein by quantifying the effect of pile tip resistance on the overall axial movement of the pile and designing the pile so that variations in the tip resistance do not result in significant variation in the axial displacement.

In order to numerically investigate soil-structure interaction of piles, which are predominantly loaded in axial direction, numerical models have been set-up and existing research work on experimental pile tests and numerical studies have been reviewed. Based on the findings appropriate physical experiments at large model scale are suggested. With the generated simulation models, the experimental tests can be accompanied by a range of numerical analyses and parametric studies. Thus, the evaluation of future test results and the assessment of experimental findings can be performed. This might add up in better validated numerical models and innovations in foundation design.

At 50m water depths, conventional jacket structures and floating structures can be highly expensive and therefore innovative sub structure designs are required. A potential candidate is for a spar buoy type sub structure to be anchored at the sea floor through an articulated joint that

prevents translation of the structure, but allows rotations. This implies that the structure also requires mooring cables to restrain its motion. Such guyed structures require much less material weight than floating spar buoys at 100m+ depths and also need far less ballast for stability. However it is required that additional buoyancy is provided for the structure due to the reduced water depths and this is provided by means of a buoyancy chamber near the mean sea level. Such an articulated joint guyed sub structure is designed herein by considering the dynamics and stability of a 10 MW wind turbine installed on it.

## 4.1 Suction-bucket foundations (AAU)

Jacket structures are usually founded on piles, these foundations are of simple design but Bucket foundations are an option that can decrease the overall cost and increase the diffusion of wind turbine. Since wind turbine are dynamically sensitive structures where stiffness requirements have to be satisfied, an alternative design allowing to increase stiffness is multi-bucket configuration (Byrne 2002), wherein loading response changes significantly with respect to a mono bucket. The following work is focused on loading of multi-bucket foundation also referred to as multi-pod, where very little moment is taken by the bucket itself. The moment load is mainly resisted by push-pull load on the vertical axis of opposite buckets. For these reasons, it is important to understand behaviour under tensile loading and improve the stiffness of foundation, so a correct design can be established. Among others, multi-pod foundations can be either tripod or tetrapod. Tripod has the advantage that it requires less material and it is easier to construct and install. This chapter has the purpose to analyze research on vertical loading of suction caisson installed in sand, focusing on works done in laboratory. Cyclic and monotonic pull-out tests are reported, specifying equipment used and test modality adopted in order to discuss and compare works of different authors. On the contrary to piles, there are no standard design methods for axially loaded bucket foundations. Oil and gas platforms transfer mainly compressive loads to the foundations. Tensile capacity is considered only for the short-term term events such as storms. Compared to the oil and gas platforms, wind turbines are very light. The foundation of a wind turbine has to sustain long-term tensile loads. It is recognized that the design of a wind turbine foundation is not driven by the ultimate capacity but it is governed by parameters as stiffness and behaviour under cyclic loading, so particular attention has been given to these topics. Important matter is the enhancement in resistance to pull-out load given by pore pressure under the lid of the caisson. This resistance is a consequence of a complex interaction between permeability of the soil, drainage path and rate of loading, and is a resource on which can possibly contribute to peak load resistance. However studys needs to be done to have a more precise model of this phenomenon. This study also emphasises the need of standard guidelines for axially loaded bucket foundations by comparing and indicating the differences of the current design methods and latest research findings for axially loaded bucket foundations.

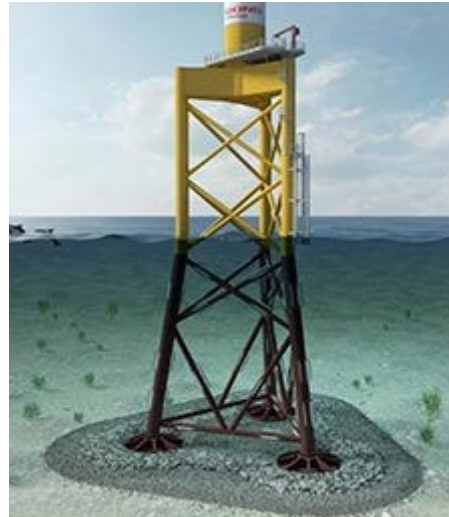


Figure 4.1-1: Jacket with bucket

can be either tripod or tetrapod. Tripod has the advantage that it requires less material and it is easier to construct and install. This chapter has the purpose to analyze research on vertical loading of suction caisson installed in sand, focusing on works done in laboratory. Cyclic and monotonic pull-out tests are reported, specifying equipment used and test modality adopted in order to discuss and compare works of different authors. On the contrary to piles, there are no standard design methods for axially loaded bucket foundations. Oil and gas platforms transfer mainly compressive loads to the foundations. Tensile capacity is considered only for the short-term term events such as storms. Compared to the oil and gas platforms, wind turbines are very light. The foundation of a wind turbine has to sustain long-term tensile loads. It is recognized that the design of a wind turbine foundation is not driven by the ultimate capacity but it is governed by parameters as stiffness and behaviour under cyclic loading, so particular attention has been given to these topics. Important matter is the enhancement in resistance to pull-out load given by pore pressure under the lid of the caisson. This resistance is a consequence of a complex interaction between permeability of the soil, drainage path and rate of loading, and is a resource on which can possibly contribute to peak load resistance. However studys needs to be done to have a more precise model of this phenomenon. This study also emphasises the need of standard guidelines for axially loaded bucket foundations by comparing and indicating the differences of the current design methods and latest research findings for axially loaded bucket foundations.

### 4.1.1 Identification and discussion of innovations on component level

#### METHODS FOR COMPRESSIVE CAPACITY

The compressive capacity of shallow foundations is calculated using the traditional Terzaghi (1943) bearing capacity formula. The formula estimates capacity of shallow onshore strip foundations. It is also applied for offshore shallow foundation calculations when improved by various modification factors to convert the plain strain problem to axisymmetric problem. The bucket foundation is a skirted shallow offshore foundation of circular shape. The soil that is trapped inside makes the bucket behave as a gravity based structure. Thus, the bearing capacity of bucket can be estimated using the traditional formulae.

$$R_c = R_\gamma + R_q + R_c + R_{fric} \quad (1)$$

Bucket compressive capacity  $R_c$  consists of four main parts: soil self-weight  $R_\gamma$ , surcharge  $R_q$ , effective cohesion  $R_c'$  and skirt friction  $R_{fric}$ . Each of these parts can be estimated in various ways which differ slightly from method to method. Factor for surcharge  $N_q$  increases exponentially with increasing soil friction angle  $\varphi$ . Most of the methods presented suggest  $N_q$  value derived by Prandtl (1920), except Larsen (2008) and Byrne (2000). Recently, Ibsen et al. (2014) has showed that  $N_q$  value for bucket foundations is influenced by surfaced roughness which was found by the finite element analysis. Bearing capacity factor for the self-weight  $N_\gamma$  depends on the values of  $N_q$ ,  $\varphi$  and surface roughness. However, it differs from method to method. Formulae for  $N_q$  and  $N_\gamma$  are provided in this paper. Most of the methods require modification factors for shape  $s$ , depth  $d$ , and inclination  $i$ . The specific formulae can be found in the references.

A large amount of laboratory tests on axially loaded bucket foundations was performed at Aalborg University. Vertical bearing capacities of rough circular surface footing and buckets of various shapes were tested and analyzed by Ibsen et al. (2012, 2013, 2014a and 2014b). These results will be discussed later on in this report.

### DNV (1992)

DNV (1992) provided guidelines for the geotechnical calculations of offshore foundations, such as gravity based and pile foundations. The application of bearing capacity for offshore foundation stability calculation is described as too rough, but a good estimate for the early stage of design.

$$R_c = A'(0.5\gamma' B' N_\gamma K_\gamma + q' N_q K_q + c' N_c K_c), \quad (2)$$

$$N_q = \tan^2(45 + 0.5\varphi) e^{\pi \tan \varphi}, \quad (3)$$

$$N_c = (N_q - 1) \cot \varphi, \quad (4)$$

$$K_q = s_q d_q i_q, \quad (5)$$

$$K_\gamma = s_\gamma d_\gamma i_\gamma, \quad (6)$$

$$K_c = s_c d_c i_c, \quad (7)$$

where  $c'$  effective cohesion,  $q'$  surcharge,  $A'$  effective bearing area of the foundation  $B'^2$ ,  $B'$  effective width of the foundation,  $N_q$ ,  $N_\gamma$ ,  $N_c$  bearing capacity factors,  $K_q$ ,  $K_\gamma$ ,  $K_c$  modification factors to account for foundation shape, embedment, and load inclination.

DNV (1992) suggests two methods for  $N_\gamma$ . The first one was found by Brinch-Hansen (1970):

$$N_\gamma = 1.5(N_q - 1) \tan \varphi. \quad (8)$$

The second was suggested by Caquot and Kerisel (1953):

$$N_\gamma = 2(N_q - 1) \tan \varphi. \quad (9)$$

Contribution of the friction on the out skirt is also considered by:

$$R_{fric} = \frac{\gamma' d^2}{2} K \tan \delta \pi D, \quad (10)$$

where  $\gamma'$  effective unit weight,  $D$  is outer diameter,  $d$  skirt length,  $\delta$  interface friction angle,  $K$  coefficient of horizontal stress.

### EC-7 (2004)

Eurocode 7 Geotechnical design (EC-7, 2004) provided guidelines for the geotechnical aspects of buildings and civil engineering structures. It adopts the same bearing capacity equation as DNV (1992), and  $N_\gamma$  is estimated only by (9). Moreover, the shape and depth factors differ from DNV (1992). The contribution of the friction on the outer skirt is not included in the formulae. For comparison reasons this guideline is included into consideration despite that it is intended for onshore foundation design.

### Byrne (2000)

Byrne (2000) used the traditional drained bearing capacity of shallow foundations formula and included the contribution of friction force on the outer skirt. The bearing capacity factors  $N_q^*$  and  $N_\gamma^*$  are taken from Bolton and Lau (1993). These factors are estimated for the axisymmetric calculation:

$$R_c = A(0.5\gamma' DN_\gamma^* + qN_q^*) + \frac{\gamma' d^2}{2} K \tan \delta \pi D. \quad (11)$$

### Ibsen (2014)

Ibsen (2014b) derives a new theoretical relationship of the bucket bearing capacity:

$$\frac{R_c}{R_\gamma} = 1 + 2.9 \frac{d}{D} \quad (12)$$

$$R_\gamma = A(0.5\gamma' DN_\gamma)$$

In this formulation Larsen (2008) derived new bearing capacity factors  $N_q$  and  $N_\gamma$  for the drained bearing capacity. The study was performed using an axisymmetric numerical model with bucket foundations and lead to equations (13) and (14). Detailed information is provided in Larsen (2008) and Ibsen et al. (2014b).

$$N_q = c_3 e^{c_4 \pi \tan \varphi} \tan^2 \left( 45 + \frac{\varphi}{2} \right), \quad (13)$$

$$N_\gamma = c_1 ((N_q - 1) \cos \varphi)^{c_2}, \quad (14)$$

where  $c_i$  are available for circular and strip foundation with rough and smooth surface, as shown in Table 4.1-1.

**Table 4.1-1: Fitted values for constants in Eq. (12) and (13) for the bearing capacity factors.**

	Circular foundation		Strip foundation	
	Smooth	Rough	Smooth	Rough
$c_1$	0.1	0.16	0.12	0.25
$c_2$	1.33	1.33	1.51	1.5
$c_3$	0.715	0.8	1	1
$c_4$	1.42	1.5	1	1

### Randolph and Gourvenec (2011)

Randolph and Gourvenec (2011) provide the classical approach for the drained bearing capacity of shallow foundations.  $N_q$  is estimated by (3).

$$R_c = A'(0.5\gamma' B' N_\gamma K_\gamma + (q + a)N_q K_q - a), \quad (14)$$

$$N_\gamma = 1.5(N_q - 1) \tan(\tan \varphi), \quad (15)$$

where  $a$  is soil attraction factor.

There is also a suggested solution for  $N_\gamma$  for rough foundation by Davis and Booker (1971):

$$N_\gamma = 0.1054e^{9.6\varphi}. \quad (16)$$

### Ovesen et al. (2012)

Geotechnical engineering textbook (Ovesen et al., 2012) provides a general bearing capacity equation based on Terzaghi (1943). The main equation is (2),  $N_q$  is estimated by (3).

$$N_\gamma = 0.25((N_q - 1) \cos \varphi)^{1.5}, \quad (17)$$

$$N_c = \frac{(N_q - 1)}{\tan \varphi}. \quad (18)$$

### Finite Element Modelling

Plaxis is a commercial geotechnical design program which is based on finite element method. Depending on the complexity of the structure, the design can be two-dimensional or three-dimensional. User-friendly interface allows design of various geotechnical structures, easy boundary set-up, loading application in steps and etc. Subsequently, a number of soil constitutive models are available which estimate the soil response when the soil properties are well known. Obviously, the quality of the solution increases if the soil properties are estimated well. Plaxis 2D axisymmetric model provides a relatively fast estimate of the bearing capacity and displacements of axially loaded bucket foundations.

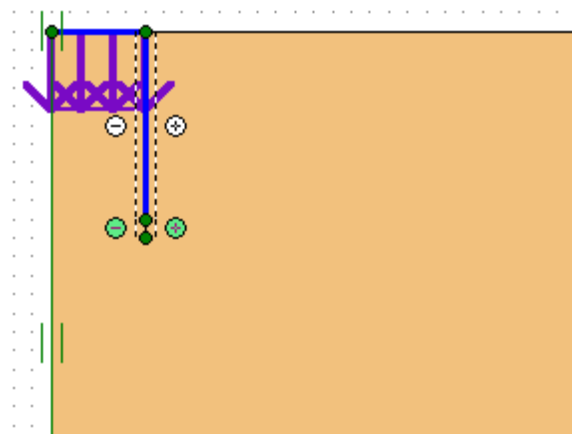


Figure 4.1-2: A fragment of Plaxis 2D model for bucket foundation with geometric ratio of  $d/D=1$

Two models, Mohr-Coulomb and Hardening-Soil, were chosen for the research. The first one is rather simple, because it requires only the main soil parameters which are rather easy to get from the soil classification data and cone penetration test (CPT). For drained soil a rather rapid calculation can be performed only knowing friction angle  $\varphi$ , dilation angle  $\psi$ , effective cohesion  $c'$ , Poisson's ratio  $\nu$  and effective Young's modulus  $E'$ . On the contrary, the Hardening-Soil model

requires knowledge about the advanced soil properties, such as triaxial loading stiffness  $E_{50}^{ref}$ , triaxial unloading stiffness  $E_{ur}^{ref}$ , and oedometer stiffness  $E_{oed}^{ref}$ . The parameters serve to describe the non-linearity in stress-strain curve as well as stress level dependency. The advanced parameters can be estimated using triaxial testing or calculated by the formulae provided in Schanz et. al. (1999).

**Table 4.1-2: Methods used for ultimate capacity analysis**

No.	Method	Variables
M1	Plaxis 2D, Hardening-Soil	$d, \gamma', \delta, \phi_{triax}$ .
M2	Plaxis 2D, Mohr-Coulomb	$d, \gamma', \delta, \phi_{triax}$ .
M3	Randolph and Gourvenec (2011) and Davis and Booker (1971)	$d, \gamma', \phi_{red,pl}$ .
M4	Randolph and Gourvenec (2011)	$d, \gamma', \phi_{red,pl}$ .
M5	Eurocode 7: Geotechnical Design	$d, \gamma', \phi_{red,pl}$ .
M6	Byrne (2000)	$d, \gamma', \delta, \phi_{red,triax}$ .
M7	Ibsen (2014)	$d, \gamma', \phi_{red,triax}$ .
M8	DNV (1992) and Caquot and Kerisel (1953)	$d, \gamma', \delta, \phi_{red,pl}$ .
M9	DNV (1992) and Brinch-Hansen (1970)	$d, \gamma', \delta, \phi_{red,pl}$ .
M10	Ovesen et al. (2012)	$d, \gamma', \phi_{red,pl}$ .
M11	Senders (2008) Senders (2008))	$d, \delta, q_c (\epsilon \gamma', l_D)$
M12	Houlsby et al. (2005)	$d, \gamma', \delta$
M13	DNV (1992) tensile loading	$d, \gamma', \delta$

### CASE STUDY OF COMPRESSIVE CAPACITY

In order to compare and visualize the differences of these design tools, an idealized case study is created. Table 4.1-2 provides the numbered marking for the previously mentioned methods which is used in the comparison. Moreover, the main variables are given in the table to avoid any possible confusion. In this study, two bucket foundations of different geometries are compared. The seabed contains ideal uniform dense sand, and the water depth is 15 meters. Soil parameters are given in Table 4.1-3. A jacket structure is supported by bucket foundations; therefore, the critical loads are axial tensile and axial compressive load. It does not matter how many buckets there are, because the comparison will be done for the pure axial capacity of a single foundation.

**Table 4.1-3: Geotechnical soil parameters**

Parameter	Units	Value
Triaxial friction angle $\phi_{triax}$	[°]	38.8
Plane friction angle $\phi_{pl} = 1.1\phi_{triax}$	[°]	42.7
Interface friction angle $\delta$	[°]	32.2
Angle of dilation $\psi$	[°]	9
Density ratio $l_D$	[%]	80
Soil unit weight $\gamma$	[kN/m <sup>3</sup> ]	20.25
Effective unit weight $\gamma'$	[kN/m <sup>3</sup> ]	10.25
Effective cohesion $c'$	[kPa]	0 1 (in Plaxis)
Effective Young's modulus $E'$	[MPa]	39.3

Triaxial unloading stiffness $E_{ur}^{ref}$	[MPa]	260.9
Oedometer stiffness $E_{oed}^{ref}$	[MPa]	43.7
Triaxial loading stiffness $E_{50}^{ref}$	[MPa]	87
Poisson's ratio $\nu'$	[-]	0.2
Plaxis interface factor $R$	[-]	0.78
Plaxis factor $m$	[-]	0.58
Reference pressure $p$	[kPa]	100
Over consolidation ratio $OCR$	[-]	1
Horizontal stress parameter $K$	[-]	0.37
Cone penetration $q_c$ at 5 m depth	[kPa]	10297
Cone penetration $q_c$ at 5 m depth	[kPa]	15075

### Soil Parameters

Horizontal soil stress parameter  $K$  is often recommended to be in the range of 0.5-0.8 (DNV, 1992, and Byrne and Houlsby, 2002). This recommendation originates from the offshore pile design criteria. Hammering of piles into the seabed strengthens the soil properties; therefore, the factor  $K$  can be higher. However, suction bucket installation is slightly different and  $K_0=1-\sin\phi_{triax}$  is used instead in this study according to Larsen (2008). For the analytical solutions, the reduced friction angle is used. It is calculated using the plane friction angle and the dilation angle in order to reduce the possibility of overestimated axial capacity. The parameter is analyzed in details by Ibsen et al. (2012). This technique was adopted by several authors, such as Larsen (2008) and Vaitkunaite et al. (2012).

$$\tan \phi_{red} = \frac{\sin \phi \cos \psi}{1 - \sin \phi \sin \psi}, \quad (19)$$

where  $\phi_{red}$  is reduced friction angle,  $\phi$  friction angle equal and  $\psi$  angle of dilation.

Moreover, in the compressive capacity calculations, where the formulae are based on plain strain solution, the plane friction angle to  $\phi_{pl}=1.1\phi_{triax}$  was introduced.

### Geometry of the Foundation

Two weightless bucket foundations are considered for the analysis. Both of them have a diameter  $D$  of 10 m. The skirt lengths  $d$  are 5 m and 10 m. During the comparison they are identified by the geometric ratio  $d/D$ , which is 0.5 and 1 correspondingly. Foundation surface is rough. The foundations are illustrated by Figure 4.1-2.

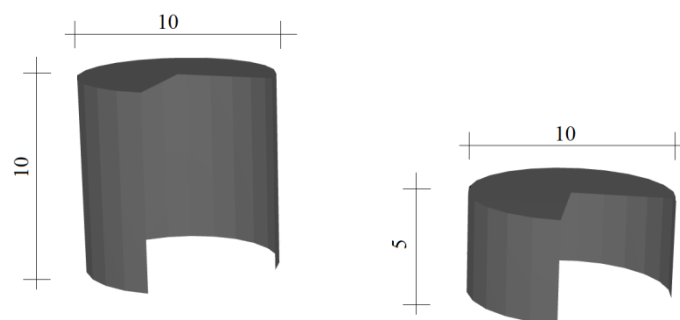


Figure 4.1-3: Buckets dimensions in meters

### Comparison

During the case study, the vertical bearing capacity was estimated according to previously presented analytical and numerical methods. The 10 bearing capacities were estimated for each of the bucket foundations. It was showed that Ibsen (2014) has derived a good match for the laboratory test preformed and described in the next section. Consequently, the bearing capacities were therefor normalized by the Ibsen(2014) estimation (M7). Figure 4.1-4 presents the normalized bearing capacities. It can be seen that the values deviate slightly and the tendencies depend on the embedment ratio. However, Byrne (2000) provides the highest estimate of the compressive bearing capacity (M6). On the contrary, the most conservative values are computed using Ovesen et al. (2012) expression (M10). The estimation of  $R_q$ ,  $R_y$  and  $R_{fric}$  differ from method to method depending on the bearing capacity factors. Skirt friction is sometimes not even included into the calculation, because it is considered to be too small, see methods M3, M4, M5 and M10. When analyzing the analytical methods, it is found that  $R_q$  value increases approximately twice if the skirt is two times longer. However, it increases 2.27 times using M10 while two times using M5, M6 and M7. The frictional part  $R_{fric}$  becomes even four times larger if the larger bucket is used. Obviously  $R_y$  is equal, independent of the skirt length, as it depends only on the foundation area.

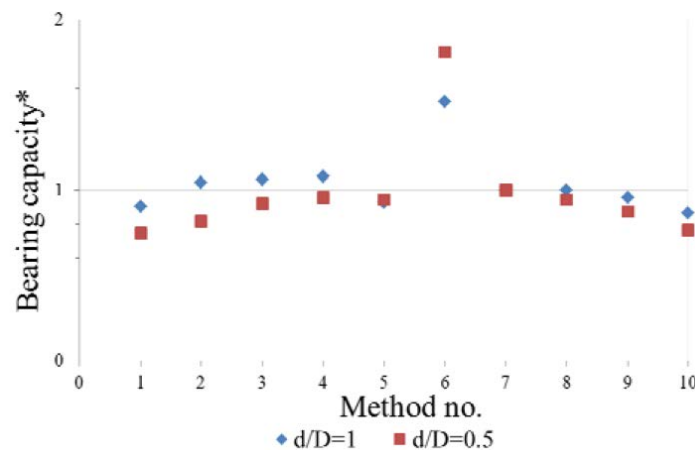


Figure 4.1-4: Compressive capacity normalized by Ibsen(2014), see method no. 7 in the Table 4.1-2

### METHODS FOR TENSILE CAPACITY

Applying the theory of anchoring systems, three failure modes for tensile loading on bucket foundation can be considered. When the tensile load is applied rapidly, suction under the lid is generated creating the reverse bearing capacity. In long-term loading conditions, two components resist the tensile load: friction on the outer skirt, and the lower value of the soil plug weight and friction on the inner skirt. Obviously, foundation self-weight is a favorable component, but it is not considered in this study as mentioned earlier. This study considers only long-term tensile loading.

### DNV (1992)

DNV (1992) is a widely used standard for offshore foundations. It provides the design principles for gravity based and monopole foundations as well as jack up platforms. Open ended offshore steel piles are of circular tube shape and in this way similar to bucket foundations. Therefore, the recommendations for axially loaded offshore piles will be considered in this report :

$$R_t = -((K \tan \delta)_o D_o + (K \tan \delta)_i D_i) \pi \frac{\gamma' d^2}{2} \quad (20)$$

where  $i$  and  $o$  are indications for the inner and outer skirt correspondingly.

### Houlsby et al. (2005)

Houlsby et al. (2005) have proposed to take into account the reduced vertical stress down the bucket. The authors described that if the reduction is not included into the tensile capacity calculations, bucket strength is overestimated.

$$R_t = -\gamma' Z_o^2 y \left( \frac{d}{Z_o} \right) (K \tan \delta)_o (\pi D_o) - \gamma' Z_i^2 y \left( \frac{d}{Z_i} \right) (K \tan \delta)_i (\pi D_i), \quad (21)$$

$$y \left( \frac{d}{Z_x} \right) = \exp \left( -\frac{d}{Z_x} \right) - 1 + \left( \frac{d}{Z_x} \right), \quad (22)$$

$$Z_i = \frac{D_i}{4(K \tan \delta)_i}, \quad (23)$$

$$Z_o = \frac{D_o(m^2 - 1)}{4(K \tan \delta)_o}, \quad (24)$$

where  $Z_{i/o}$  is interface parameter, and  $m=1.5$ .

### Senders (2008)

Senders (2008) used cone resistance for the estimation of the tensile bucket capacity. Foundation resistance is expressed as the sum of the inner friction and the outer friction of the skirt.

$$R_t = F_{i,t} + F_{o,t}, \quad (25)$$

$$F_{i,t} = \pi D_i k_{f,i} \int_0^d q_c(z) dz, \quad (26)$$

$$F_{o,t} = \pi D_o k_{f,o} \int_0^d q_c(z) dz, \quad (27)$$

$$k_{f,i} = -0.375C \left[ 1 - \left( \frac{D_i}{D_o} \right)^2 \right]^{0.3} \tan \delta, \quad (28)$$

where  $q_c$  is cone resistance from a CPT test,  $k$  coefficient,  $C$  coefficient equal to 0.012.

Five different static pull-out capacities were estimated for each of the bucket foundations. It was showed that Senders (2008) has derived a good match for the Performed laboratory test (M11). Consequently, the bearing capacities were normalized with this CPT based method. Cone resistance highly depends on location and sand properties. However, an idealized profile was assumed which corresponds to possible cone penetration values for dense sands, as shown in Table 4.1-3. Figure X4 presents the normalized pull-out capacities. It can be seen that the values deviate significantly and the tendencies depend on the embedment ratio. Tensile capacity for the smaller bucket is very similar, but for the smaller bucket methods M1 and M2 estimate much higher capacity than the rest of the methods. On the contrary, the most conservative estimate of the bearing capacity was estimated by M11.

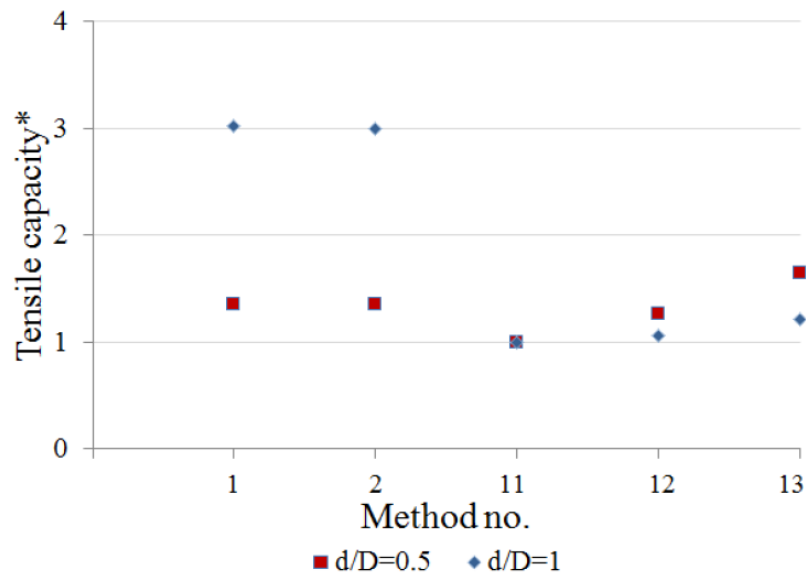


Figure 4.1-5: Tensile capacity normalized by Senders (2008), see M11 in the Table 4.1-2

The intension of this article was to collect up-to-date methodology for the compressive and the tensile bucket bearing capacity estimation. Ten different expressions were used for the estimation of the compressive capacity and five for the tensile capacity. Quite some scatter between the compressive and tensile capacities was seen, which indicates that more testing and analysis would be favourable to clarify the design of the bucket foundations

#### 4.1.2 Preliminary studies of innovations on component level

Therefore large model tests are carried out in the geotechnical laboratory of Aalborg University, see Figure 4.1-6 where the testing rig is shown.



Figure 4.1-6: The test set-up of axially loaded bucket foundations

#### TEST EQUIPMENTS

The equipment used for testing of axial loaded bucket foundation is shown schematically in Figure 4.1-7. The testing rig includes a rigid circular box, a movable loading frame equipped with two movable hydraulic pistons, a signal transducers box and a measuring system described in the following.

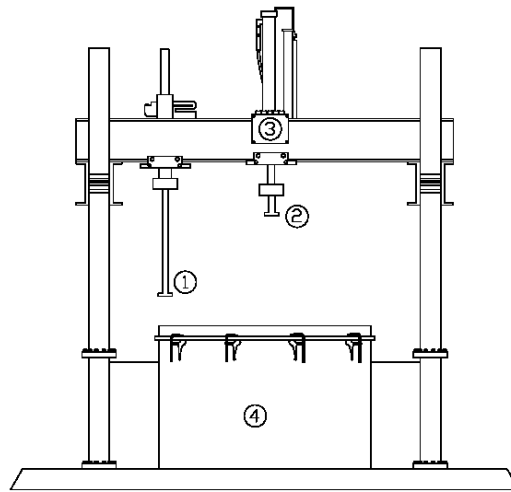


Figure 4.1-7: Equipment used testing bucket foundation: loading piston (1), installation piston (2), signal transducers box (3) and sand box (4)

### Sand box

The sand box is a steel made cylinder with a diameter of 250 cm and a total height of 152 cm. A 30 cm thick layer of gravel with high permeability is placed at the bottom, in order to provide a uniform distribution of water and create uniform water pressure, avoiding piping problems. A geotextile sheet is placed on top of the gravel layer, to avoid sand infiltration and thus maintain drainage property unaltered. The top layer is composed of Aalborg University Sand No.1 and has a thickness of 120 cm. Water is leaded into the box by a system of perforated pipes, uniformly placed on the bottom. To supply water a tank of 1 m<sup>3</sup> is filled of water and placed in a higher position with respect to the sand box. This allows having an upward gradient in the sand box, needed to loosen the sand. The in and out flow of water is controlled by a system of valves. By regulating the inflow valve, the gradient in the sand box is controlled.

### Bucket Models.

Two cylindrical shaped models of bucket foundation have been built to be tested. Both models have an outer diameter of 1000 mm, and a wall thickness of 3 mm, the skirt length is 500 mm (aspect ratio  $d/D=0,5$ ), and 1000 mm ( $d/D=1$ ). Models are approximately scaled of 1:10. To simulate overburden pressure the sand is compressed by a suction system that create a depression inside the sand box. Hermetic isolation is provided by a membrane made of nonporous latex rubber. The membrane has been cut so that can fit with the bucket model, it has thicknesses that allow it to adapt to the sand surface. Four connections for suction pipes and one connection for surface pressure transducer are installed on the membrane. Hermetic isolation along the perimeter of the sand box is provided by a groove where a circular rubber gasket is inserted. The membrane is stretched on the rubber gasket and the steel frame is placed on it and fixed with clamps as shown in Figure 4.1-6.



Figure 4.1-8: Bucket model of  $d/D=0.5$

#### Loading and measuring systems.

Two hydraulic pistons are connected on the frame placed above the sand box: the installation piston and the loading piston as shown in Figure 4.1-7. The installation piston is used to run CPT tests and to install the bucket. It has a capacity of 200 kN and is actuated by a control, while speed has to be settled by the control panel in a range of 0.01-5 mm/s. Vertical displacement is measured by a displacement transducer connected to the transducers box, applied force is measured by a load cell. The signals are recorded by a computer with the program Catman. Loading piston can apply a vertical force of 250 kN and has a maximum displacement range of 40 cm. Force or forced displacement for static and cyclic loading are applied with loading piston, controlled by the MOOG system whereby data are recorded and test are programmed. A wide range of options are available for cyclic loading in terms of frequencies and load modalities. Displacements are measured by two 125 mm displacement transducers. As shown in Figure 7, six pressure transducers are installed at different levels inside and outside the bucket. Installation valves and connection for pressure transducers are installed on top of the lid. Cable of pressure transducers are connected to the signal transducers box and through the signal amplifier MGCplus and Spider 8, the signal is elaborated by Catman. A pressure sensor is placed outside and connected to MGCplus system, in order to have a measurement of ambient pressure.

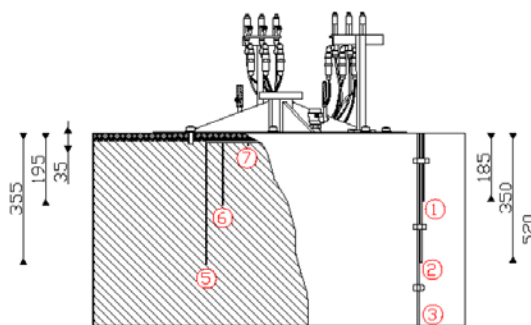


Figure 4.1-9: Section of the test bucket  $d/D = 0.5$ . Distances and position of pressure transducers inside and outside the bucket are shown. Connection for pressure transducers (1) and installation valves (2)

#### Soil Description

Sand utilized is Aalborg University Sand No. 1. The main part of sand is quarts, but it also contains feldspar and biotit. The classifications parameters is given in Table 4.1-4

**Table 4.1-4: classifications parameters of Aalborg University Sand No. 1**

50% quantile	$d_{50}$	0.14 mm
Uniformity coefficient	$d_{60}/d_{10}$	1.78
Specific grain density	$d_s$	2.64
Maximum void ratio	$e_{max}$	0.854
Minimum void ratio	$e_{min}$	0.549
Permeability	$K_{e=0.612}$	$6.89 \cdot 10^{-12} \text{ m}^2$

### Soil preparation

To obtain homogeneity of the soil and so ensure comparability between tests, the procedure described in the following has been settled, based on previous experiences (Fisker, L.B., and Kromann, K. 2004). First the groove along the perimeter of the sand box is cleaned by compressed air and paper, then the rubber gasket is placed and aluminum frame is fixed by clamps. To loosen the sand, an upward gradient of 0.9 is applied opening gradually the inflow valve. To avoid air infiltration during vibration, water is set to rise approximately 8 cm above the sand surface. To reach this level, the inflow valve is closed and additionally water has to be poured from the top, placing a small panel on the area of interest so as soil in the surface do not move. A wooden panel with symmetrically distributed holes is placed on the box, as shown in Figure 4.1-10. Then rod vibrator is systematically pushed and pulled in the sand. After vibration the outflow valve is opened and water level is lowered till one centimeter above the sand surface, then the wooden plates are removed and the surface is first cleaned manually, then levelled using a specific shaped aluminum beam.



**Figure 4.1-10: Vibration starts inserting the rod vibrator in the hole marked in yellow**

### CPT tests

Cone penetration tests are carried out to have complete information about compaction and homogeneity of the soil. CPT probe used is shown in Figure 10. It has a diameter of 15 mm, tip area of 176.7 mm<sup>2</sup>, cone angle of 60° and penetration length of 120mm. It is connected to the installation pistons then force transducer is plugged in the signal transducer box. Afterwards four CPT tests in four different positions are run. The penetration velocity is set to 5 mm/s. The penetration resistance  $q_c$ , time and vertical displacement is measured. The CPT test is performed to a depth of 110 mm. Figure 4.1-11 shows the typical results of cone penetration test made in the four positions of the test rig. Trend of the curves shows a cone resistance that uniformly increases with depth. Figure 4.1-11 shows also the variation in relative density  $D_r$  with respect to depth. An iterative process described in Ibsen et al. (2009) is used to calculate  $D_r$  based on the CPT tests.

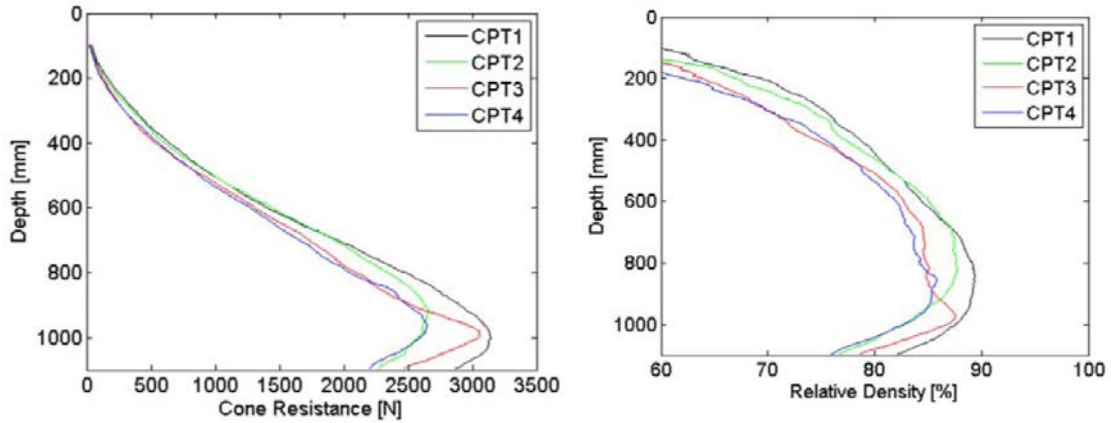


Figure 4.1-11: CPT test results for test no 5

#### TEST PROCEDURES.

In the following, steps on how to run tests are described. Soil preparation is common for both tests with and without membrane. Steps of installation are the same for both long and short bucket. Only differences are the longer time and greater installation force required in the installation of long bucket.

#### Test without membrane

The water level is raised to 5-8 cm above the surface level and is kept while tests are run. The bucket is connected to the installation piston and installed with a speed of 0.2 mm/s. To ensure comparability between different tests, a preloading load of 70 kPa is reached before to close the two valves of the lid. An indicator of a good installation is water flowing out from the two valves of the lid, since no air is trapped between lid and soil. Figure 14 is showing installation loading curve that is similar for all tests, since sand and sand properties like relative density and saturation are uniformed by soil preparation. In the first part of the curve it can be seen the increase of resistance due to skin friction of the sand adjacent to the caisson. When the lid touches the surface, the load is increase to 70 kN.

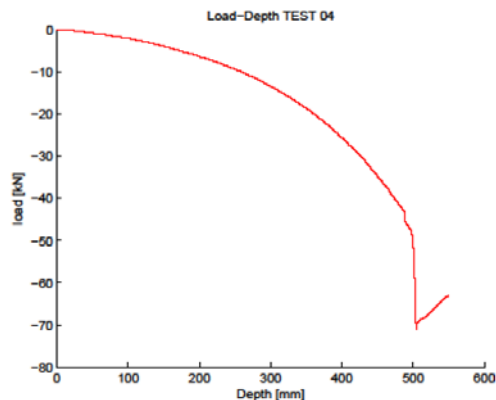


Figure 4.1-12: Installation load curve for static test

Once installation has been completed, installation piston is disconnected and the loading piston is positioned in the central position of the horizontal beam and fixed. Pressure sensors are connected to the signal transducers box. Data of pressures, load and displacement are registered by both MOOG and Catman.

### Test with membrane

Test with membrane is performed in order to simulate overburden pressure. Overburden pressure is used in order to have a greater stress level along the skirt. This allows simulating higher friction ratios. Preparation and installation of the bucket are then the same as described in for the tests without a membrane. After the bucket is penetrated into sand, the filter is laid on the sand and the membrane is outstretched so that overlay the rubber gasket placed on the perimeter. A metal ring is positioned and fixed with clamps. Installation piston is then removed and load piston is connected as indicated in the procedure of without membrane test. Suction pipes are connected to the membrane and the suction system is activated. The pressure level is measured by Catman and, once reached the required value, has to be kept constant for at least 12 hours.

### 4.1.3 Results presentation

Tests carried out until now are summarized in Table 4.1-5

**Table 4.1-5: Test overview**

Test	L/D	Load	Overburden pressure [kPa]	Displacement [mm]	Amplitude [kN]
13.02.06	0.5	Static	0	3.8	-
13.02.08	0.5	Static	0	4	-
13.02.09	0.5	Static	40	8.8	-
13.02.10	1	Static	0	3.9	-
13.02.11	0.5	Static	20	4	-
13.02.12	0.5	Static	40	6	-
13.02.14	1	Static	0	6.5	-
13.02.15	0.5	Static	0	4	-
13.03.02	0.5	Cyclic	0	-	1.925
13.03.03	0.5	Cyclic	0	-	3.85

In the following Typical test results are presented. All tests presented are carried out with the bucket model (d/D=0.5) numbers in Figure 4.1-9 are showing the corresponding position of pressure measurements.

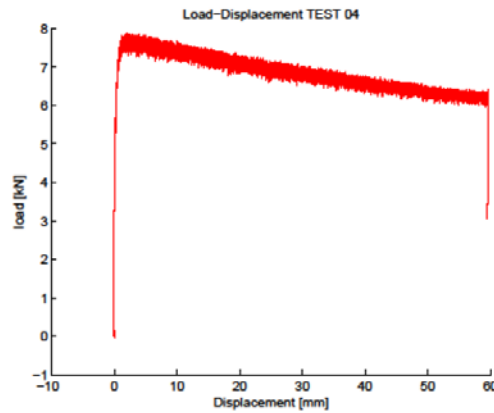


Figure 4.1-13: Load-Displacement curve for static test without overburden pressure

#### Static test without overburden pressure

Figure 4.1-13 is shown the expected trend for a static load – displacement curve. In this case in MOOG it has been set up to reach a maximal vertical pullout displacement of 60 mm. That has to be reached in 3000 seconds. The load – displacement curve is very steep until it reaches the maximal value of 7.8 kN, than is slightly decreasing until a residual value of 6.2 kN before to drop in correspondence of the end of the test. To show pressure measurements, it has been chosen to split the results in two graphs.

Figure 4.1-14 shows the pore pressured measured on the inside and outside of the bucket. The positions of the pore pressure measurement are shown on Figure 4.1-9. Measurement of atmospheric pressure given by “p6a” and shown in both graphs, this is made in order to have a reference point and allow a better comparison between results.

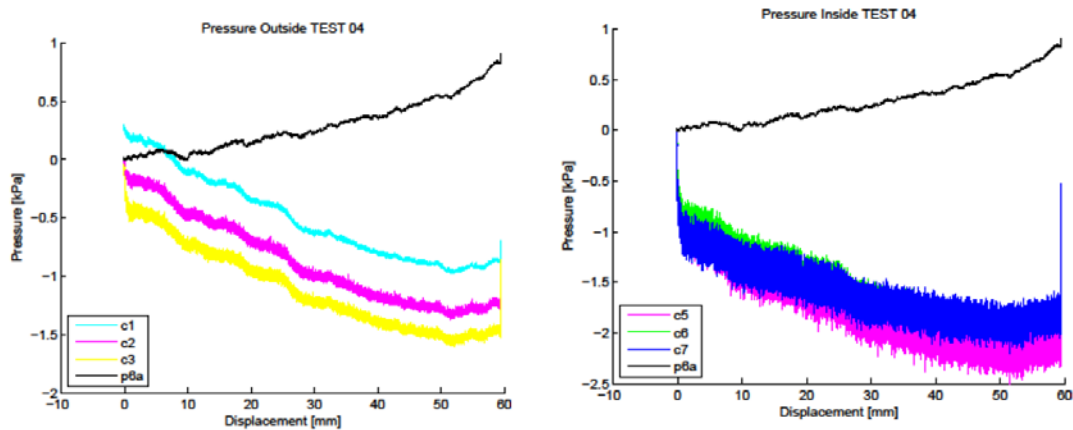


Figure 4.1-14: Pressure measurements at the outside and inside of the bucket

#### Cyclic test without overburden pressure

Figure 20 shows a load-displacement curve for a cyclic test. Considering results of static test, for the cyclic test 40000 cycles has been settled with a frequency of 0.1 Hz and an amplitude of 50% of the static maximum load. Before of the cyclic load, the bucket is loaded with a static tensional load of 50% of the static maximum load, by “round ramp” mode.

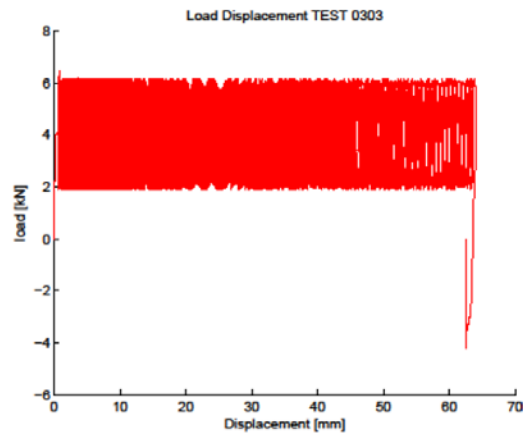


Figure 4.1-15: Load-Displacement curve for cyclic test without overburden pressure

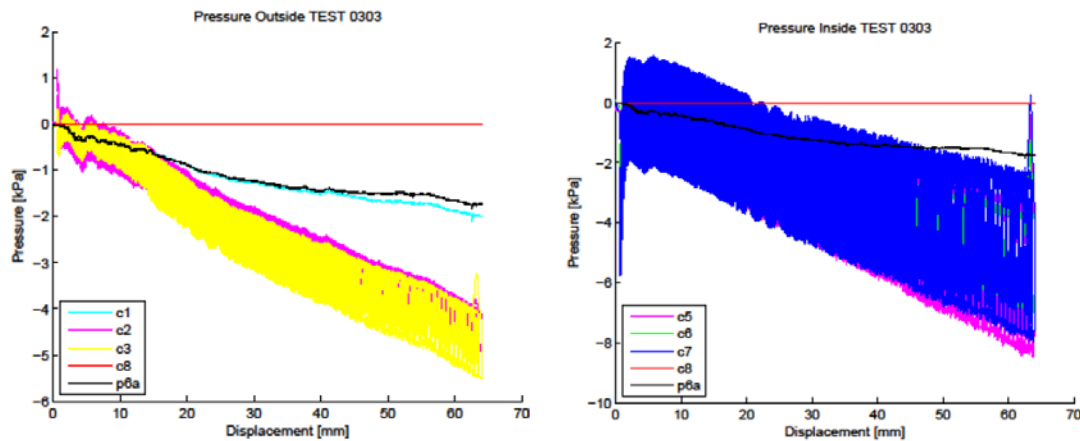


Figure 4.1-16: Pressure measurements at the outside and inside of the bucket

Pressure results are presented in the same way as for the static test, as it can be seen in Figure 4.1-16.

#### 4.1.4 Interim conclusion and assumed impact of innovations on component level

In this section the preliminary tests are analysed with CPT based methods both for the installation and the pull-out face of the tests. In order to compare results, load and displacements are plotted in dimensionless form, respectively as  $V/(D^3 \cdot \gamma)$  and  $h/D$ , according to Kelly et al. (2006). In the following study, parameters are evaluated from responses of test 6, test 9, and test 11, carried out with overburden pressure of respectively 0kPa, 40kPa, and 20kPa.

##### DNV CPT-based installation method.

DNV presents a method to estimate the installation resistance of steel caisson based on the average cone resistance  $q_c$ . Installation resistance is calculated summing friction forces and end-bearing resistance by (29). End bearing resistance and friction resistance on the skirt, are related to  $q_c$  respectively by constants  $k_p$  and  $k_r$ , of which suggested ranges are listed in Table 4.1-6

$$R_i = F_i + F_o + Q_{tip} \quad (29)$$

$$F_i = \pi D_i k_f \int_0^d q_c(z) dz \quad (30)$$

$$F_o = \pi D_o k_f \int_0^d q_c(z) dz \tag{31}$$

$$F_o = \pi D_o k_p q_c(z) \tag{32}$$

**Table 4.1-6: Parameters suggested by DNV**

$k_p$		$k_f$	
Most probable	Highest expected	Most probable	Highest expected
0.3	0.6	0.001	0.003

**Senders (2008) CPT-based installation method.**

*Senders (2008)* suggests to modify CPT-based method presented in DNV using a different  $k_p$  and evaluating  $k_f$  with *Formula 22*.

$$k_f = C \left[ 1 - \left( \frac{D_i}{D_o} \right)^2 \right]^{0.3} \tan \delta, \tag{33}$$

Where  $C=0.21$  is a constant suggested by *Lehane et al. (2005)*.  $k_p$  factor is taking into account differences in shape between the circular cone and the strip geometry of the caisson rim. Values of the shape factor  $s_q$ , giving the ratio between  $N_q$  for circular and strip footing, have been extrapolated and are showed in *Figure 4.1-17*, where are plotted with respect to the friction angle. In *Senders (2008)* it was noticed that  $s_q$  factor is in line with the range of  $k_p$  factor suggested by DNV, and  $s_q$  was therefore substituted to  $k_p$  in the calculation. In the present work it is chosen to use  $k_p = s_q = 1 - 0.016f' = 0.1536$ .

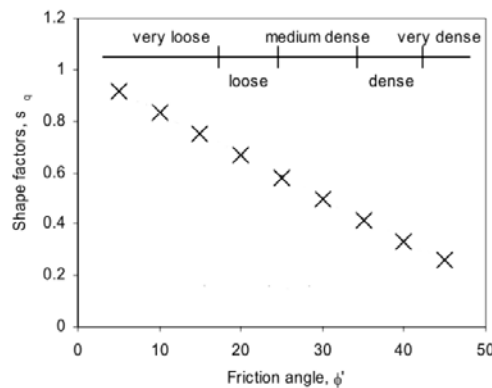


**Figure 4.1-17: Theoretical shape factor (Randolph 2004)**

**Validation of installation CPT-based methods**

In order to show how different value of  $k_f$  are affecting results of CPT-based methods, in *Figure 4.1-18* are plotted responses keeping constant  $k_p=0.3$ , while  $k_f$  is varying on the range proposed in DNV *Table 4.1-6*.

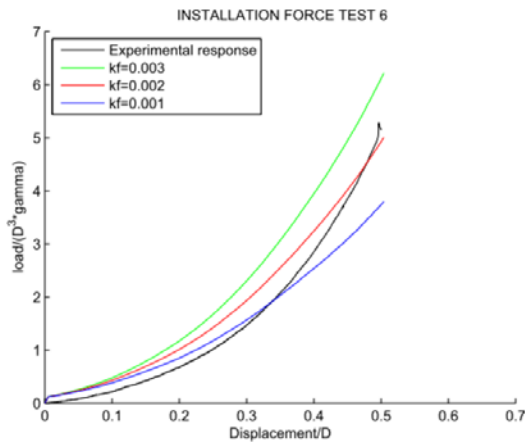


Figure 4.1-18: DNV method with constant  $k_p=0.3$  while  $k_r$  is varying

Figure 4.1-19 is showing the effect on the response varying  $k_p$  in the range suggested by DNV, and maintaining constant  $k_r=0.002$ . As can be noticed from Figure 4.1-18 and Figure 4.1-19, increase of the response is directly proportional to  $k_r$  and  $k_p$ .

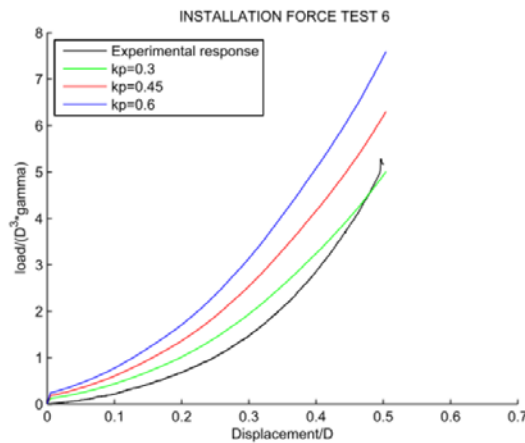


Figure 4.1-19: DNV method with constant  $k_r=0.002$  while  $k_p$  is varying

Parameters of method suggested by Senders (2008) are evaluated as  $k_r=0.0032$  (33), and  $k_p=0.1536$  Figure 4.1-17. Best fit of parameters in DNV method is obtained with  $k_r=0.002$  and  $k_p=0.3$ . Responses are shown in Figure 4.1-20. Both CPT-based methods are giving a good approximation of the experimental response, as it can be seen in Figure 4.1-20. Peak of the experimental response is  $4.92D^3\gamma'$ , peaks in Senders (2008) and DNV methods are, respectively,  $5.1D^3\gamma'$  and  $5.0D^3\gamma'$ . Method proposed by Senders (2008) has a better slope, since the response is lower at the beginning and more steep at the end of the installation, therefore is following the experimental trend.

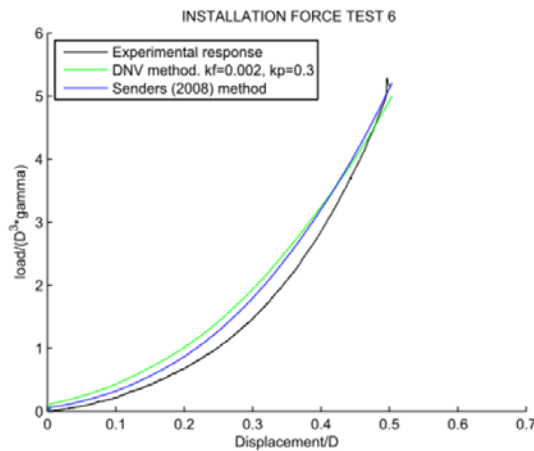


Figure 4.1-20: Comparison of DNV and Senders (2008) CPT based methods

#### Pull-out CPT-based method.

Method suggested by CUR introduces a constant  $k_f=0.004$  to evaluate the frictional pull-out resistance from  $q_c$ . In CUR is also presented a CPT based method to evaluate penetration resistance, where higher value of  $k_f$  is utilized. In CUR it is pointed out that friction resistance in compression is higher than friction resistance in tension. Frictional resistance in drained condition is calculated by (25). In the method suggested by CUR, internal and external frictions are given respectively by (26) and (27).

Senders (2008) proposed that the friction resistance is calculated following CUR procedure, but a different value of  $k_f$  is introduced in (28). This ratio was extrapolated from experimental results in centrifuge tests by Senders (2008), as -0.375. In the present work, the ratio between tensile and compressive friction is evaluated from back-calculation the experimental responses as -0.1652, and is substituted into (34).

$$k_f = -0.1652C \left[ 1 - \left( \frac{D_t}{D_o} \right)^2 \right]^{0.3} \tan \delta, \quad (34)$$

#### Validation of pull-out CPT-based methods.

CPT-based method proposed in CUR is using a  $k_f = 0.004$ . This heavily overestimating the experimental response shown in Figure 4.1-21. CUR also present an installation method where  $k_f$  is greater than the one fitted in the previous section. Therefore the methods presented by CUR are overestimating both installation and pull-out responses.

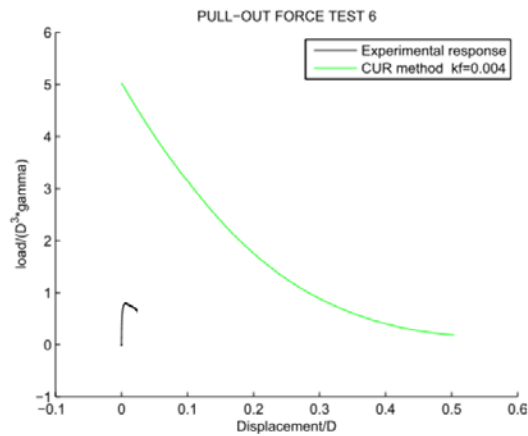


Figure 4.1-21: Pull-out method presented by CUR, heavily overestimate the pull-out resistance

By fitting CUR to the test result  $k_f = 0.00049$ . This gives a good approximation of the pull-out load for tests without overburden pressure. Figure 4.1-22 shows that the modified CUR method has a peak value of  $0.785D^3\gamma'$  where the experimental result is  $0.795D^3\gamma'$ .

In test with 0kPa overburden pressure, CPT-based method proposed by Senders (2008) gives a slight overestimation of the pull-out resistance, due to the greater value of  $k_f=0.00053$ . Figure 4.1-22 shows that Senders (2008) reaches a peak value of  $0.832D^3\gamma'$ . This result is slightly unconservative but, since the method does not need any fitting of parameters, the method presented in Senders (2008) is considered the most reliable CPT-based method to evaluate pull-out resistance.

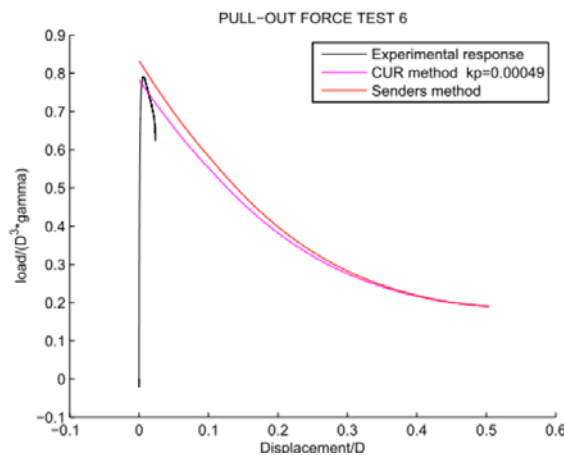


Figure 4.1-22: CPT-based method for test without overburden pressure

In the tests where overburden pressure is applied, values of cone resistance are evaluated before of the installation phase. After the application of overburden pressure, it is not possible to carry out CPT tests. In the tests with overburden pressure of 20kPa and 40kPa,  $k_f$  are evaluated as, 4.5 and 5.7 times the  $k_f$  measured with zero overburden pressure. Function is fitted in order to evaluate  $k_f$  with different overburden pressures, see Figure 4.1-23. The slope progressively decreases with the increase of overburden pressure, showing that  $k_f$  is not constant but dependent on the applied overburden pressure. As overburden pressure is applied, a decrease of the friction angle will occur, therefore it is suggested that  $k_f$  could be dependent on the stress stage in the same way as the friction angle. To find this relationship more tests must be performed to confirm this theory.

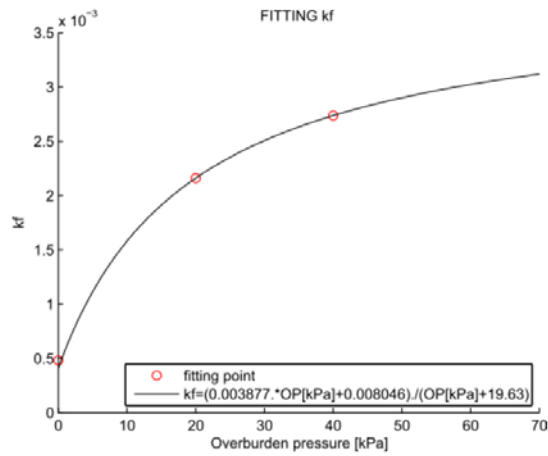


Figure 4.1-23: Function relating  $k_f$  and overburden pressure

In Figure 4.1-24 and Figure 4.1-25 the experimental responses are compared to the results calculated with  $k_f$  defined by Figure 4.1-23. Figure 4.1-24 and shows that CUR and Senders (2008) methods are respectively underestimating and overestimating the response. Therefore the same trend as observed with zero overburden pressure is maintained.

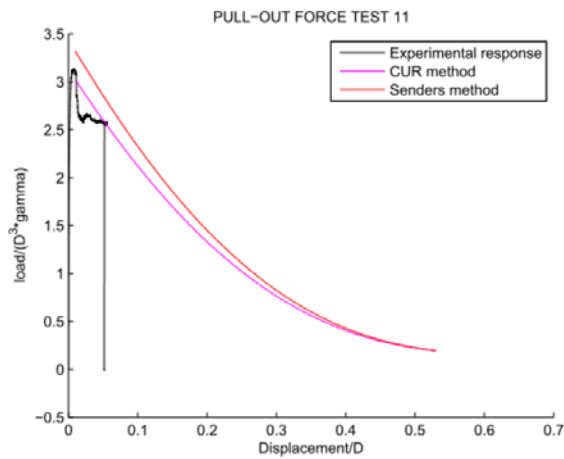


Figure 4.1-24: CPT-based methods for 20kPa overburden pressure

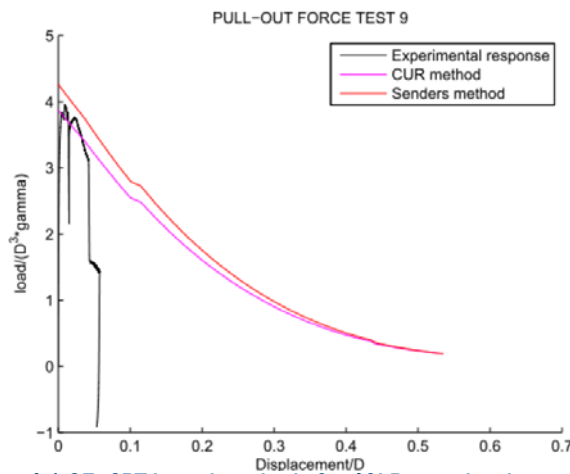


Figure 4.1-25: CPT-based methods for 40kPa overburden pressure

#### 4.1.5 Required experimental investigations on innovations on component level

This chapter presents a new developed testing rig of Aalborg University, and the procedure followed to carry out tests. Responses obtained are considered of high reliability, given the large model test with scaling factor adopted (1:10) and the standardized procedure followed in each test. The possibility to apply overburden pressure allows examining a wide range of friction ratios simulating different skirt length. This allows extending the possibility of study to configurations otherwise not reachable. Methods to evaluate pull-out and installation forces are validated, relying on responses obtained from tests described. More tests are needed in order to reach a better definition of parameters on which the designs methods are based. Since in installation measurements is not well defined where the lid makes contact with soil, an approximation on this value has been done. It is believed that more precise data can be obtained installing for a depth of 50cm the bucket model M2 ( $L/D=1$ ). Following this expedient ensures that only frictional forces and end-bearing resistance Dependence of  $k_f$  to overburden pressure has been demonstrated, however a better definition of parameters used in CPT based method is needed. The foundation of a wind turbine has to sustain long-term tensile loads. It is recognized that the design of a wind turbine foundation is not only driven by the ultimate capacity but it is governed by parameters as stiffness and behaviour under cyclic loading, so particular attention has been given to these topics. The new test rig has the capability to study this effects and a test program is under execution. Important matter is the enhancement in resistance to pull-out load given by pore pressure under the lid of the caisson. This resistance is a consequence of a complex interaction between permeability of the soil, drainage path and rate of loading, and is a resource on which can possibly contribute to peak load resistance. However, study's needs to be done to have a more precise model to describe this phenomenon.

#### REFERENCES

- Brinch-Hansen, J (1970). "The Revised and Extended Formula for Bearing Capacity," Geotechnisk Institut, Bulletin No. 28, Copenhagen, pp 5-11.
- Byrne, BW (2000). "Investigations of Suction Caissons in Dense Sand," PhD Thesis, The University of Oxford.
- Caquot, A, and Kerisel, J (1953). "Sur la Terme de Surface dans le Calcul des Fondations en Milieu Pulverult," *Proc. of the 3rd International Conference on Soil Mechanics and Foundation Engineering*, Vol. 1, Zurich.
- CUR (2001) 2001-8; Bearing capacity of steel pipe piles, Centre for Civil Engineering Research and Codes.
- Davis, EH, and Booker, JR (1971). "The bearing capacity of strip footings from the standpoint of plasticity theory," *Proc. Australia-New Zealand Conf. Geomech.*, Melbourne, Australia, pp 276-282.
- DNV (1992). Foundations. *Classification Notes No.30.4*, Det Norske Veritas, Norway, pp 13.
- EC-7 (2004). EN 1997-1:2004, Eurocode 7: Geotechnical Design – Part 1: General rules. *Dansk Standard*.
- Fisker, L.B., and Kromann. K. (2004). "Cyklisk Belastning af Bøttefundament i Tryktank", Speciale ved Aalborg University.
- Foglia, A, Ibsen, LB, and Andersen, LV (2012). "An Innovative Physical Model for Testing Bucket Foundations", NGM 2012 Proceedings is the 16<sup>th</sup> Nordic Geotechnical Meeting, Vol. 1, Dansk Geoteknisk Fore ning, pp. 323-300.

- Houlsby, G.T. and Byrne, B.W. (2005a). Design procedures for installation of suction caissons in sand. Proceedings of the ICE, Geotechnical Engineering 158, No. 3, 135- 144.
- Houlsby, G. T., Kelly, R. B. & Byrne, B. W. (2005b) The tensile capacity of suction caissons in sand under rapid loading. Proc. International Symposium on Frontiers in Offshore Geotechnics (ISFOG). Perth, Australia, Tayler Francis Group.
- Houlsby, G.T., Ibsen, L.B., and Byrne, B.W.(2005c) “ Suction caisson for wind turbines” Department of Civil Engineering, Aalborg University Denmark, Department of Engineering Science Oxford University UK.
- Ibsen L.B., Hanson, M Hjort, T. and Taarup, M. (2009) “MCPParameter Calibration for Baskarp Sand No. 15” DCE Technical Report No.62. (ISSN 1901-726X), Aalborg University, Department of Civil Engineering, Aalborg, Denmark.
- Ibsen, LB, Barari, A, and Larsen, KA (2012). “Modified vertical bearing capacity for circular foundations in sand using reduced friction angle,” *Ocean Engineering* 47 (2012) 1-6, Elsevier Ltd.
- Ibsen, LB, Barari, A, and Larsen, KA (2013). “Calibration of Failure Criteria for Bucket Foundations on Drained Sand under General Loading,” *Journal of Geotechnical and Geoenvironmental Engineering*, American Society of Civil Engineers.
- Ibsen, LB, Barari, A, and Larsen, KA (2014a). “Adaptive Plasticity Model for Bucket Foundations,” *Journal of Engineering Mechanics*, Vol. 14, Number 2. American Society of Civil Engineers. ISSN 0733-9399, CODEN: JENMDT.
- Ibsen, LB, Barari, A, and Larsen, KA (2014b). “Evaluation of Vertical Bearing Capacity of Bucket Foundations in Saturated Sand,” *International Journal of Geomechanics*, ISSN 1532-3641.
- Larsen, KA (2008). Static Behaviour of Bucket Foundations. PhD Thesis, Aalborg University, Denmark.
- Lehane, B. A., Schneider, J. A. & Xu, X. (2005) The UWA- 05 method for prediction of axial capacity of driven piles in sand. Proc. International Symposium ‘Frontiers in Offshore Geotechnics’. Perth, Australia, Taylor & Francis Group.
- Kelly, R. B., Houlsby, G. T. & Byrne, B. W. (2006). A comparison of field and laboratory tests of caisson foundations in sand and clay. *Getotechnique*, 56, No. 9, 617–626.
- Prandtl L. (1920) Über die Härte plastischer Körper, *Nachr. D. Ges.D.Wiss*, Göttingen 1920.
- Ovesen, NK, Fuglsang, LD, Bagge, G, and Krogsbøll, A (2012). “Lærebog i Geoteknik”, *Polyteknisk Forlag*, Lyngby, Denmark. ISBN10 87-502-1042-4, ISBN13 978-87-502-1042-9, pp. 223-230.
- Prandtl, L (1920). “Über die Harte plastischer Körper, *Nachr.D.Ges.D. Wiss.*” Gottingen.
- Rahman, MS, Wang, J, Deng, W, and Carter, JP (2001). "A neural network model for the uplift capacity of suction caissons," *Computers and Geotechnics* 28 (2001), Elsevier, pp 269-287.

- Randolph, M, and Gourvenec, S (2001). *Offshore Geotechnical Engineering*. Spon Press and imprint of Taylor & Francis, ISBN13: 978-0-415-47744-4(hbk), ISBN13:978-0-203-88909-1(ebk), pp 265-266.
- Randolph, M.F., Jamiolkowski, M. B. & Zdravkovic, L. (2004) Load carrying capacity of foundations. Proc. Skempton Memorial Conf. London.
- Schanz, T, Vermeer, PA, and Bonnier, PG (1999), “The hardening soil model: Formulation and verification”, *Beyond 2000 in Computational Geotechnics – 10 Years of Plaxis*, Balkema, Rotterdam. ISBN 90 5809 040 X.
- Senders, M (2008). Suction caissons in sand as tripod foundations for offshore wind turbines. PhD Thesis, The University of Western Australia.
- Terzaghi, K (1943). “Theoretical soil mechanics”, New York: Wiley.
- Vaitkunaite, E, Devant Molina, S, and Ibsen, LB (2012), “Comparison of Calculation Models for Bucket Foundation in Sand”, *DCE Technical Memorandum No. 17*, Aalborg University, Denmark, ISSN 1901-7278, 2012.
- Vaitkunaite, E, Ibsen, LB, and Nielsen, BN (2014), “New Medium-Scale Laboratory Testing of Bucket Foundation Capacity in Sand”, *Proceedings of the Twenty-fourth International Ocean and Polar Engineering Conference*, Vol. 2, Busan, pp. 514-520.

## 4.2 Soil-structure interaction / axial pile loading (FhG-H)

### 4.2.1 Motivation

The aim of this section of Deliverable 4.1.2 is to give an overview of design methodologies that has to be investigated in more detail in order to enable more realistic and more cost efficient substructures with optimized or more reliable foundation designs.

The following aspects are of main interest in view of a jacket design for WTG of 10 MW class and more:

1. An important scenario to be investigated is the large pile diameter effect resulting from different scale effects that are no more negligible in case of larger pile diameters,
2. cyclic loading effects, with respect to one-way and two-way loading modes
3. and the effect of combined loading of lateral and vertical loads.

Therefore, numerical studies as well as experimental model tests have to be set-up. Potential outcomes of these investigations are expected to reveal a better insight into the following topics:

1. Evaluation of the potential influence of pore water pressure effects during loading and the scale effect in case of larger pile diameter
2. The development of a pressure ring after cyclic loading is an important effect to be investigated as it may result in a decrease in shaft resistance due to a potential shading of earth pressure acting on the pile shaft

Based on the findings, recommendation for experimental test setups can be specified and applied in virtual experiments conducted within numerical simulations.

### 4.2.2 Approach

The numerical analyses needed for the investigation of the pile bearing behaviour require two modeling approaches that consist of two sets of multi-body or finite element models that have to be set-up:

- a. a model of the reference jacket structure representing the structural dynamics and deriving the load transfer to the pile heads (Model A)
- b. and a model representing the soil-structure interaction (Model B)

### 4.2.3 A support structure model for time domain analysis (Model A)

The purpose of this model is to predict load series and extreme loads at the pile heads in order to investigate the cyclic behaviour and possible degradation of the pile bearing capacity by cyclic loading and stress rearrangement resulting in a decreased shaft friction.

Based on these time series, prediction in finite element model (Model B) can be carried out, e.g. the build-up of pore water pressure in combination with plastic volumetric strains.

The analysis of structural dynamics can either be performed in multi-body or finite element simulation frameworks. Both are carried out in this report: The multi-body approach (Model A1) is performed with application of the simulation program Adams, while Abaqus is applied for the finite element approach in Model A2.

**Model A1 – a multi-body approach.** Figure 4.2-1 shows a 3D view of the structural jacket model in RFEM 5 (Dlubal Software) being the basis for the generated multi-body model applied in the simulation software Adams. For the prediction of wave loads, the program WaveLoads, developed within the GIGAWIND research project at Leibniz Universität Hannover, is included into the time domain analysis. In doing so, the movements and thus the resulting interaction of the structure with the water body are considered during wave load and buoyancy load calculation.

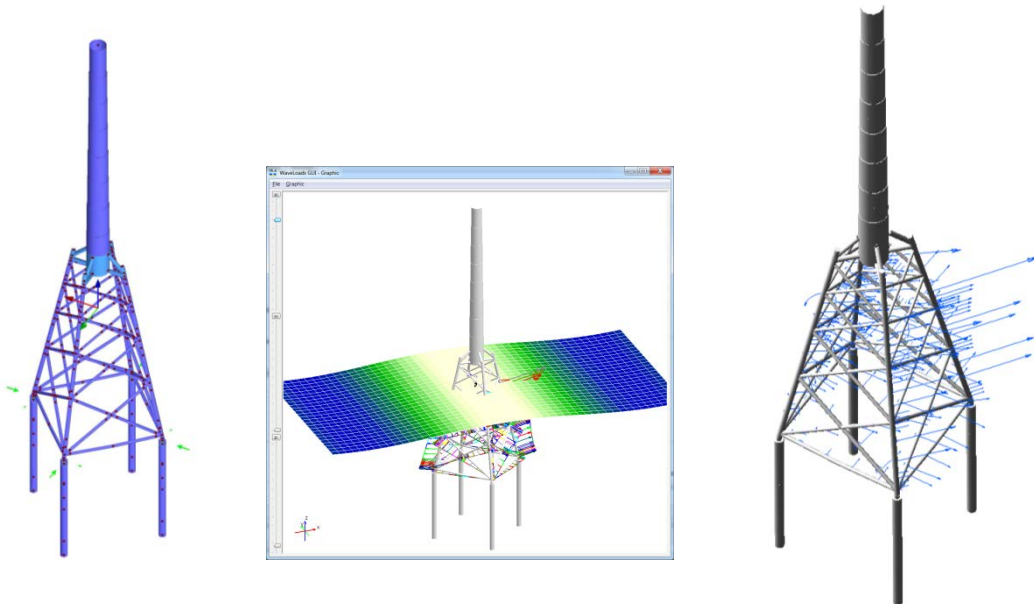


Figure 4.2-1: Model of the reference jacket in RFEM5 (Dlubal Software) for structural dynamic analysis with fully coupled (wave-structure) interaction in a multi-body framework.

**Model A2 – a finite element approach.** In order to investigate the structural dynamics of the support structure coupled to the pile foundation, a finite element model has been set-up. It is been generated automatically by a Visual Basic for Application (VBA) program based on the reference jacket data provided by Rambøll in WP 4 [FhG-H2]. The jacket has been designed based on the DTU 10 MW reference turbine data given in [FhG-H1].

Based on the geometric and material data provided for the reference jacket a beam element model of the jacket is to be set-up including the piles and their nonlinear springs according to given  $p$ - $y$ ,  $t$ - $z$  and  $q$ - $z$  curves representing the load settlement or load deflection behaviour of the soil layer.

Figure 4.2-2 shows a 3-D view of the model of the resulting jacket support structure. It consists of finite beam elements representing the jacket members and the piles. The bearing behaviour of the piles is approximated by springs defined by the provided  $p$ - $y$ ,  $t$ - $z$  and  $q$ - $z$  curves. Within this model the wave loads on the structural members are calculated in a preprocessing step using the program WaveLoads. Gravity and buoyancy loads can also be taken into account for the structural analyses.

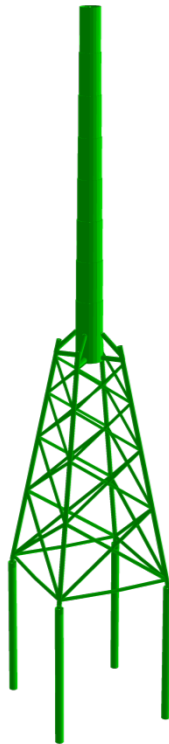


Figure 4.2-2: Model of the reference jacket for structural dynamics analyses coupled to a soil-structure interaction. The foundation model is represented by nonlinear springs distributed along the submerged pile length.

#### 4.2.4 A finite element model of the pile foundation for quasi static analyses (Model B)

In order to investigate the nonlinear behaviour of the pile due to cyclic or extreme loadings, a finite element model has been set-up in the simulation program Abaqus. The set-up procedure has been automated by an object-oriented program using the general purpose scripting language Python that is able to directly interact with the simulation program Abaqus. Thus, all pre and post process feature of Abaqus can be included into the pre and post processing strategy and applied during the simulation process. The script can thus be parameterized in order to perform parameter studies and automated simulation series. Figure 4.2-3 shows a 3-D view of the pile-soil model of the foundation. It consists of three dimensional finite elements (bricks) representing the elastic steel pile and the nonlinear soil material. The interface is defined by contact elements. The piling process is set-up in a simplified way by setting the initial stress state of the soil first, then replacing the soil elements by pile elements and including the required contact elements at the pile-soil interface.

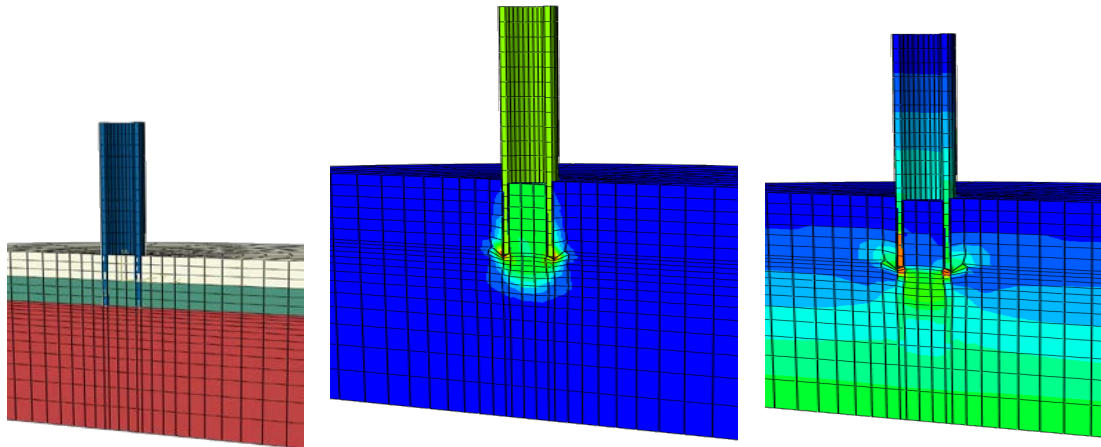


Figure 4.2-3: Exemplary model of the pile model for investigation of soil-structure interaction. Material groups (left), magnitude of displacements (middle) and von Mises stresses due to compressive settlement (right) of the pile (right).

A simplified approach is depicted in Figure 4.2-4. Here, also the initial stress of the overburden is set during the initial simulation steps. The soil material model is set to Mohr-Coulomb plasticity. For convenience the tubular pile is replaced by a substitutional pile with a full cross-section neglecting the soil in the interior of the pile.

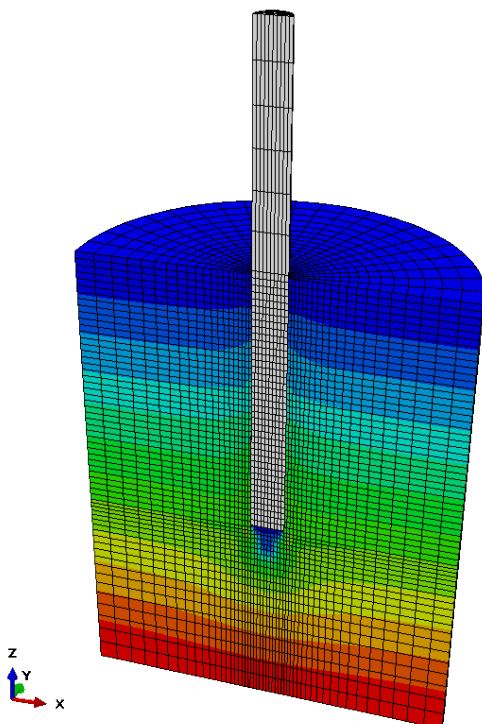


Figure 4.2-4: Exemplary finite element representation of the pile-soil model for investigation of soil-structure interaction. Von Mises stress during a pile pull out load test. The displacements are scaled by factor 1000 in order to visualize the deformations.

#### 4.2.5 Numerical model verification

The applicability of the model shall be demonstrated by performing eigenanalyses of the support structure and comparing the resulting natural frequencies against the values predicted by ROSAP and provided by Rambøll within Deliverable 4.3.1 [FhG-H2].

Two models have been set up. The first one is a jacket with legs that are fully clamped at bottom level (see Figure 4.2-5) and the second one is a jacket with a pile foundation approximated by beam elements with distributed nonlinear springs (see Figure 4.2-6).

For verification purposes the natural frequencies and the mode shape have been compared against those of the other programs used by partners (ROSAP by Rambøll and GH Bladed applied by the University of Oldenburg). The differences in the predicted natural frequencies compared to ROSAP and GH Bladed results are in an acceptable range in view of further dynamic pile load analyses, see Table 4.2-1.

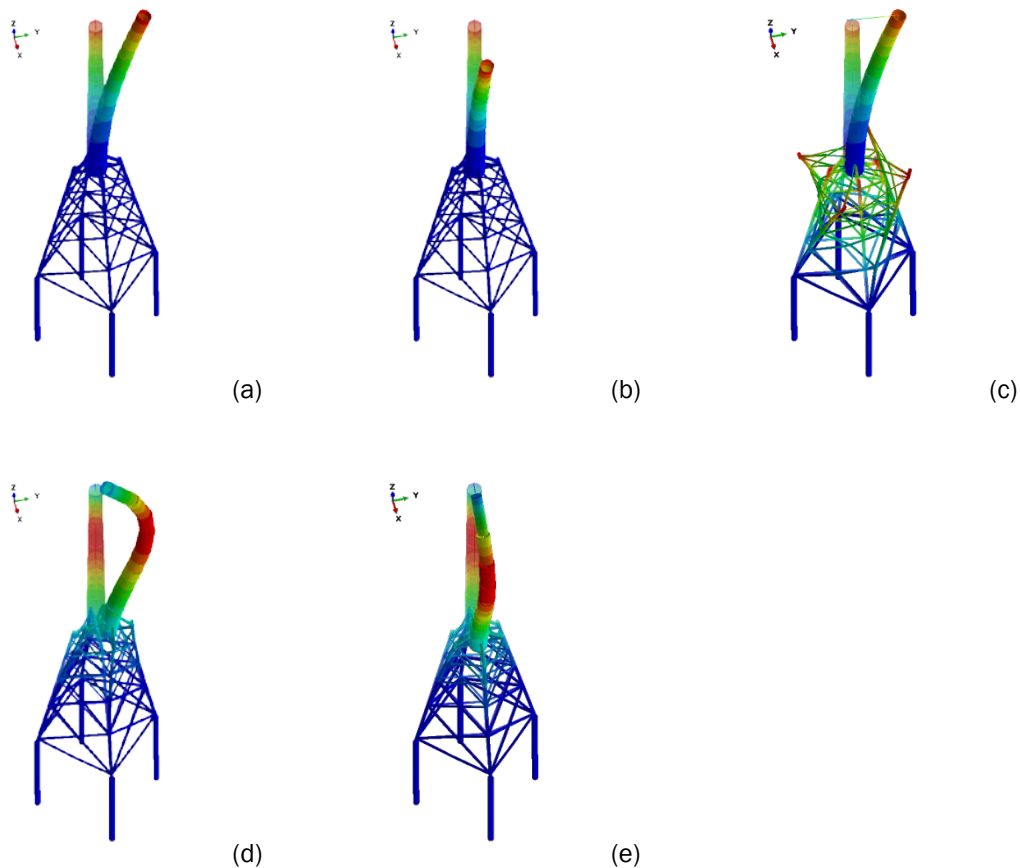


Figure 4.2-5: Reference jacket clamped at pile heads. Undeformed configuration of jacket support structure model with mode shape according to the natural frequencies of 1<sup>st</sup> bending (a - side to side, b - fore aft), torsion (c) and 2<sup>nd</sup> bending mode (d - side to side, e - fore aft).

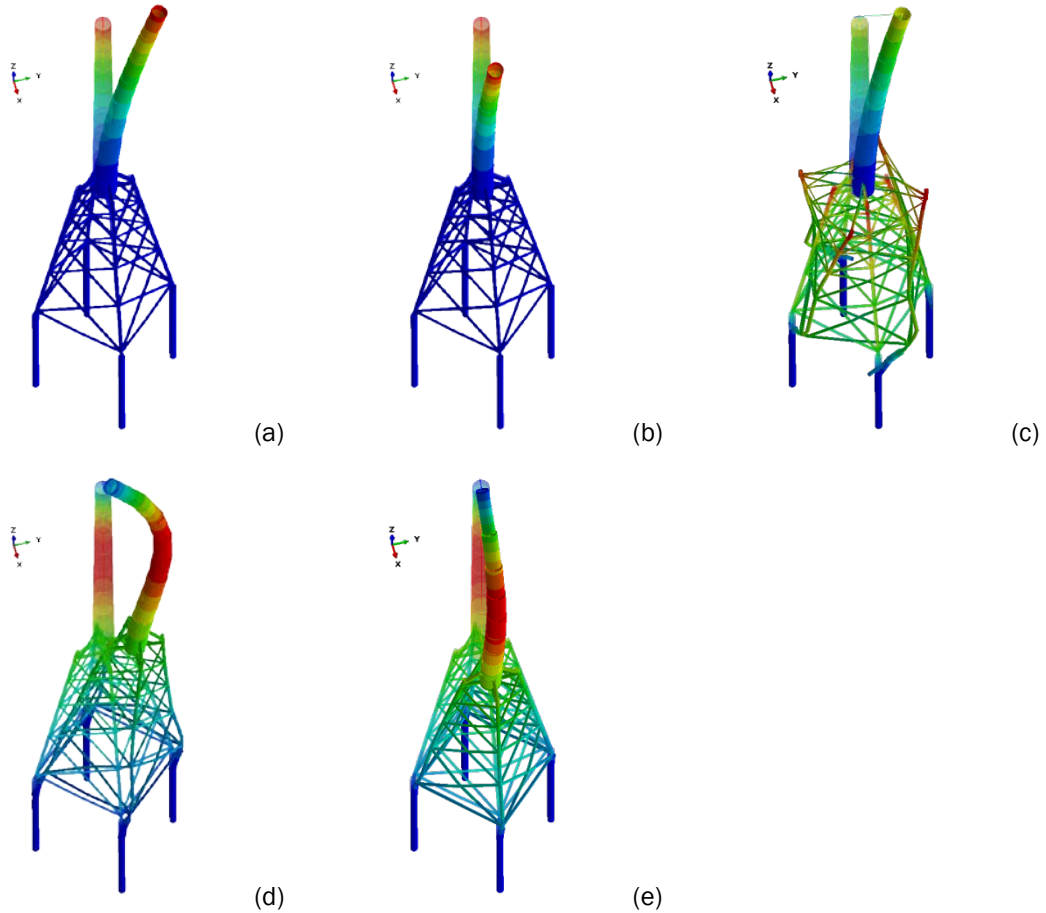


Figure 4.2-6: Reference jacket with pile foundation and approximation of soil behaviour by nonlinear springs. Undeformed configuration of jacket support structure model with mode shape according to the natural frequencies of 1<sup>st</sup> bending (a - side to side, b - fore aft), torsion (c) and 2<sup>nd</sup> bending mode (d - side to side, e - fore aft).

Table 4.2-1 Natural frequencies derived in the Abaqus model compared to ROSAP (Rambøll) and GH Bladed (University of Oldenburg) predictions.

	Model	1st Bending side-side	1st Bending fore-aft	Torsion	2nd Bending side-side	2nd Bending fore-aft
Natural Frequency (Hz)	Abaqus Jacket fully clamped at bottom level	0.29414	0.29599	1.0253	1.6338	1.7683
	Abaqus Jacket with pile foundation <sup>1</sup>	0.28828	0.28991	1.0138	1.4553	1.5248
	ROSAP	0.3246	0.3274	1.0298	1.7214	1.9024
	GH Bladed Jacket fully clamped at bottom level	0.328	0.331	1.171	1.699	2.046

<sup>1</sup>) Including nonlinear springs according to p-y, t-z and q-z curves.

As also predicted by other partners the resulting natural frequencies of a simplified approach with a jacket fully clamped at the bottom level are not very different from those of a jacket with a pile foundation model. Accordingly, the results predicted here have more significant differences only for the higher modes. Thus, the 2<sup>nd</sup> bending mode shows higher differences in the predicted natural frequencies, see Table 4.2-1.

#### 4.2.6 Identification and discussion of innovations on component level

**Review of test results on the bearing behaviour of axially loaded piles.** Experimental findings according to the cyclic axial pile behaviour do show distinct results. Cyclic loads usually result in a post cyclic variation in pile capacity. Usually a resulting degradation is described in literature e.g. [FhG-H3] or [FhG-H4]. The degradation of the pile capacity can be derived from interaction diagrams depending on the combination of average and cyclic load level. Nevertheless, in the literature also pile load tests are mentioned that result in increasing pile capacities ([FhG-H5], [FhG-H6]).

**Review of recommendations for the improvement of pile design.** Within observations of the soil movement near the pile shaft made by Thomas [FhG-H13], it could be shown that phenomena, specific to cyclic loads, are caused by particle rearrangements. He observes a shear zone near and a shear band being established during cyclic loading and distinguishes between one-way and two-way loading. Thus, he mentions the hypothesis that two-way loading causes a pressure ring in the shear band which decouples radial stresses from the pile shaft and thus results in a worse pile behaviour compared to one-way loading. Thomas also recommends further investigations of the pile behaviour in saturated soil with respect to conditions that may generate pore water pressures. The potential appearance of these effects has been described by Taşan et al. in [FhG-H8], based on a coupled two-phase model and a hypoplastic constitutive model they numerically demonstrate the importance and relevance of the consideration of pore water pressure accumulation with monopole soil systems subjected to offshore loading conditions. Fully coupled two or even three phase models, as described in [FhG-H10], combined to appropriate plastic constitutive models are to be used in order to investigate and to prove or disprove potential effects of pore water pressure with respect to axially loaded pile of large jacket support structures.

In case of pile design configuration with shorter pile length, resulting in a more compact pile geometry, the lateral pile behaviour becomes more important. In this case, Achmus and Thieken [FhG-H9] describe that the interaction of horizontal and vertical load becomes more relevant. Therefore, existing experimental investigations on laterally loaded piles (see e.g. [FhG-H12]) and axially loaded piles (see e.g. Thomas [FhG-H13]) should be taken into account and experiments with combined (horizontal and vertical) loading should be designed.

#### 4.2.7 Interim conclusion and assumed impact of innovations on component level

At the current status the impact of potential innovations on component level with respect to an axially loaded pile is hard to predict. The statement that liquefaction may occur due to pore water pressure accumulation has to be disproved with respect to pile sizes and lateral load characteristics being expected for the investigated jacket support structures.

Using the multi-body and finite element models described in the previous sections, numerical studies of the pile bearing behaviour also with regard to potentially scale effects can be carried out. The expected impacts are as follows:

1. One of the most important effects is the development of the stress field within the shear zone near the pile shaft and within the shear bands and its resulting influence on the shaft friction behaviour. The profound understanding of the processes within these zones is of fundamental importance.
2. A suggested innovation is the application of shorter pile embedding lengths. These compact piles with a smaller length-to-diameter ratio show a stronger influence of

interaction effects between lateral and axial loads [FhG-H9] that should be taken into account.

3. Further research on cyclic loading effects, which is still the most unknown process, could result in innovations in the design recommendations that might also have favorable impact with respect to a reduction of safety factors.

#### 4.2.8 Required experimental investigations on innovations on component level

**Test Center for Support Structures Hannover.** In the Test Center in Hannover support structures and foundation systems are to be investigated in physical experiments at large scales models of 1:10 to 1:3.5 Design studies and construction methods can be validated and optimized. Therefore, a foundation test pit and a span are available, see Figure 4.2-7. Several special laboratories supplement the facility. They are designed for measurement and test engineering, for concrete and composite materials and for geotechnical investigations.

In the foundation test pit with its depth of 10 m the behaviour pile foundations and especially their soil-structure interaction can be investigated in detail within reproducible experiments.

The Test Center is a facility of the Leibniz Universität Hannover and the ForWind Research Center. It is operated by the Fraunhofer IWES Northwest.

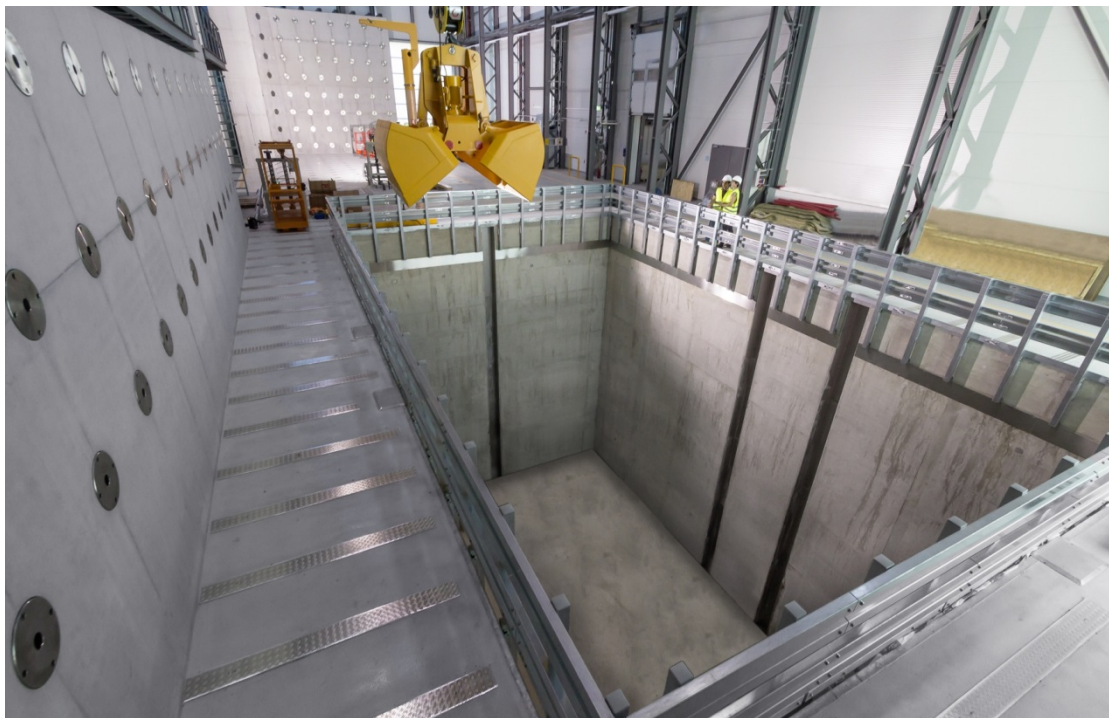


Figure 4.2-7: Foundation test pit with abutment wall (front) and span (rear).

**Large scale model experiments.** The experiments planned within the INN WIND project focus on the foundation test pit capabilities. The main feature of the test pit is the possibility to apply high level cyclic loads in multi-axial directions. Thus, horizontal loads can be applied using the abutments wall or additional steel supports anchored on the ground anchor bars. Portal steel frame supports are used for vertical loading.

Currently planned physical experiments focus on piles with diameters of about 0.5 m, see Figure 4.2-8, but experiments with larger specimens may be set-up.

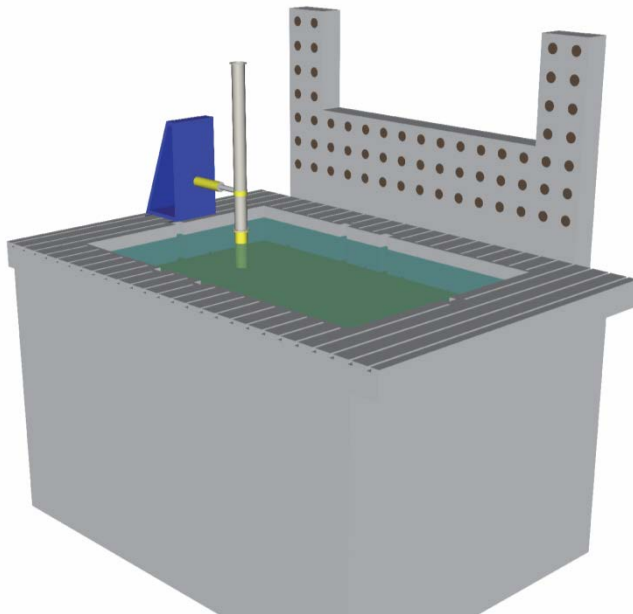


Figure 4.2-8: Exemplary sketch of physical experiments on pile-tower dynamics in the foundation test pit.

**Recommendations on test objectives and specifications.** The objectives of experimental tests that should be carried out are still the more profound understanding of

a) Vibratory pile driving in comparison to impact pile driving with respect to pile bearing capacity: Vibratory pile hammers are best suited for sandy soils. Vibratory hammers are less noisy and do not cause pile damage compared to pile driving hammers. One of the major problems of vibratory hammers is the unavailability of credible methods to compute the bearing capacity of piles based on penetration rates.

In spite of the increasing use of vibrators and the rapid development of vibrator technology, many aspects of pile-soil interaction are not yet fully understood. One major limitation is that at present, the bearing capacity of vibratory driven piles is difficult to predict.

b) Influence of cyclic loading: The reduction of pile load capacity can be predicted by interaction diagrams (references are made in [FhG-H11], Annex D). The application of interaction diagrams is problematic, especially with respect to the restricted experimental data base and in case of two way loading combined with large load amplitudes.

c) Effects of pore water pressure: Negative influences due rising pore water pressure are assumed to be important for a larger pile diameter only. Nevertheless, the investigation of pore water effects might be interesting with respect to vibratory pile driving and its influence on penetration velocity. The pore water is also important with regard to the prediction of the resulting bearing capacity based on penetration rates.

d) The influence of multi-directional horizontal loading compared to unidirectional horizontal loading direction and its influence on cyclic degradation might also be an important study to be considered within further research.

## References

- [FhG-H1] DTU10MW Reference Turbine Data Sheet. DTU excel-sheet, version 1.04, 11/05/2013.
- [FhG-H2] Thomas von Borstel (Rambøll): Design Report – Reference Jacket, Deliverable 4.3.1, Task 4.3.
- [FhG-H3] McManus, K. J., Kulhawy, F. H.: Cyclic axial loading of drilled shafts in cohesive soil. *Journal of the Geotechnical Engineering Division* 120 (1994), No. 9, pp. 1481–1497.
- [FhG-H4] Lehane, B. M., Jardine, R. J., McCabe, B. A.: Pile group tension cyclic loading: Field test program. Kinegar N. Ireland, Imperial College Consultants (ICON), Research Report No. 101,
- [FhG-H5] Turner, J. P., Kulhawy, F. H.: Drained uplift capacity of drilled shafts under repeated axial loading. *Journal of the Geotechnical Engineering Division* 116 (1990), No. 3, pp. 470–491.
- [FhG-H6] Baumbach, J.: Beitrag zum Tragverhalten von Mikropfählen unter axial zyklischer Belastung in bindigen Böden. Lehrstuhl und Prüfamf für Grundbau, Bodenmechanik, Felsmechanik und Tunnelbau der Technischen Universität München, Dissertation, 2013.
- [FhG-H7] Coyle, H. M., Reese, L. C.: Load transfer for axially loaded piles in clay. *Journal of the Soil Mechanics and Foundation Division*, Vol. 92, No. 2, 1966, pp. 1–26.
- [FhG-H8] Taşan, H. E., Rackwitz, F., Savidis, S.: Porenwasserdruckakkumulation bei zyklisch horizontal belasteten Monopiles mit großen Durchmessern, *Bautechnik* 87, Heft 8, 2010.
- [FhG-H9] Achmus, M., Thieken, K.: On the behavior of piles in non-cohesive soil under combined horizontal and vertical loading, *Acta Geotechnica*, 5:199–210, 2010.
- [FhG-H10] Kohlmeier, M.: Coupling of thermal, hydraulic and mechanical processes for geotechnical simulations of partially saturated porous media. Institut für Strömungsmechanik, Leibniz Universität Hannover, PhD thesis, Bericht Nr. 72, 2006.
- [FhG-H11] DGGT (Deutsche Gesellschaft für Geotechnik e.V./ German Geotechnical Society) (Editor): *Recommendations on Piling (EA Pfähle)*, Wiley, 2013.
- [FhG-H12] Reese, L. C., Van Impe, W.: *Single Piles and Pile Groups Under Lateral Loading*, 2nd Edition, 2011.
- [FhG-H13] Thomas, S.: Zum Pfahltragverhalten unter zyklisch axialer Belastung. PhD thesis, Heft 25, Universität Kassel, 2011.

### 4.3 Innovative Foundations (DTU)

#### 4.3.1 Piles for Jackets

In comparison with a monopile foundation, jacket foundation used for a wind turbine produces different loading conditions on the submerged piles, see Figure 4.3-1. The main difference is that vertical axial loads occur at the piles in addition to the horizontal loading originating from the turbine thrust. The thrust force positioned substantially far from the piles produces a significant bending moment at the mud level. In the case of a monopile configuration, this bending moment is fully taken by the monopile itself, however in the case of jacket structure serving as foundation the bending moment is taken by the piles as axial loading. The pile axial loads from the bending moment are further transferred to the soil and thus, the axial soil-pile interaction becomes an important factor in addition to lateral pile resistance in design of supporting piles for wind turbine jacket structures.

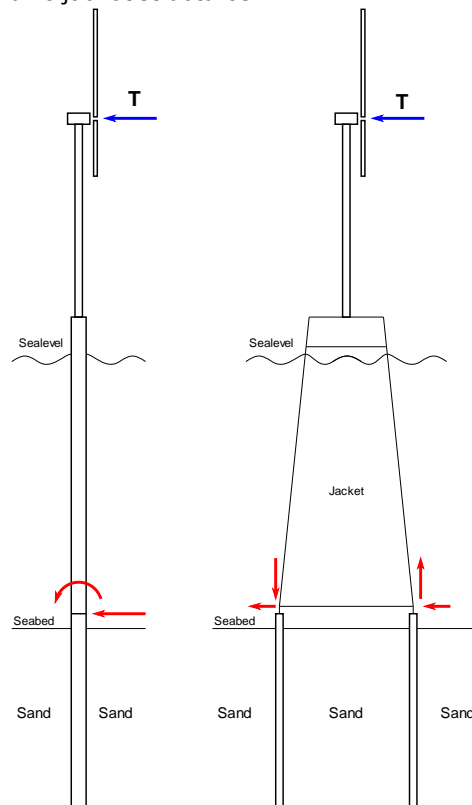


Figure 4.3-1: Typical pile loads (in red) generated by thrust (in blue) for monopile and jacket configurations.

#### Loads experienced by the piles

Two principal jacket orientations with respect to the wind and subsequently thrust directions are shown in Figure 4.3-2. It can be easily demonstrated that for a given thrust value, highest vertical loading occurs for the case (a), when two out of four piles barely experience any vertical loads induced by the thrust. At the same time the other two piles experience maximum push-in and maximum pull-out forces. Due to this reason only the described loading direction (a) has been presently considered.

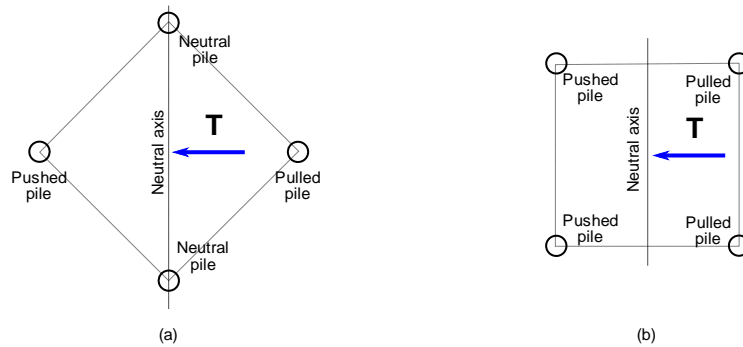


Figure 4.3-2: Pile loading in two principal trust directions.

### Possible innovations based on the problem definition

One of the first questions that comes up is if the original pile length of 40 meters provided by RAMBOLL preliminary design [DTU03] can be reduced without significantly affecting the WT structural response. The initial parametric study demonstrated that the original pile length was rather conservative both in terms of WT natural frequencies and aeroelastic response and it is likely to be reduced with negligible effect on the overall structure behaviour. See Figure 4.3-3 for variations of the fore-aft and side-side natural frequencies versus pile length in maximal thrust loading conditions.

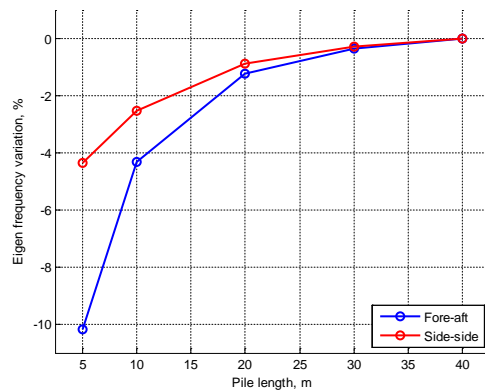
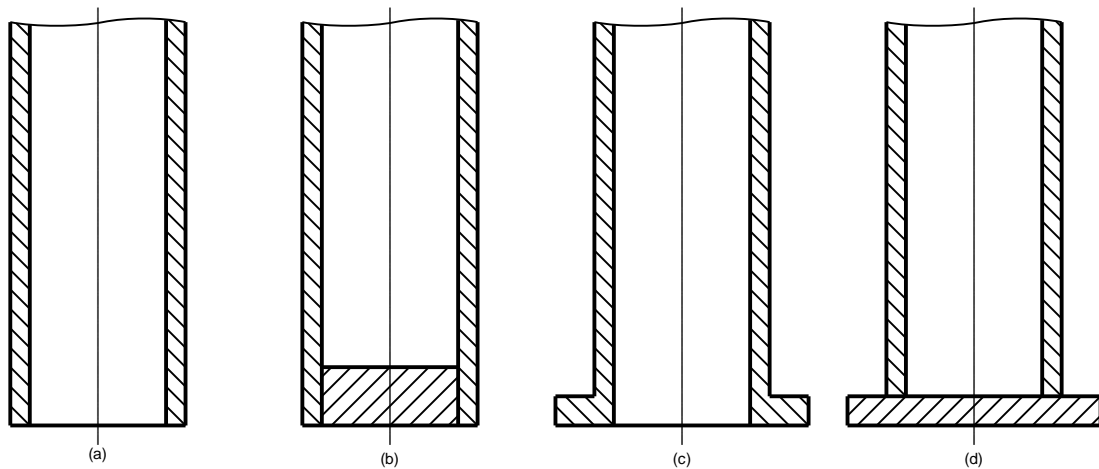


Figure 4.3-3: Effect of pile length on the turbine natural frequencies in maximum thrust conditions.

Further, it is expected that for possible shorter pile configurations the tip resistance will play more significant role in stiffness and strength of the jacket-pile foundation. For this reason the effect of increased pile tip resistance on the maximal pile deflections in extreme loading conditions is presently studied. Initially pile tip resistance is represented by a reaction force provided by the annulus of the pile tip wall (unplugged pile) in typical sandy soils of sea beds. Further, increased pile tip resistance is accounted for where the tip resistance is implemented piles with plugs for which pile gross area produces significantly larger reaction forces simply due to larger tip area, see sketches for both cases in Figure 4.3-4a and Figure 4.3-4b.

An ordinary pile, plugged or unplugged, produces tip resistance generated by the soil only when it is being pushed-in. A pile configuration that is capable of providing tip resistance when the pile is in pull-out condition can be an attractive approach, especially for configurations with shorter piles. Such a conceptual pile configuration could be implemented via special pile end like those sketched in Figure 4.3-4c and Figure 4.3-4d.



**Figure 4.3-4: Sketches of pile ends with innovative designs. a) – original unplugged pile, b) – original plugged pile, c) – unplugged pile with pull-out tip resistance, d) – plugged pile with pull-out tip resistance.**

Thereby, in the present investigation effects of two main concepts on the pile strength in extreme loading conditions are studied: effect of the magnitude of the regular pile tip resistance and effect of the pile tip with innovative design providing higher pull-out resistance capabilities.

#### **Aeroelastic model of the reference wind turbine on jacket foundation**

Aeroelastic multi-body dynamics code HAWC2 is presently used for numerical simulation of the structural response of the entire reference wind turbine on jacket foundation. Particular attention is paid to modelling of soil-pile interaction that is hereby implemented according to DNV Offshore Standard [DTU01] and API recommended practice [DTU02] based on the soil data and initial pile configuration provided by Ramboll [DTU03].

The HAWC2 code allows for modelling of lateral, axial and torsional reactions on piles from soil. These kinds of soil-pile interactions are modelled as systems of non-linear springs distributed along the submerged pile length, see Figure 4.3-5. The spring non-linear behaviour is input into HAWC2 by force-displacement relation as a function of spring position. The relation can be given only for positive pile displacements as the HAWC2 code automatically produces symmetrical response for the negative displacements. Plots of soil-pile interaction calculated for given soil properties and pile configurations are presented in Figure 4.3-6a and Figure 4.3-6b.

Thus, being non-linear, a soil spring in HAWC2 can only possess symmetrical behaviour with respect to the neutral point where no soil deformation exists. Due to this code particularity the pile tip resistance, asymmetrical in nature (as reaction force occurs only when a pile is pushed in), could not be directly represented using HAWC2 soil springs. Presently, for proper modelling of the pile tip resistance, the reaction force at the pile tip is calculated externally and fed into the HAWC2 simulations via dynamic library (DLL) interface. This approach provides correct non-linear and asymmetric pile tip resistance, however it was found that it cannot ensure application of an appropriate damping force at each time step due to the way HAWC2 is implemented. Therefore in the present investigation no damping of the pile tip movements is accounted for. Instead, compensation for underestimated soil damping was made by varying the soil damping at the axial soil springs.

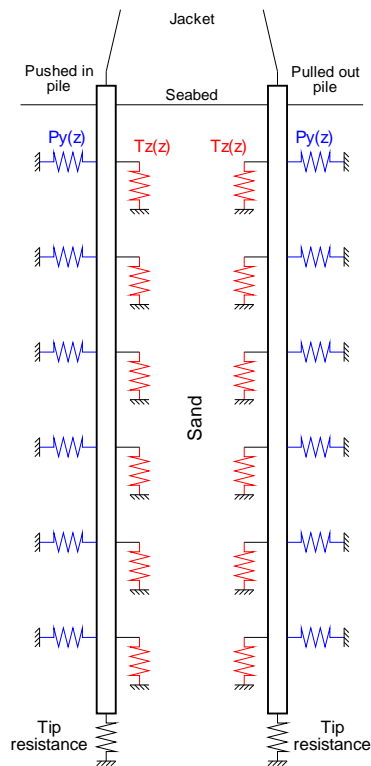


**Figure 4.3-5: Representation of soil in HAWC2 aeroelastic model setup.**

After numerical simulations of a set of design load cases (DLC) where the piles were subject to high push-in and pull-out loads it was found that the most critical case is DLC 2.3 where the turbine operates at maximum thrust and then experiences extreme wind gust with subsequent grid loss. The maximum thrust condition ensure high bending moment at the mud level and thus high axial loading on the front (pulled-out) and rear (pushed-in) piles. Extreme gust magnifies the loads produced by the maximum thrust, while grid loss occurring at a certain time point leads to inverse loading on the piles with nearly same high magnitudes due to return movement of the entire turbine. By performing trial model runs it was found that for the current turbine and controller configurations the worst case scenario occurs when the grin loss happens 2.5 sec. after the wind gust starts. This moment corresponds to the first local wind speed minimum within the gust profile, see Figure 4.3-7.

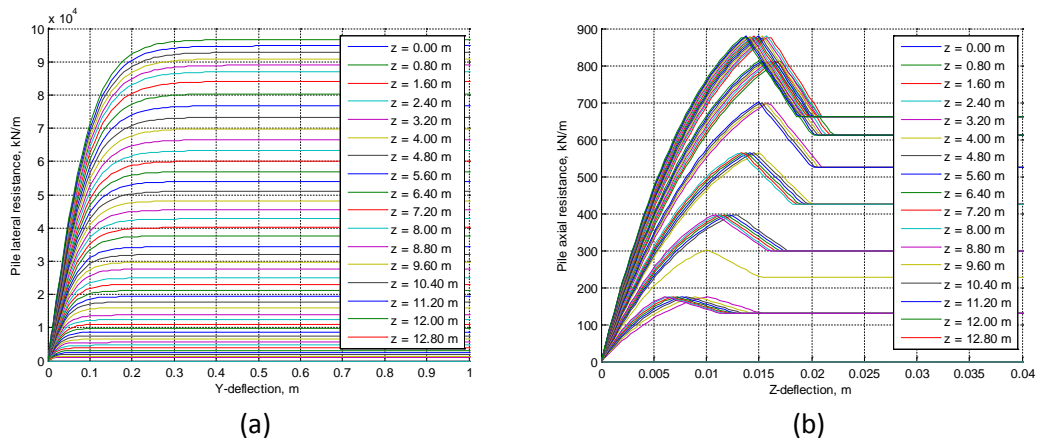


Figure 4.3-6: Soil-pile lateral (a) and axial (b) interaction as function of soil depth  $z$ . All soil depths are plotted but only depths up to 12.80m are included in the legends.

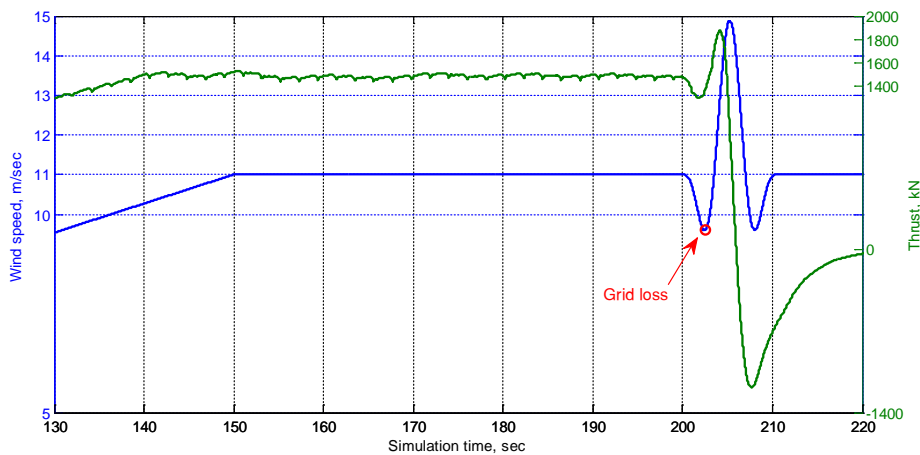
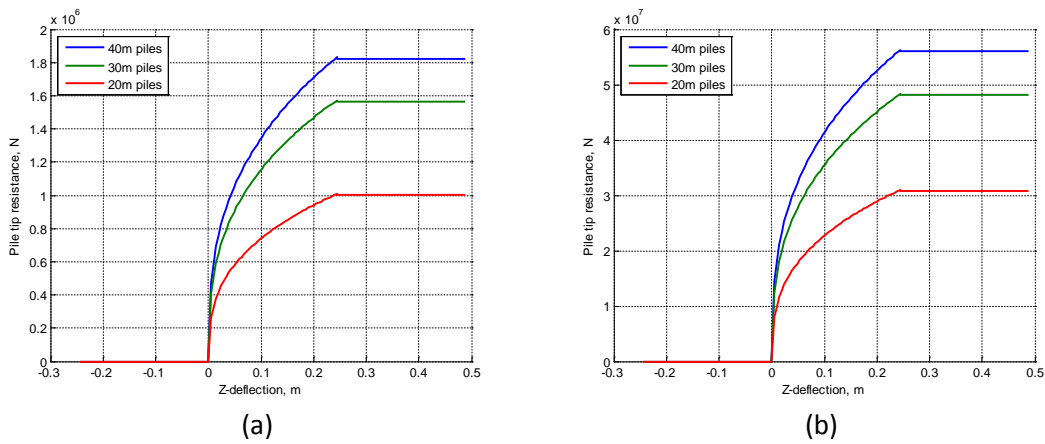


Figure 4.3-7: Wind speed, blue, and thrust, green, time series in DLC 2.3 (extreme gust and grid loss).

### Results comparing piles with Plugs versus unplugged piles

In the first set of considered pile configurations are the original piles with unplugged and plugged tips. Here, the tip resistance is considered to be original, without pull-out pile tip resistance and thus having ordinary tip resistance law as given in Fig. 8a for unplugged piles and 8b for plugged piles. The tip resistance vs. tip displacement law is calculated following the Recommended Practices by API [DTU02]. The aeroelastic calculations of the turbine response in DLC2.3 were performed for three pile length configurations: 40m, 30m and 20m piles. The pile length variations were assumed as simple pile cuts so that the 20m piles are the same 40m piles but cut 20m away from the mud line position.



**Figure 4.3-8: Tip resistance vs. tip displacement for original unplugged (a) and plugged (b) piles.**

As it was discussed earlier, to compensate for the damping effect of the pile tip resistance not included into the aeroelastic model, the damping of the soil springs corresponding to the axial soil-pile interaction (T-z springs) was varied by changing of the Rayleigh stiffness proportional damping coefficient of the axial soil springs from the original value of 0.01 up towards 0.015 and down towards 0.005 with a step of 0.0025. It was found that the maximal pile axial displacements always occur at the front piles as pull-out displacements; the rear pile push-in displacements were found to be slightly lower in magnitudes and therefore the more conservative front pile displacements are used as indicative. Results of the aeroelastic simulations of the reference wind turbine with unplugged piles in DLC 2.3 are given in Figure 4.3-9.

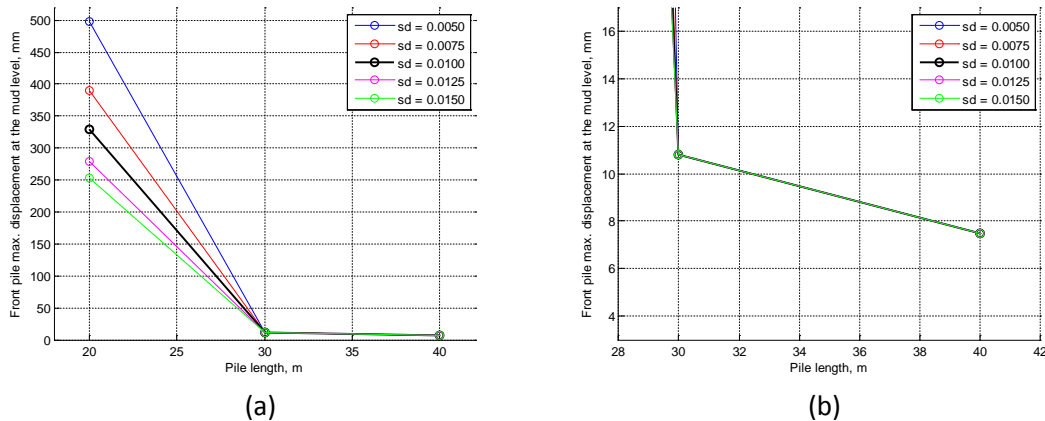


**Figure 4.3-9: Unplugged original piles. Maximum axial displacements of the front (pulled-out) pile at the mud level in DLC 2.3. A – all three pile configurations, b – zoomed in plot at 30m and 40m pile configurations.**

One can immediately observe that both 40m and 30m unplugged pile configurations demonstrate very similar axial displacements which are well within the upslope part of the t-z curves of the soil springs, see Fig. 6b. Thus it is likely that the original pile length could be shortened by about 10 meters without significantly affecting the pile foundation strength. Next, it becomes clear that the dynamic responses of the 30m and 40m unplugged pile configurations do not change with variation of soil damping. However, simulations of the turbine with plugged piles showed some local instability effects due to very large tip resistance forces and absence of damping at the pile tip. The instabilities were represented by axial oscillations of the piles which generated significant noise in the output results of the simulations. As at this stage it was not possible to properly introduce pile tip damping into HAWC2 the results obtained for plugged piles

can be treated only as qualitative, see Fig. 10. The only thing which is clear is the maximum pile axial displacements decreased for all pile configurations and became less than 7 mm for both 30m and 40m pile configurations.

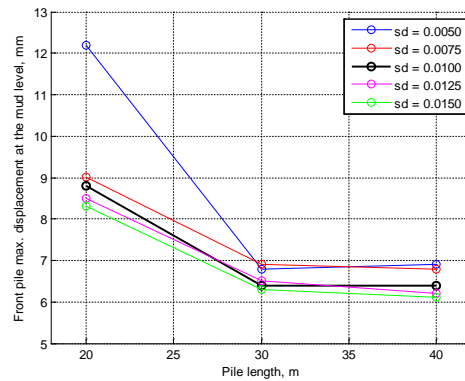


**Figure 4.3-10: Plugged original piles. Maximum axial displacements of the front (pulled-out) pile at the mud level in DLC 2.3.**

To model the piles with pull-out tip resistance the effective pile tip area acting either in push-in or pull-out direction was taken as a basis for calculation of the tip resistance values. When the pile is being pushed-in an ordinary tip resistance law according to API Recommended Practice [DTU02] is applied with the effective pile area. When the pile is being pulled-out the effective area is typically smaller and thus, the same approach can be used but with appropriate smaller effective area. One can safely assume that pile tip designs with the pull-out effective areas of 50% of the push-in effective areas are feasible, e.g. see Figure 4.3-4c and Figure 4.3-4d. This is accounted for in the present investigation and the pull-out tip resistance is assigned as 50% of the tip resistance acting in the pile push-in direction. The obtained tip resistance laws are presented in Figure 4.3-11a and Figure 4.3-11b.

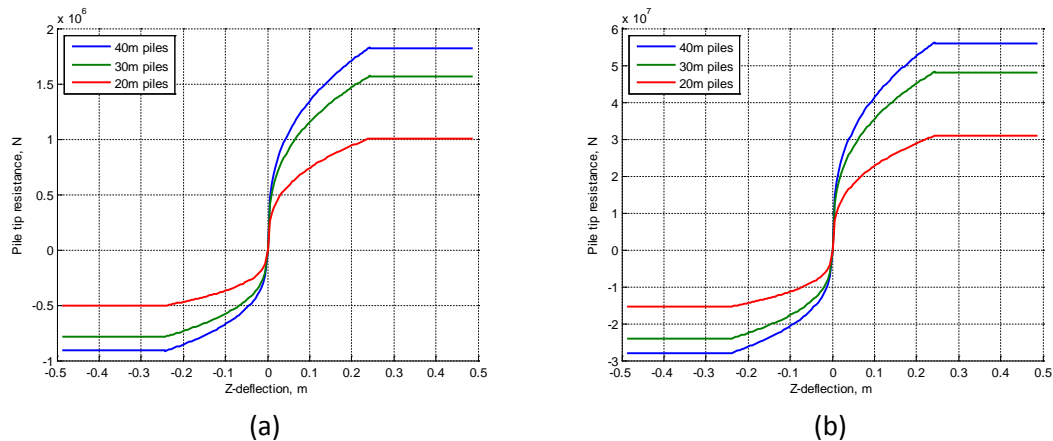


**Figure 4.3-11: Tip resistance vs. tip displacement for unplugged (a) and plugged (b) piles with pull-out tip resistance. Effective pull-out area is 50%.**

Similarly to the pile configurations with original tip resistance, the results for the pile configurations with pull-out tip resistance are given as front pile maximum axial displacements at the mud level, Figure 4.3-12. Damping of the axial soil springs was varied around its original value of 0.01 to account for the tip damping not included into the model and to study general effect of soil damping. As seen from the results for the piles with pull-out tip resistance, the pile displacements and therefore behaviour of the turbine structure did not change any significantly from when the original pile tip configurations are used (Figure 4.3-9). This indicates that all three

considered pile designs are insensitive towards the pile pull-out tip resistance. Additionally, sensitivity to damping is noticed only for the short 20m pile configurations.

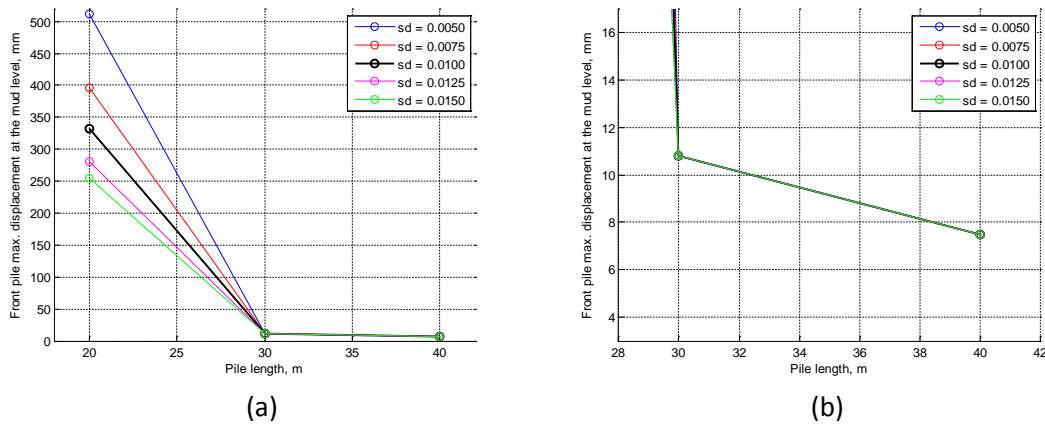


**Figure 4.3-12: Unplugged piles with pull-out tip resistance. Maximum axial displacements of the front (pulled-out) pile at the mud level in DLC 2.3. A – all three pile configurations, b – zoomed in plot at 30m and 40m pile configurations.**

Alike in the case of the original pile tip configurations, larger tip resistance forces for the plugged piles with pull-out tip resistance generated significant noise in the output results as no tip damping was included in the model. This led to preliminary results presented in Figure 4.3-13, which still indicate similar low magnitudes of pile-axial displacement.

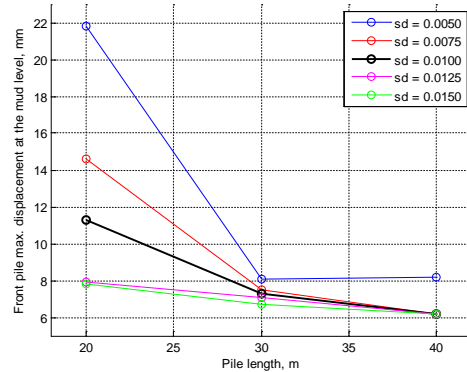


**Figure 4.3-13: Plugged piles with pull-out tip resistance. Maximum axial displacements of the front (pulled-out) pile at the mud level in DLC 2.3.**

### Conclusions on Piles for Jackets at 10 MW

The initial pile configuration for jacket foundation provided by RAMBOLL is found to be rather conservative with respect to pile length. More than the shear resistance along the pile length, it is the pile tip resistance that is a major design driver. Reduction of the pile length is expected to produce minimal impact on overall WT structural response.

Significant pile length reduction of ca. 10m is found to be feasible especially together with certain modifications to the pile configurations such as with the addition of a pile tip plug. The higher pile tip resistance could ensure low pile axial displacements in the most critical design load case which found to be DLC 2.3 with maximum thrust with extreme wind gust and consequent grid loss.

Additionally, the aeroelastic response of the entire wind turbine structure with considered pile designs with pile lengths of 30-40 meters is found to be almost insensitive to variations of soil damping characteristics.

### 4.3.2 Universal Articulated Joint as an Innovative foundation

A new platform has been design for water depths of 50 m for the 10MW DTU reference wind turbine (RWT) [DTU04]. The goal of this new design is to look for a cheaper alternative for 50 m water depth than the traditional jacket structure. The new platform is a semi floating platform strongly anchored to the seabed with a spherical joint. The sub structure includes a mooring system, a laminated rubber articulated joint and a floater composed of two different bodies: a steel cylinder and a buoyancy chamber. Figure 4.3-14 describes the assembly of the sub structure. The various parts are described herein.

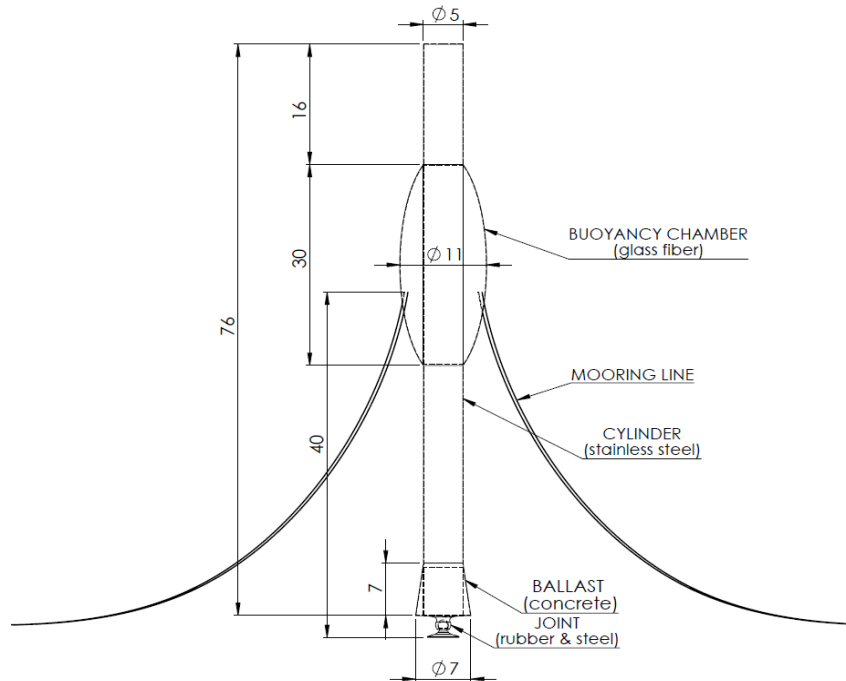


Figure 4.3-14: Design of the Semi floater substructure

### MOORING SYSTEM

The mooring system used has 6 mooring lines (see Figure 4.3-15), located each 60 degrees around the turbine. The locations of the mooring lines are: +30°, +90°, +150°, +210°, +270° and +330° (considering 0° as the direction perpendicular to the rotor plane, downwind). The length of each mooring line is 500 m. The weight per unit of length of the line is 113.35 kg/m in air and 108.63 kg/m in water. The diameter of each mooring line is 7.66 cm. The material used for the mooring lines is stainless steel alloy (16 GPa Young's modulus).

The anchoring point of the mooring system in the platform is at 40 m above the mud level. The anchors are located equidistantly in a circle of 500 m radius centered at the joint at the mud level.

The fairlead points are located in a horizontal plane at 40 m above the mud level in a circle of radius 8 m centered in the longitudinal axis of the floater. The link between the fairlead point and the floater includes the delta connection of the mooring lines. The delta connection consists of the

division of each of the mooring lines into two lines that are directly connected to the exterior surface of the floater (see Figure 4.3-15). The delta lines increment the torsional stiffness of the system.

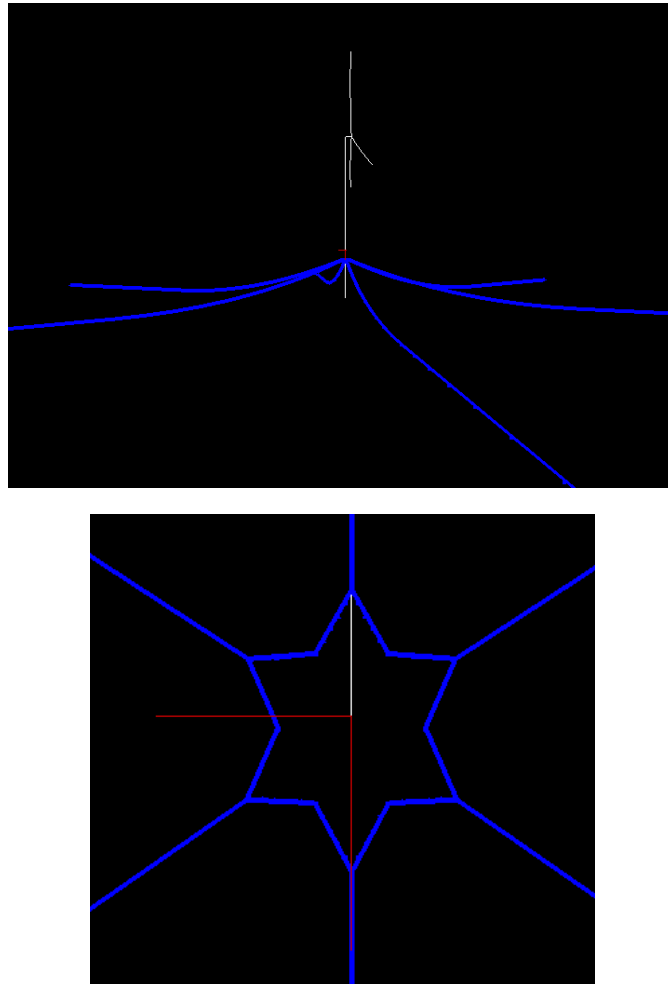


Figure 4.3-15: Details of the mooring system with Delta Connection.

### Articulated Joint

The joint used in this project is a similar joint to the one described in [DTU05]. This joint is a spherical joint with the particularity that has some torsional stiffness. This stiffness is achieved due to the construction of the joint. It includes some layers of rubber that produce friction when they are displaced relatively from each other.

The values assumed for the joint have been taken from [DTU05]. A diagram of the joint can be seen in Figure 4.3-16. The rotational stiffness is achieved thanks to the resistive moment to imposed rotation generated at the rubber layers of the joint.

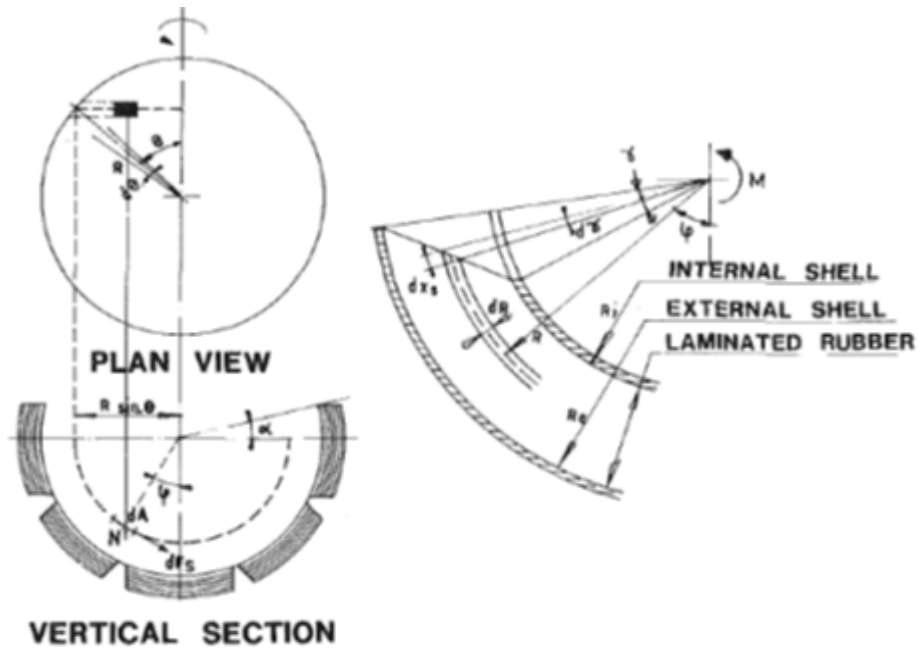


Figure 4.3-16: Joint response to imposed rotation (taken from [5])

That moment has been measured as:

$$M = \frac{4(\pi + 2\alpha)}{3} \gamma G \frac{R_i^3 R_e}{nt}$$

Where:

$(\pi + 2\alpha)$  → angular spread of articulation

$R_e$  and  $R_i$  → external and internal radii of the joint ( $R_e = 1.918\text{m}$ , and  $R_i = R_e - nt$ )

$nt$  → number and thickness of the rubber layers (assumed  $0.135\text{ m}$ , from [DTU05]).

$\gamma$  → pitch angle of the tower

$G$  → elastomer shear modulus ( $G = 50\text{ MPa}$ , natural rubber)

$A$  → joint area

Solving the formula for the values defined in [DTU05], Figure 4.3-17 is obtained which plots the restoring moment versus the pile deflection.

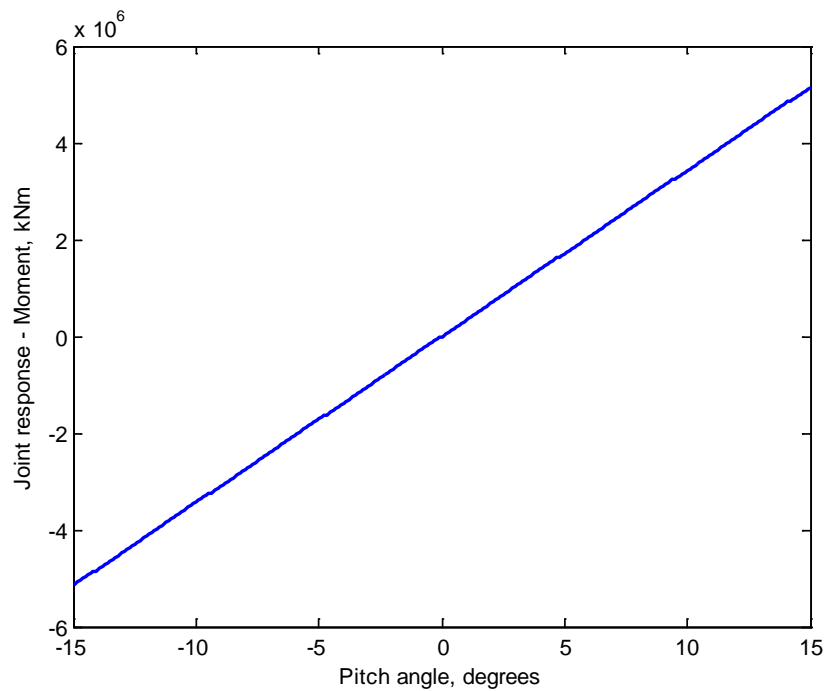


Figure 4.3-17: Resistive moment depending on the pitch angle of the platform.

To implement this rotational stiffness in an aeroelastic software such as HAWC2, a virtual body foundation was defined. This body does not exist in the real model, but is used so that a representative cantilever whose free end bending moment is the same as the universal joint can be made. This body is defined as a cantilever beam with a moment applied on its free end.

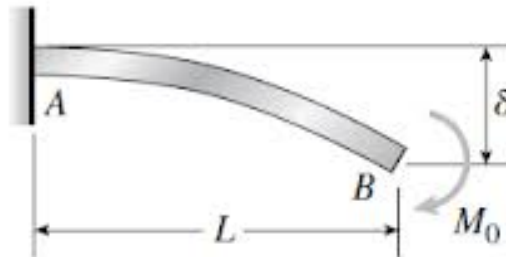


Figure 4.3-18: Scheme of the beam (foundation) body.

Solving the moments and efforts the following equation is obtained:

$$M = \theta \cdot \frac{EI}{L} \quad \text{Equation 1}$$

Where E is the Young's modulus, I represents the inertia and L the length of the element. To minimize the value of the displacement in the free end ( $\delta$ ), the value of the length (L) has been chosen as only 40 cm.

Matching equations 1 and 2, the following relationship has been found:

$$\frac{EI}{L} = 1.9678 \cdot 10^{10} \quad \text{Equation 2}$$

Its mechanical properties (inertia, length, Young's modulus) have been defined accordingly to fulfil the requirements of Equation 1.

## Platform Assembly

The platform is the most critical element of this study. The platform should be designed so that it is stiff enough to keep the wind turbine stable and for an operational life period of 25 to 30 years.

Besides, the platform should displace a volume of water big enough to create a buoyancy force that balances the weight of the whole system (wind turbine and the platform itself). That volume of displaced water needs to create a restoring moment capable of keeping the pitch angle of the platform in an operational range.

To fulfil these two goals (structural resistance and creation of restoring moment), the platform has been divided into two different bodies that are fully coupled to each other: a buoyancy chamber made with composite and a steel cylinder. The geometry of the steel cylinder is described later on. The buoyancy chamber has a shape of an ellipsoid.

The dimensions of these two bodies have been calculated through a static analysis in Matlab. In that analysis, the following forces have been considered: wind thrust, joint response, weight of the turbine, weight of the platform, the buoyancy force generated by the platform, the restoring moment created by the platform itself when it tilts over the joint and the wave forces when they hit the platform (these forces depend on the platform geometry)

- Wind thrust: the averaged wind thrust measured for each wind speed at the whole rotor has been considered as a static force. Its application point is the centre of the rotor. The moment that this force generates depends on the pitch angle of the platform.
- Joint response: the joint response has been considered as a moment applied at the joint. Its value depends on the pitch angle of the platform. It has been calculated using equation 1.
- Weight of the turbine: according to the data provided by reference turbine [DTU04], the weight of the turbine has been calculated from addition of the weight of the blades, hub, shaft and tower (the tower model used was the short version of the tower for the jacket substructure designed by Ramboll). The centre of mass has been used as the application point of the weight in order to calculate the moment produced by the weight.
- Weight of the platform: the own weight of the platform (including the cylinder and the buoyancy chamber) has been considered.
- Buoyancy force and restoring moment: depending on the geometry of the platform and on its pitch angle the volume of submerged floater changes. Therefore, the volume of displaced water varies. First the volume of displaced water is calculated and then its buoyancy centre is calculated. Depending on these two variables (volume of displaced water and the buoyancy centre), the restoring moment generated by the platform is calculated.

All these forces are combined in a Matlab script. The design variables are the length of the semi axis of the buoyancy chamber. The pitch angle of equilibrium of the platform for each wind speed is calculated. The maximum value of that angle during operation has been set to  $\pm 10^\circ$ . If this requirement is not fulfilled, the variable of design is modified (increased) until the operational limit for the pitch angle is met.

## CYLINDER

It is a steel cylinder of 5 m diameter; 76 m length and 0.04 m wall thickness. It has been proved to be strong enough to support the weight of the wind turbine. Internally the cylinder is hollow, and this contributes to a smaller buoyancy chamber. With the purpose of lowering the gravity centre of the cylinder, ballast was added to the lowest part of the cylinder (close to the joint). The ballast has a conical shape and it is made of concrete.

**Table 4.3-1: Properties of the cylinder of the platform.**

Property	Value (unit)
Length	76 m
Diameter	5 m
Wall thickness	0.04 m
Mass without ballast	401420 kg
Total mass (including ballast)	501020 kg
Volume of water displaced	437.2 <sup>1</sup> m <sup>3</sup>
Rough cost	944560 €

### BUOYANCY CHAMBER

The buoyancy chamber has an ellipsoid-shape (see Figure 4.3-7). Its goal is to increase the buoyancy of the platform in order to be able to create a restoring moment big enough. It should not be too heavy, so the chosen material for this chamber is composite.

Besides, as the buoyancy chamber is located on the upper part of the platform, it receives all the impacts from the waves. Therefore, it needs to be strong enough to resist all the wave loads without cracking. For this purpose, an internal structure or frames similar as the one used in boats has been implemented [DTU06] with material (reference [DTU07]) used in the composite is an E-glass polyester fibre (combined woven roving –WR- and CSM) defined in [DTU08]. The mechanical properties of this material are:

**Table 4.3-2: Properties of the material used (data from [8])**

Property	Value (unit)
Fibre Volume Fraction ( $V_f$ )	0.4
Density	1600 (kg/m <sup>3</sup> )
Tensile Modulus (E)	12 (GPa) <sup>2</sup>
Tensile Strength ( $\sigma_{UT}$ )	180 (MPa)
Compressive Strength	180 (MPa)

The thickness of this material is 5 cm.

The internal structure of the buoyancy chamber has a skeleton made of stainless steel beams. There are two types of beams. All of them have a squared shape. The thickness of those beams is 15 mm. The beams are divided into two sets. One set of beams is located in the periphery of the buoyancy chamber. These beams are under the composite layer and reinforce the resistance against the wave forces. The other set of beams is located close to the steel cylinder and reinforces the inner surface of the buoyancy chamber that is in contact with the steel cylinder. As the sealing of the buoyancy chamber has huge importance, a double layer of the composite material could be required for safety reasons. The link between the different layers of composite and the internal structure/skeleton is made with rivets.

**Table 4.3-3: Properties of the buoyancy chamber of the platform.**

Property	Value (unit)
Length	30 m
Semi-major axis (radius)	15 m
Semi-minor axis (both radii)	5.5 m
Wall thickness	0.04 m
Mass	41363 kg
Volume of water displaced	1272 m <sup>3</sup>
Rough cost	209210 €

<sup>1</sup> The part of the cylinder inside the buoyancy chamber has been already discounted

<sup>2</sup> Measured in the fiber direction

### Conclusions regarding the floating spar with the universal joint

The semi floating spar buoy connected to the soil floor by a universal joint was required to be restrained by 6 mooring lines. The joint restrains rotational motion and the mooring lines restrain both translation and rotation. A composite buoyancy chamber at the mean sea level and concrete ballast at the sea floor are required for stability. The stability of the structure was ensured and the material cost of the structure was found to be less than the material cost for jackets at the same depth.

### Required experimental investigations on innovations on component level

The innovative semi floater arrangement is expected to have a total material cost including the mooring system of about €2 Million. This is significantly less than the material cost of the jacket. However the mechanism of installation of the universal joint at the sea floor and the soil structure interactions thereof needs to be investigated further with experiments.

With respect to jackets, the initial pile configuration provided by RAMBOLL is found to be rather conservative with respect to the pile length. Reduction of the pile length by 10m on each jacket leg is expected to produce minimal impact on overall WT structural response.

The pile length reduction is found to be feasible with certain modifications to the pile configurations such as tip plugs. Particularly the pile tip resistance become a significant part of the vertical reaction force produced by the pulled-out pile and implementation of higher pull-out tip resistance would allow for shorter pile lengths. Experiments that quantify the effect of plugs at the bottom of the piles in terms of pull-out resistance will be beneficial.

### References

- [DTU01] DNV-OS-J101, Design of Offshore Wind Turbine Structures, Det Norske Veritas, January 2013.
- [DTU02] API RP 2A-WSD: Recommended Practice for Planning, Designing and Constructing Fixed Offshore Platforms – Working Stress Design. 21. Edition, 1. December 2000. Including Errata and Supplement 3, October 2007.
- [DTU03] InnWind Design Report - Reference Jacket, Rev. 31/10/2013.
- [DTU04] Christian Bak et al., "Description of the DTU 10 MW Reference Wind Turbine," DTU Vindenergi, DTU, DTU Wind Energy Report-I-0092, 2013.
- [DTU05] Sedillot F. and Stevenson A., "Laminated rubber articulated joint for the deep water gravity tower," *Journal of Energy Resources Technology*, vol. 105, pp. 480-486, December 1983.
- [DTU06] Sumer B. Mutlu and Fredsøe Jørgen, "Hydrodynamics around cylindrical structures," in *Advanced Series on Ocean Engineering*.: World Scientific, vol. 26.
- [DTU07] Eric Greene. (2013) Marine Composites, Webb Institute. [Online]. <http://ericgreeneassociates.com/webbinstitute.html>
- [DTU08] Ronald F. Gibson, "A review of recent research on mechanics of multifunctional composite materials and structures," *Composite Structures*, vol. 92, pp. 2793-2810, 2010.

## 5 LOAD MITIGATION

In the INN WIND.EU reference jacket design report [5-01] an in-depth fatigue analysis of the reference design in combination with the reference turbine was carried out. The results already indicated that the support structure might not fulfil the fatigue requirements for a lifetime of 20 years, especially in the lower parts of the jacket. Innovative solutions are necessary to master these challenges. Two approaches are the usage of innovative materials and/or new design solutions of the support structure as already presented earlier in this report.

Chapter 5 focus, in contrast, on load mitigation strategies. The Fraunhofer Group Darmstadt - LBF therefore discusses the application of passive damping devices. Firstly, a study of the natural frequency and its tuning to the reference is presented. Secondly, the main part of LBF's contribution, is the tuning and evaluation of a vibration absorber at transition piece height. Frequency responses and the effect on tower top displacement are described in the following section 5.1.

ForWind - University of Oldenburg carried out an in-depth analysis of the design load cases and studied the origins of the strongly increased fatigue loads, which are the challenge for the large reference wind turbine support structure. Several possible causes, such as the natural frequency excitation of the tower by the blade passing frequency, are described in detail and possible concepts and their effect are evaluated in section 5.2.

Fraunhofer Group Kassel is focussing on numerous control and regulation concepts to mitigate loads, namely the peak shaving of the thrust and the speed exclusion window to avoid resonances during operation. An outlook is given in section 5.3. on the effect of more advanced strategies such as active tower damping.

### References

- [5-01] INN WIND.EU Design report - Reference Jacket, "InnWind\_DesignReport\_ReferenceJacket\_Rev00.docx", Internal teamsite, uploaded 2014-01-16, accessed 2014-08-12

## 5.1 Passive damping devices (FhG-DA)

Unwanted structural vibrations occur at various operational stages, since loads excite the modes of a system. In particular at lean offshore wind turbines (OWTs) loads can cause large vibration amplitudes. They can lead to fatigue and damage the structure, especially in lightweight designs, which must be used in renewable energy of offshore wind turbines to reduce the overall costs.

Especially the increased loads, the increasing size of design and the larger water depth require innovative development needs. The design of the foundation structure influences significantly the structural dynamic behaviour. The vibrations are analysed with a simulation model. Moreover a tuned vibration absorber (TVA) system can be installed numerically and the amplitudes of the overall structure can be reduced. A vibration absorber can increase the operating range of the system, involving longer power generation. In addition, a TVA helps to increase the lifetime of the OWTs, which reduces the current cost of generating electricity. Furthermore a TVA or a system of TVAs can help to improve the structural behaviour of a lightweight design. Thus, a TVA makes the system more economical and helps to enhance generating power at the ratio of costs.

The effects of vibrations on the structures themselves, however, can be very significant due to structural fatigue. The deflections of the typical mode shapes of vibration should be reduced. This is basically done by energy dissipation with various types of vibration absorbers. Known systems are for example pendulum mass damper or viscous mass damper in different versions [FhG-DA01]. By using of a vibration absorber, the durability of the material of the entire structure can be improved. In terms of offshore wind turbine, the foundation structure may designed material-saving by using a vibration absorber. In addition, it is expected to reduce the prevailing deflections and vibration speed of the nacelle to extend the operating range.

### 5.1.1 Identification and discussion of innovations on component level

In section 5.1 the focus is on passive tuned vibration absorbers to reduce unwanted vibrations. Further the use and development of a simulation model is important. At Fraunhofer LBF ROSAP as well as Bladed are not available. Therefore a model must be developed in the finite element software ANSYS.

The application of a single TVA or a system of TVAs comprises of three important considerations: the agreement on the amount of used TVAs, the positioning of the TVAs and their design and parameterizing. The latter strongly interacts with the positioning, due to available space and junction issues.

In a first step and in particular in this contribution, only one applied TVA is considered.

The optimal positioning of TVAs can be provided with measures of controllability and observability. Therefore system matrices, in particular their eigenfrequencies are needed.

For a single TVA the controllability correlates with the position of the largest amplitude in a specific eigenmode. Influencing the first eigenmode the nacelle would therefore be the best position. However nearby the nacelle as well as inside it, the available space is limited. From this position the torsional mode could also be influenced best, since the deflections are large. The largest deflections of the second eigenmode occur in the middle of the structure. Thus the application at the transition piece is best.

Due to the process of the design of the transition piece and because of the available space, the TVA is applied at the transition piece to influence the torsional eigenmode.

For a second design approach the implementation of a pendular TVA can be considered.

At first the reference structure, which was allocated by Ramboll is modelled in ANSYS and its behaviour is adjusted to the behaviour of the reference model. The structure consists of the jacket, a transition piece, a tower and the nacelle, which is represented by a lumped mass. The structure is made of steel and consists therefore of very low damping. A more detailed description of the reference structure can be found in [FhG-DA02].

The first five eigenfrequencies of the structure are two times the first bending eigenmode, the torsional mode and twice the second eigenmode. The first and second bending eigenmodes appears twice, because of the center of the nacelle is not in the towers center. Further

eigenmodes show an oscillation of the x-braces at the floor nearby the sea. Of course the amplitudes of the operating modes depend on the excitation of the OWT. Also the damping and the interaction with fluid and aerodynamic behaviour must be taken into account. The presented numerical results are obtained using a Dirac impulse with 10kN. The loads are applied at the tower.

The geometry and material data of the reference model of the partner Ramboll are the base for the model in ANSYS. The following Figure 5.1-1 visualizes the comparison of the two models. The reference model created with ROSAP by the project partner Ramboll is shown on the left in Figure 5.1-1 and the model designed in ANSYS is shown on the right. The anchoring of the jacket feet in the seabed is implemented as a fixed mounting in ANSYS.

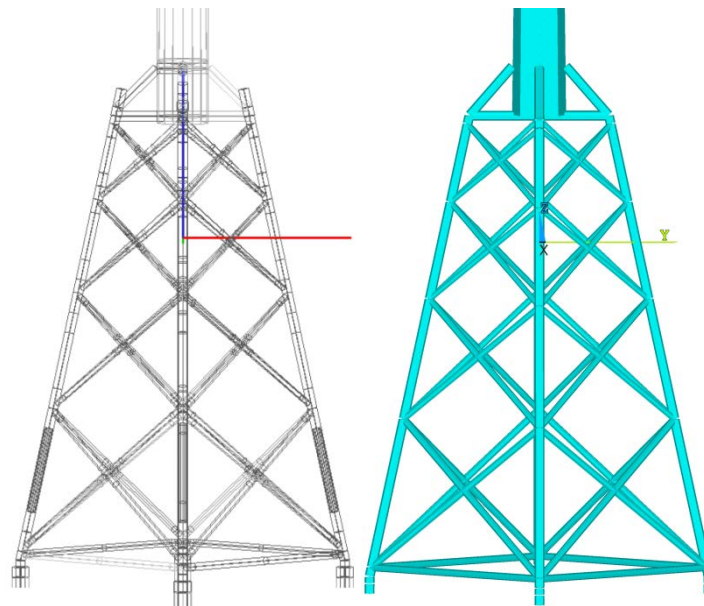


**Figure 5.1-1: left: jacket as ROSAP model; right: jacket as ANSYS model with same location and orientation of the origin**

In a next stage one passive vibration absorber is designed. In the following considerations the vibration absorber is placed at the transition piece. A passive vibration absorber operates through its connecting stiffness and or through its mass, since  $\omega = \sqrt{\frac{c}{m}}$  holds. The mass of the TVA is supposed to be less than 10% of the overall mass.

### 5.1.2 Preliminary studies of innovations on component level

At first a model of the whole system is considered. When the system behaviour of the reference model in ROSAP and the ANSYS model coincide, then the application of a TVA is reliable.

The coordinate system of the model has the same origin and the same orientation than the reference model. The origin of the ordinates is at sea level. The Z-axis points upwards and the X- and Y-axis pass through each of the legs. The model is created parametrically and modularly in ANSYS. Beam elements are used as element type for representing the tubes' characteristics. The lumped mass is assigned with a mass element formulation and three space-dependent moments of inertia are assigned.

The legs are linked with horizontal beams just above the foundation piles. Furthermore, the legs are connected to crossed pipe elements, known as X-braces. These X-braces stiffen the overall structure of the jacket. The connection of the legs with the X-braces is constructed with K-

joints. In reality, all legs, X-braces and horizontal beam elements consist of several welded steel tubes. The respective tube elements have different inner and outer radii and lengths. About a quarter of the jacket protrudes out of the water after installation. At the upper end of the jacket the transition piece joins the tower of the wind turbine with the jacket. The tower is additionally supported at the transition piece with pipes to the jacket.

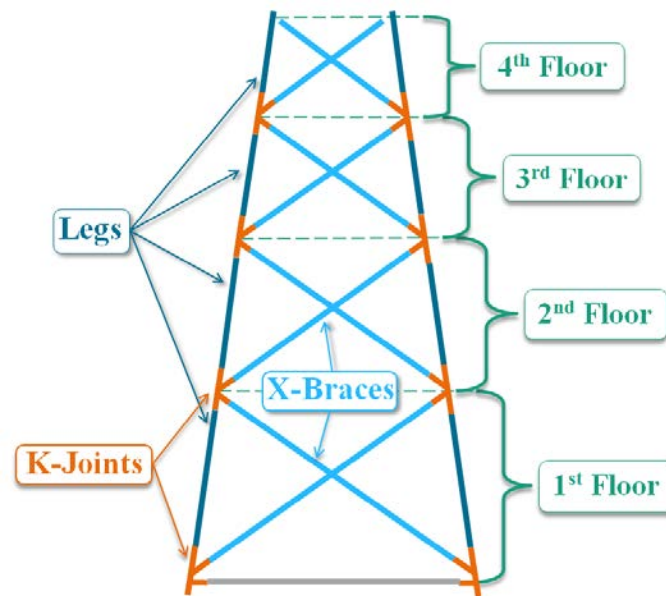


Figure 5.1-2: jacket with naming of the elements and floors

The naming of the elements and floors is shown in Figure 5.1-2. The Jacket is constructed in floors from bottom to top.

The used parameters are the E-modulus, Poisson's ratio, density, material damping, element length, length of the tube section, inner and outer radius.

The tower is also generated equivalent to the legs, where difference between these macros is the constant decreasing inside and outside radii. The tower is also supported by braces with the transition piece. The transition piece and also the nacelle are simulated by a lumped mass and three space-dependent moments of inertia.

### Fitted Model Parameters

The modification of the following parameters is reasoned in the differences between the ANSYS model and the reference model. The aim of the modification is to achieve the same structural dynamic response of the two models. In particular, the eigen frequencies of the system have been modified this way. Mainly modified parameters are the density and modulus of elasticity. There are no geometrical data available of the tubes for the brace support of the tower and the cross on top for the transition piece. The wall thickness of the tubes is designed thicker than the rest of the jacket tubes. This assumption affects positively on model fit.

A possibility to fit the eigen frequencies is to reduce the stiffness. The geometry and material data have influence on the stiffness of the structure. As the geometry is given, the modification has to be done with the E-modulus. Modification of the E-module also takes place mainly at the jacket. The modulus of elasticity of the tower is defined to  $2,04e11\text{kg/ms}^2$ , which is a deviation of 3% to structural steel with an E-modulus of  $2,1e11\text{kg/ms}^2$  [FhG-DA02].

The jacket is assigned in sections to different E-modules, which are between  $0,8e11\text{kg/ms}^2$  and  $1,5e11\text{kg/ms}^2$ . This corresponds to a deviation of 28% to 63% to the reference material. The location dependent modification of the E-Modulus is shown in Figure 5.1-3.

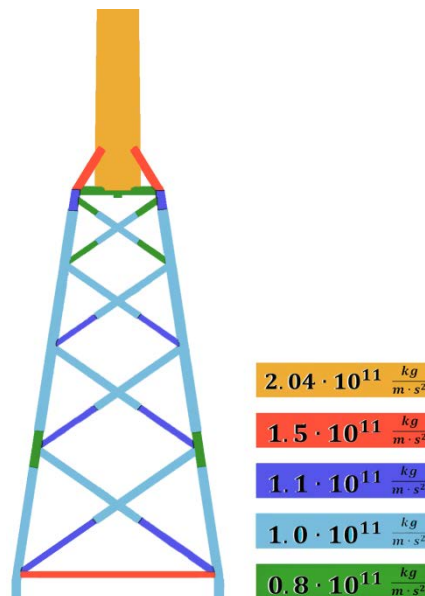


Figure 5.1-3: jacket with location dependent of adjusted E-moduli

The E-modulus of  $1.0e11kg/ms^2$  is assigned to the legs. The exception is the connection between the first and second floor. Here the upper legs of the first floor and the first legs of the second floor have a smaller E-modulus of  $0,8e11kg/ms^2$ . This adaptation has a positive effect on the adjustment of the second bending mode shape, which in turn leads to a smaller deviation on the fourth and fifth eigen frequency compared to the reference model. The upper connection of the legs to the transition piece has a modulus of elasticity of  $1,1e11kg/ms^2$ . The support brace of the tower and the horizontal brace have the biggest E-modulus of  $1,5e11kg/ms^2$ . Only the tower has a higher modulus of elasticity:  $2,04e11kg/ms^2$ . The modulus of  $0,8e11kg/ms^2$  is assigned to the links of the X-brace on the 4th floor and the transition piece. Each first leg of the X-braces of the remaining three levels has a E-modulus of  $1,1e11kg/ms^2$  and the remaining legs one of  $1,0e1kg/ms^2$ .

The model is constructed of structural steel which is the reference material. This steel has a density of  $7850kg/m^3$  [FhG-DA03]. This density is used for the tower. In all other parts of the structure the density is set to  $9500kg/m^3$ . This corresponds to a deviation of 21% to the reference material. With higher density, higher mass is associated which in turn reduces the eigen frequency of the whole structure. The change in density also takes into account the effect of the structure in water. This effect is considered by the increased inertia of the structure in water accounted by its higher density.

For the model, two different types of damping are considered. One takes account of the material damping and the other is a percental damping of the overall structure. The damping of the entire structure is missing. The modified damping used to achieve the required response of the structure is defined as material damping. The material damping ratio  $\xi$  for welded steel parts lies approximately between the value of 0.002 and 0.02 [FhG-DA03]. With this guideline, a default material damping of the model is realized with  $\xi = 0.0025$ , as this is the material damping of structural steel. With knowing that the fact that the structure has a higher damping in water than in the medium of air, the higher damping factor of water is considered within the material damping. About three-quarters of the jacket are in the water. In this section, the material damping is set to  $\xi = 0.5$ . This relates to the two floors at the bottom and half of the 3rd floor.

### Modal Analysis and model comparison

The most important parameters for linear dynamic investigations are given by the eigenvalues and eigenvectors. The first five eigenmodes of the model are shown in Figure 5.1-4 as

a result of the modal analysis with ANSYS. As expected, the first eigenmode is a first bending mode shape of the entire structure. The following eigenmode is also a first bending mode shape of the whole structure but rotated by 90 degrees. After the first bending shapes a torsion of the model follows. The succeeding two eigenmodes are the second bending mode shape, twisted by 90 degrees to each other as with the first bending mode shapes.

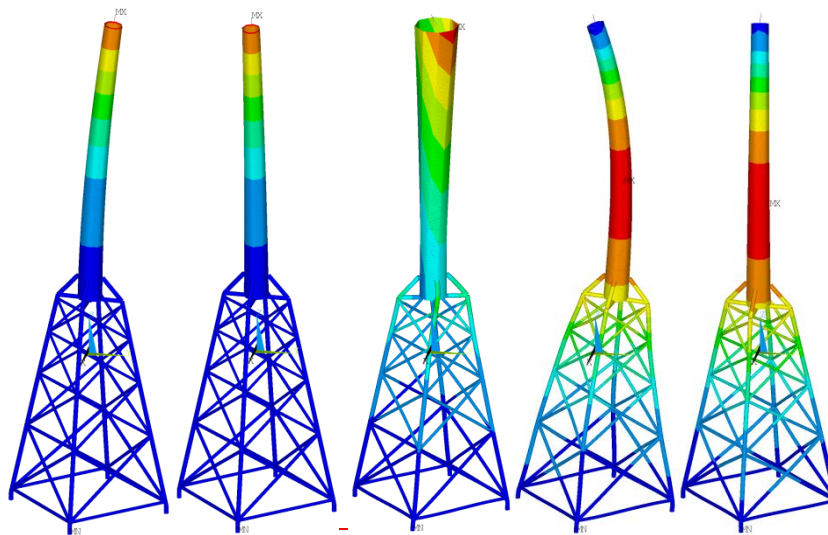


Figure 5.1-4: first five mode shapes of the overall model in ANSYS

Figure 5.1-4 indicates the vibration behaviour of the reference model of Ramboll. The comparison vividly shows that kind and order of the ANSYS model mode shapes are equal to the reference model. The comparison of the mode shapes is operated by comparing the eigenvectors with the Modal Assurance Criterion.

Therefore, the first five eigen frequencies are compared to the created ANSYS model with the reference model of the partner Ramboll.

At first of all it has to be checked if the tower model responses have the same eigen frequencies as the tower of the reference model. As it can be seen in Table 5.1-1 the deviations of the first five eigen frequencies are below five percent. As expected, the first five eigen frequencies of the tower are almost equal to the reference tower model. No modification is necessary besides the modification of the E-modulus with a deviation of 3%.

Table 5.1-1: Comparison of the eigenfrequencies of the tower with the reference model

Mode Number	Mode Shape	Reference Model [Hz]	ANSYS Model [Hz]	Deviation [%]
1	1 <sup>st</sup> bending	0.3246	0.3393	4.53
2	1 <sup>st</sup> bending	0.3274	0.3423	4.54
3	Torsion	1.0298	1.0381	0.81
4	2 <sup>nd</sup> bending	1.7214	1.7007	1.2
5	2 <sup>nd</sup> bending	1.9024	1.8947	0.4

Secondly, the first five eigen frequencies of the overall structure are compared to the reference model. The results of the comparison of the whole structure with the model of the tower amounts only half of the percental deviation.

Table 5.1-2: Comparison of the eigen frequencies of the overall structure with the reference model

Mode Number	Mode Shape	Reference Model [Hz]	ANSYS Model [Hz]	Deviation [%]
1	1 <sup>st</sup> bending	0.2867	0.2846	0.73
2	1 <sup>st</sup> bending	0.2885	0.2864	0.71
3	Torsion	0.9358	0.9797	1.78
4	2 <sup>nd</sup> bending	1.1003	1.1175	1.56
5	2 <sup>nd</sup> bending	1.1133	1.1388	2.29

### Model Comparison with Modal Assurance Criterion

The two models are compared with the Modal Assurance Criterion (MAC) [FhG-DA04]. The eigenvectors of both models are compared by observing the geometry data. The comparisons of the models are plotted in Figure 5.1-5.

The first two eigenmodes of the ANSYS model correspond with the reference model. The torsional mode as a third mode also correlates with the reference model, even if the results of the comparison are not as clear as in the first two modes. The fourth and fifth eigenmodes are correlating as well. For the sixth and seventh eigenmode a correlation is noted but it does not have the same quality as the previous ones.

The fact that the eigenvalues of the first ANSYS mode show similarity to the sixth reference mode (respectively two to seven) can be explained by a similarly occurring bending shape. The eigenmodes eight, nine and ten excite only the lower parts of the structure, not the tower. These are only local mode shapes of the single braces. Only these global modes are essential to the overall dynamic response. Due to missing information about the eigenmode shapes six to ten of the reference model no statement concerning the comparison of the models can be made.

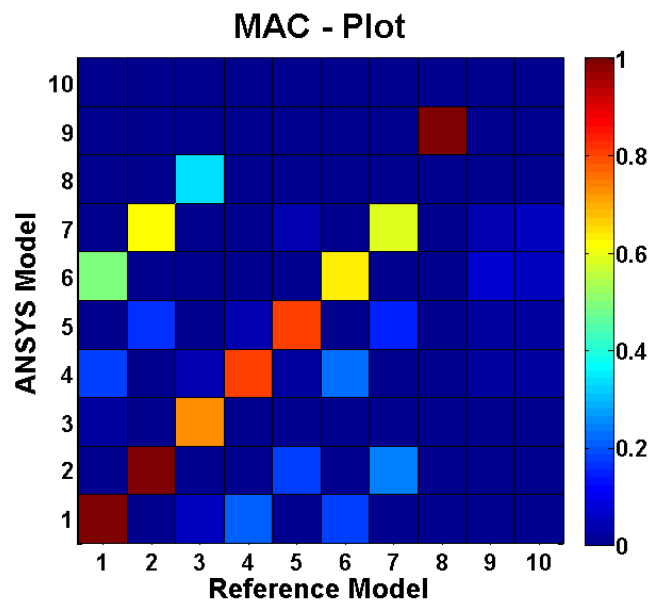


Figure 5.1-5: MAC-Plot compares ANSYS and reference model

However, the result of comparing the first five eigenmodes is optimal. These two modes are essentially characteristic for the system.

### Design of the Vibration Absorber

Now the basic geometrical and constructive data concerning the set-up of the vibration absorber is described. The vibration absorber is constructed economically. The vibration absorber is designed as a torus. In Figure 5.1-6 two different concepts are illustrated.

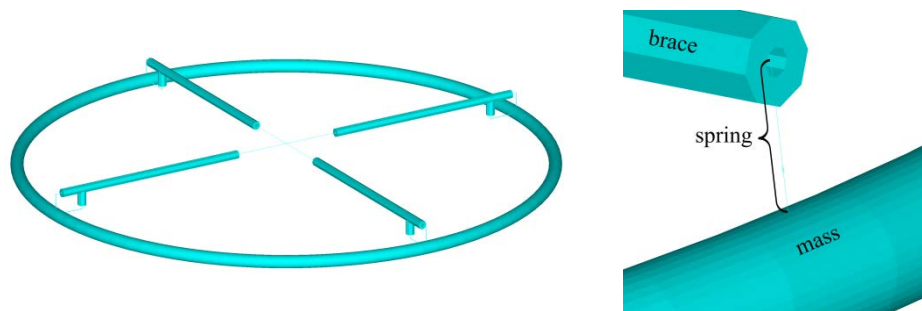


Figure 5.1-6: concepts of the vibration absorbers designed in ANSYS

The value of the torsional eigen frequency of the overall structure amounts  $f = 0,28462\text{Hz}$ . At this value the highest grade of displacement is reached. Due to this fact the vibration absorber is tuned in order to reduce these displacements.

As above mentioned the vibration absorber provides the necessary eigen frequencies and is able to withstand the strains: The braces are dimensioned with high total and wall thicknesses, respectively. The for the absorber effect necessary and relevant stiffness is gained by means of the spring-elements. For more detailed information see Figure 5.1-6.

The design of the vibration absorber does not have an additional damping element. The damping is provided by the material and structural damping. The ratio of the absorber mass to the mass of the total structure equals 7.6%. For more relevant data of the vibration absorber see Table 5.1-3.

Table 5.1-3: Vibration absorber data

Parameter and Data	Value	Entity
Spring Stiffness	318 400	N/m
Absirber Nass	357 011	kg
First eigenfrequency	0,28	m
Radius of the Torus	15	m
Outer Radius of the Torus-beam	0,44	m
Inner Radius of the Torus-beam	0,2	m
Outer Radius of the braces	0,3	m
Inner Radius of the braces	0,1	m
Length of the Spring	1	m
Total mass	565 660	kg

### Model with Vibration Absorber

The braces of the vibration absorber are connected to the tower at a height of 25 m above sea level.

The braces of the vibration absorber are rotated by 45 degrees to the legs of the jacket and the brace support of the tower. This constructive design makes the vibration absorber less stiff in the direction of the tower's first eigenmode. This allows the vibration absorber more easily to transmit the energy to the remaining structure.

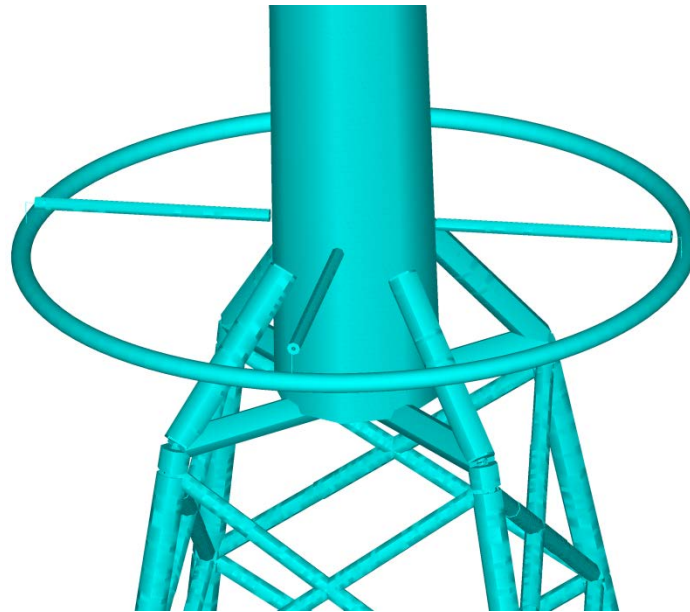


Figure 5.1-7: model with connected vibration absorber in ANSYS

### 5.1.3 Interim conclusion and assumed impact of innovations on component level

#### Modal Analysis of the Model with Vibration Absorber

A modal analysis is also done for the model with the connected vibration absorber. The first three mode shapes of the model, see Figure 5.1-8, are rigid body modes. This results from the coupling and the degrees of freedom of the vibration absorber with the Model.

With the connected vibration absorber one translation mode occurs, which excites only the vibration absorber itself and not the rest of the model. The torsion is displaced after the two second bending modes, see Figure 5.1-8.

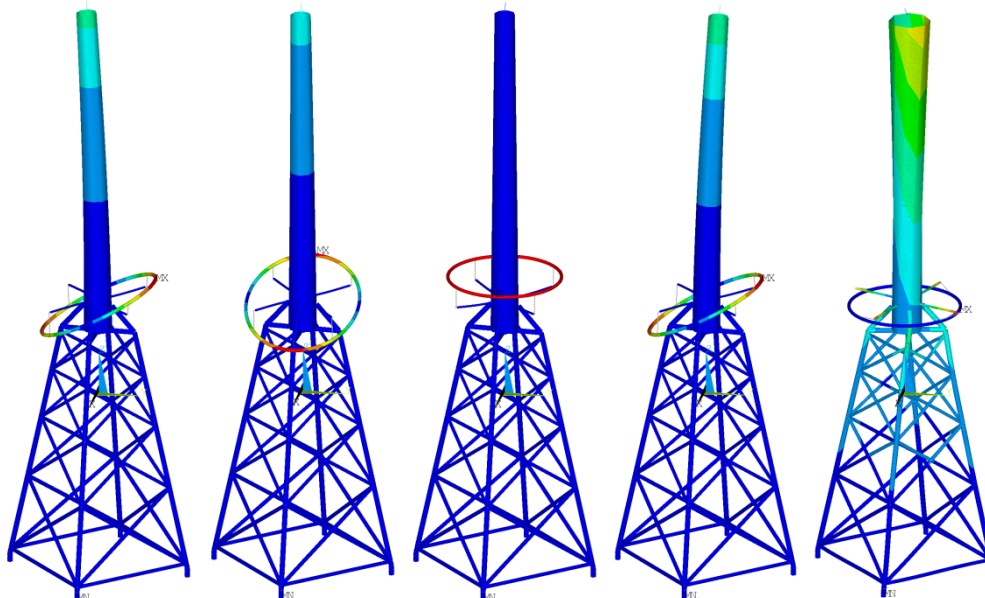


Figure 5.1-8: mode shapes from 1st to 3rd eigen frequency of the model with vibration absorber

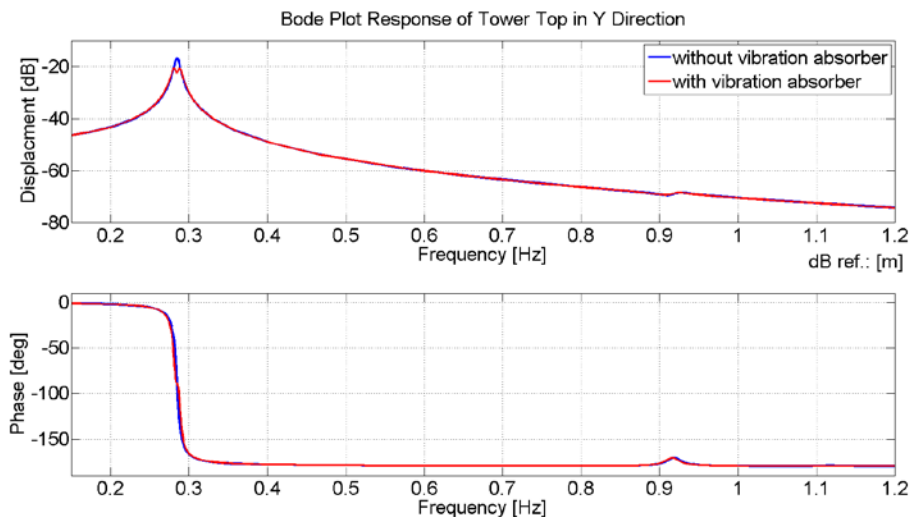
### Harmonic Response Analysis of the Model with Vibration Absorber

The harmonic response analysis is a type of analysis in which the applied loads harmoniously vary over time with known amplitude and frequency. The steady-state response of the structure is calculated as a function of frequency for these loads. The harmonic response analysis is conducted for the model with vibration absorber using modal superposition. The modal superposition sums up the eigenvectors from the modal analysis in order to calculate the response of the structure.

In the harmonic response analysis a structural damping is defined for the entire model. The chosen damping value is based on the damping ratio  $\xi_i = 0.012$  for welded steel structures. The analysis is accomplished in the frequency range of the first five eigen frequencies of the model of 0.15 Hz to 1,3 Hz. At the top of the tower a stimulating force of 10 kN is assumed which exerted in the Y-direction. The system response is evaluated as displacements about the frequency axis. The displacements are plotted from the bottom and top of the tower in X- and Y-direction.

The two Bode Plots in Figure 5.1-9 show the decreasing of displacement on the top of the tower, which is effected because of the vibration absorber. Figure 5.1-9 shows the response in Y-direction, which is stated to be the direction of the stimulating force and Figure 5.1-9 shows the response in X-direction. In both directions the reduction of the resonance of the first eigen frequency is significant.

The resonance occurring additionally due to the vibration absorber is clearly visible in all Bode Plots at 0.2878 Hz. In both Figure 5.1-9 and Figure 5.1-10 the other resonances of the torsional mode at 0.9358 Hz and the second bending mode at 1.1003 Hz can be seen at tower top and tower bottom in X-direction. Even if the response of the amplitude of the torsion is higher with the vibration absorber than without vibration absorber, the displacement of the second bending mode is lower again. However, these resonances have small responses which can only be seen if they are plotted logarithmically.



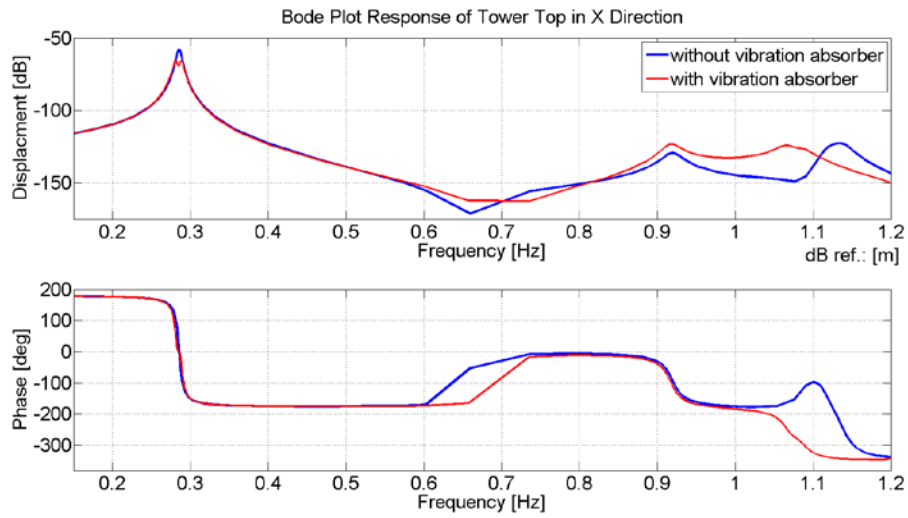
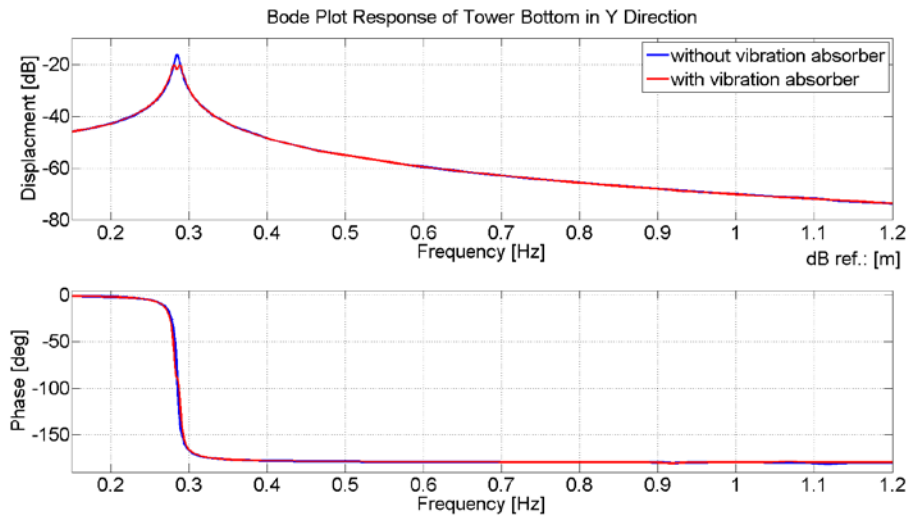


Figure 5.1-9: Top x and y



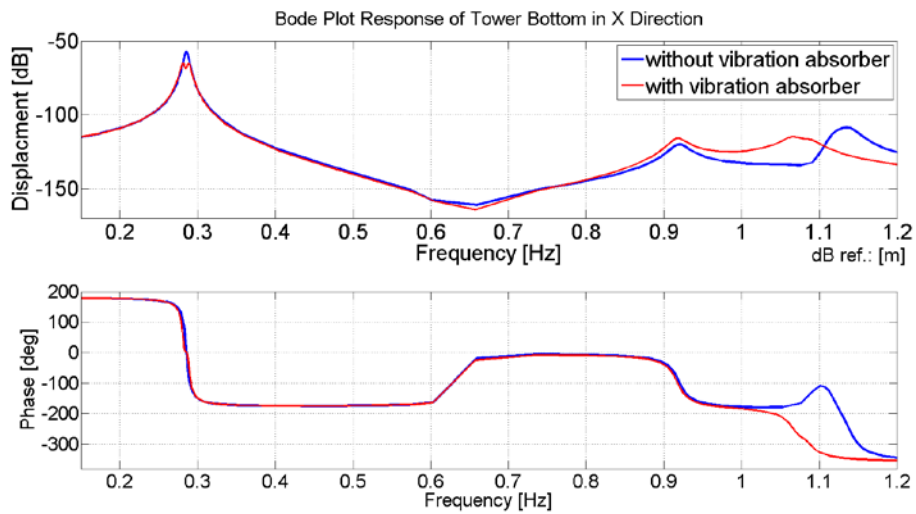


Figure 5.1-10: Displacement Response with and without Vibration Absorber at Tower Bottom

In Figure 5.1-11 the reduction of the response between the models with and without vibration absorber on the top of the tower in Y-direction is shown. For the stimulating force of 10 kN the amplitude of the model without vibration absorber has a value of -16.9 db and the amplitude of the model with vibration absorber one of -20.74 db. This corresponds to a displacement's deviation of 35.8%.

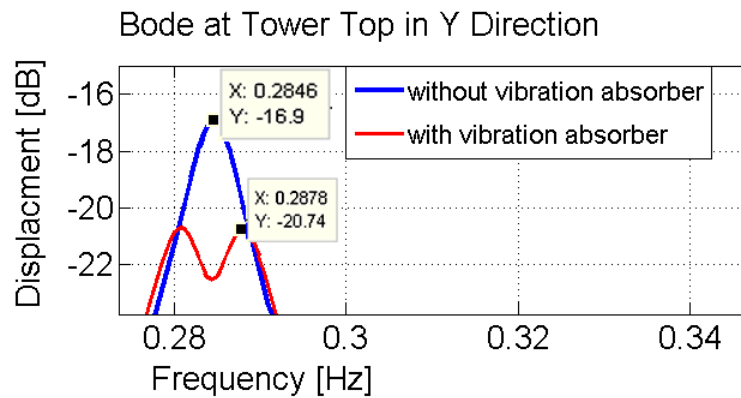


Figure 5.1-11: deviation of the response with and without vibration absorber on tower top in y-direction

The displacement's deviation of 35.8% is also seen in Figure 5.1-12. Because of the stimulating force the top of the tower is displaced without vibration absorber to 0.1428 m. In contrast, the top of the tower is displaced only by 0.0918 m if constructed with the vibration absorber.

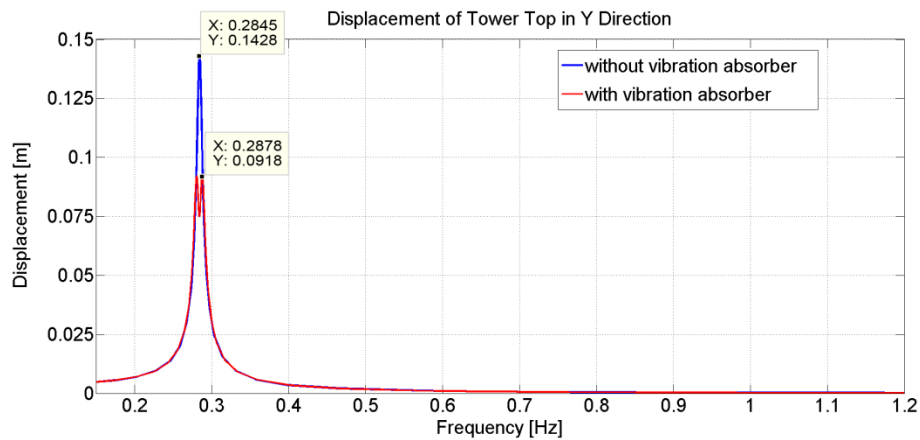


Figure 5.1-12: deviation of the displacement with and without vibration absorber on tower top in y-direction

#### 5.1.4 Required experimental investigations on innovations on component level

Working with ANSYS enabled to analyse the structural dynamic response of an offshore wind turbine's structure by means of the modal analysis and a harmonic response analyse. Frequencies and eigenvalues were calculated. These are characteristic for the structural dynamic behaviour of the model. The eigenvalues are matched with the Modal Assurance Criterion. To reduce the deviation of the eigen frequencies significantly the E-modulus and the density are adapted. Furthermore, the material damping of the jacket sections under water is increased in order to simulate the dynamic behaviour in a better way and to reach the equal dynamic behaviour as in the reference model.

Eventually, the vibration absorber with separated spring-elements is adjusted to the model. This vibration absorber with separated spring-elements causes a reduction of the overall structure's amplitude of displacement even with a small mass ratio of only 7.6%.

Finally, it is confirmed by means of the harmonic response analyse that the vibration absorber reduces the amplitude of the displacement of the tower top by 35.8% in Y-direction, which is stated to be the direction of excitation.

However, to get a result an impact of 10 kN is exerted on the top of the tower. Generally acceptable conclusions about the reduction of the displacement in any other loading case cannot be drawn. Further research concerning the quantities and directions of loads will be essential in order to find out how the overall structure reacted on all kinds of loads. Additional investigation in order to improve the system response could be made regarding the mounting location of the vibration absorber.

#### References:

- [FhG-DA01] Deliverable D4.1.1, "Innovations on component level for bottom-based structures", 2013.
- [FhG-DA02] INN WIND.EU Design report – Reference Jacket, "InnWind\_DesignReport\_ReferenceJacket\_Rev00.docx", Internal teamsite, uploaded 2014-01-16, accessed 2014-08-28
- [FhG-DA03] Müller, G.; Groth, C., "FEM für Praktiker – Band1: Grundlagen", ISBN: 978-3-8169-2685-6, expert verlag, 1993, Renningen.
- [FhG-DA04] Ewins, D. J.: "Modal testing: Theory and practice", ISBN: 0-86380-218-4, Research Studies Press, 2000, Baldock and England

## 5.2 Semi-active and active damping devices (UOL)

### 5.2.1 Identification and discussion of innovations on component level

For the identification of necessary innovations on component level, initially an in-depth analysis of the reference support structure, the design integration of rotor-nacelle-assembly and the effect of the reference controller in different operational points is carried out. Therefore, the reference support structure, designed by Rambøll, had to be imported into the aero-elastic simulation tool GH Bladed.

#### Implementation of the reference structure in GH Bladed

The following graphs illustrate the design of the reference structure in GH Bladed. Whereas the first gives an overview over the nomenclature for the nodes, the second shows the numbering of the elements. The support structure in GH Bladed consists of 264 nodes and 323 elements. In the following sections, three main representative sections are analysed: The transition piece node (1), a lower tower leg node (2) and a lower brace node (3) as shown in Figure 5.2-1. Wind and waves are in all investigations approaching from north, or with respect to Figure 5.2-1, Figure 5.2-2 and Figure 5.2-3 from the left hand side.

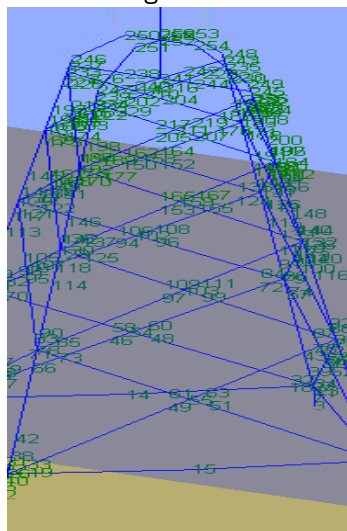


Figure 5.2-1: Jacket structure and nodes in GH Bladed

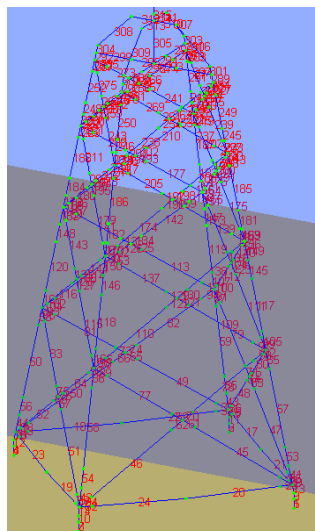


Figure 5.2-2: Jacket structure and elements in GH Bladed

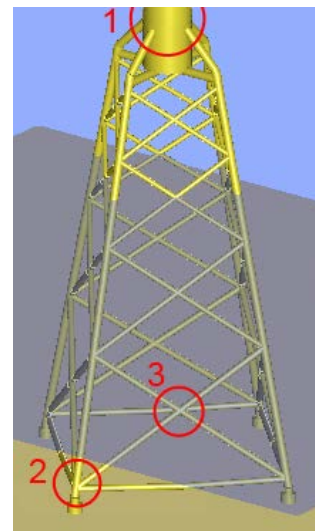


Figure 5.2-3: Jacket structure and investigated sections

#### Tower and Rotor-Nacelle-Assembly

The Rotor-Nacelle-Assembly is imported in the GH Bladed model as provided by DTU and Uni Stuttgart on the internal webpage [OLD01]. The following differences in terms of mass and inertia were found in comparison with the RNA used by Rambøll for the reference design of the support structure [OLD02]. The specific influence on the dynamic behaviour of this difference is not further investigated. The modal validation of the reference structure is found in the section “Analysis of dynamic behaviour and comparison with other codes”.

Table 5.2-1: Rotor-Nacelle-Assembly Data, ref. [OLD02]

RNA at tower top		
	ROSAP	GH Bladed
Lumped Mass [kg]	676723	676543
Moment of Inertia about x-axis [kg m <sup>2</sup> ]	1.66e8	1.563e8

## Analysis of dynamic behaviour and comparison with other codes

### General

The purpose of this section is to compare the system dynamics of the reference support structure design investigated with ROSAP against the results derived with GH Bladed. Furthermore, it compares the coupled natural frequencies of GH Bladed with those deduced in HAWC2 by DTU. The purpose is however not to do an in-depth comparison like in OC4, which is out of scope of the INN WIND.EU project [OLD03].

Nonetheless, the dynamic analysis is important to ensure a realistic representation of the dynamic behaviour of the turbine in operation. Therefore these basic comparisons are indispensable. The adequate dynamic modelling ensures a realistic reproduction of the systems reaction to external excitations. The rotor stimulates the tower and support structure with 1P, which means corresponding to the rotor frequency, 3P, corresponding to the blade passing frequency, and its multiples. The 1P bandwidth is for this turbine configuration between 0.1 and 0.16 Hz, the 3P bandwidth between 0.3 and 0.48 Hz. Therefore, including a safety margin of 10%, and assuming a soft-stiff configuration, the frequency allowance would be between 0.176 to 0.272 Hz.

### Calculation method

The calculation of the angular periods, as described in the INN WIND.EU Design Report [OLD02], of the support structure – tower configuration is based on the solution of the eigenvalue problem. Given the global stiffness matrix [K] and the global mass matrix [M], the natural frequencies and modes shapes can be calculated according to:

$$([K] - \omega^2 [M]) \{v\} = \{0\}$$

where omega represents the eigenvalues which determine the natural frequencies of the system and the eigenvectors {v} determining the shapes of the vibrational modes.

### Results

#### Tower only

The first 5 natural frequencies of the tower (including the RNA), considering the tower to be clamped at interface (tower bottom, transition piece), are displayed in Table 5.2-2.

**Table 5.2-2: First 5 natural frequencies of the tower considered clamped at tower interface**

	Mode	1 <sup>st</sup> Bending side-side	1 <sup>st</sup> Bending fore-aft	Torsion	2 <sup>nd</sup> Bending side-side	2 <sup>nd</sup> Bending fore-aft
Natural Frequency [Hz]	ROSAP	0.3246	0.3274	1.0298	1.7214	1.9024
	GH Bladed	0.328	0.331	1.171	1.699	2.046
	Difference	1%	1.1%	12%	-1.3%	0.7%

It can clearly be seen that the accordance of the natural frequencies is, except for the torsional frequency, in an acceptable range for the further implementation of the overall system including the support structure.

#### Total structure (uncoupled modes)

As shown in Table 5.2-3, the first natural frequency of the overall uncoupled system lies marginally under the 3P region, which is at 6 rpm for the first reference control, and the design can therefore be considered as being critical. This aspect has to be managed with ease in the design phase of the wind turbine control, otherwise the operation of the wind turbine in the lower rotational speed region will highly amplify turbine loading and consequently reduce fatigue life of

the structure which will be shown in section “Aero-elastic simulation of the reference structure in GH Bladed”.

The next step is to evaluate the natural frequencies of the overall structure, to assess the criticality during operation in simulations. These frequencies, without coupling with blade modes, are presented in the following.

**Table 5.2-3: First 5 natural frequencies of the total structure**

	Mode	1 <sup>st</sup> Bending side-side	1 <sup>st</sup> Bending fore-aft	Torsion	2 <sup>nd</sup> Bending side-side	2 <sup>nd</sup> Bending fore-aft
Natural Frequency [Hz]	ROSAP	0.287	0.289	0.936	1.100	1.113
	GH Bladed	0.297	0.299	1.102	1.565	1.858
	Difference	3.5%	3.5%	15.1%	30%	40.1%

As can be clearly seen, the first two natural frequencies are matching quite well in the comparison of the outputs of the two codes. However, the torsional frequency is again overestimated by GH Bladed as in the aforementioned analysis of the pure tower.

A reason for the large deviation of the second tower modes could not be found so far. Possible reasons might be that a different modelling of the soil as a stiff soil in comparison to an elastically modelled one has a minor influence on the first natural frequency whereas its effect on the second might be significantly higher. Another obstacle could be the different modelling approach in GH Bladed compared to ROSAP. ROSAP uses a finite element method, whereas the elements in GH Bladed are coupled with a multi-body approach. Further information about in-depth code comparisons and the difference between different tools can be found in the OC4 project report [OLD03].

Most likely, also the modelling of the nodes and braces has a significant contribution to the result as ROSAP defines joint flexibilities and therefore softens the tower. A rigid representation of the braces and joints would lead to an overestimation of the natural frequency.

The first two uncoupled bending modes in both directions, fore-aft and sideways, as well as the uncoupled torsional mode are shown in the Figure 5.2-4 to Figure 5.2-8.

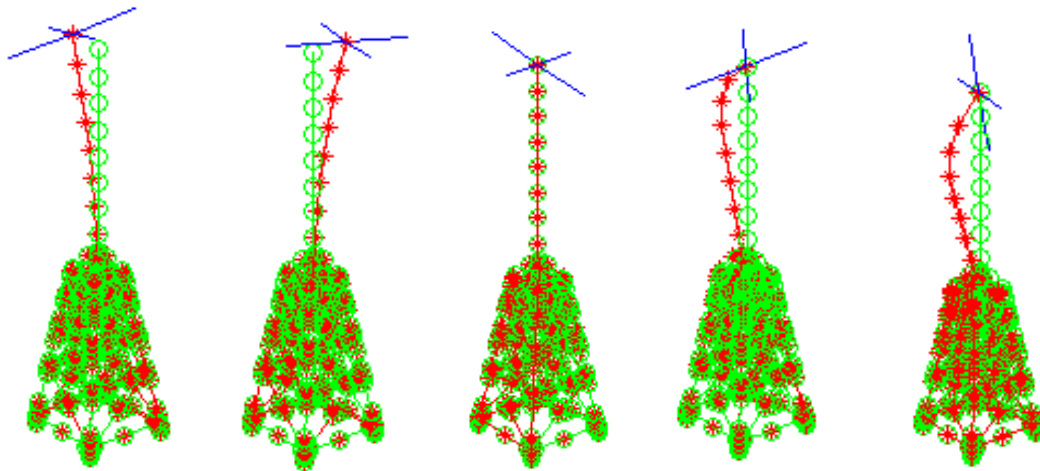


Figure 5.2-4: First natural tower mode fore-aft

Figure 5.2-5: First natural tower mode sideways

Figure 5.2-6: First torsional tower mode

Figure 5.2-7: Second tower mode fore-aft

Figure 5.2-8: Second tower mode sideways

### Total structure (coupled modes)

More important, for the overall system dynamics in aero-elastic simulations than the uncoupled modes with lumped tower top mass, are the coupled modes taking the system dynamics of the rotor-nacelle assembly, especially the blade dynamics, into account. In the following Table 5.2-4, a comparison of coupled modes derived with HAWC2 and GH Bladed is shown. It is clearly seen that the coupled frequencies of both software tools are in relatively good accordance to each other.

Table 5.2-4: Natural frequency comparison of coupled modes in HAWC2 and GH Bladed

	Mode	Tower mode 1	Tower mode 2	Blade 3 mode 1	Blade 2 mode 1	Blade 1 mode 1	Blade 2 mode 2	Blade 1 mode 2	Tower mode 3
Natural Frequency [Hz]	HAWC2	0.3	0.31	0.55	0.59	0.63	0.92	0.94	1.41
	GH Bladed	0.3	0.31	0.60	0.64	0.66	0.94	0.95	1.43
	Difference	0%	0%	8.3%	7.8%	4.5%	2.1%	1.1%	1.4%

The corresponding modes are depicted and described further in the following. The first two coupled modes are dominated by the first two uncoupled tower modes: the side-to-side and fore-aft mode of the tower. It can be seen that, especially in the second coupled mode, a flapwise motion of the rotor blades has a significant share in the overall system motion.

The third and fourth coupled modes are dominated by the uncoupled blade modes in flapwise and edgewise direction respectively. The coupled modes represent the asymmetric flap- and edgewise blade mode. Only minor contribution of tower sideways and fore-aft motion is seen in these modes. The fifth mode is the coupled tower torsion and blade flapwise motion mode.



Figure 5.2-9: Tower mode 1 – side to side

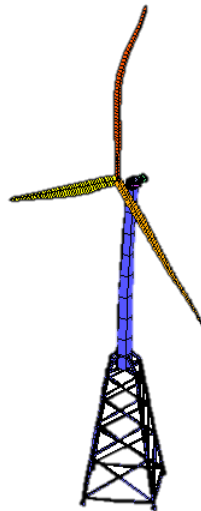


Figure 5.2-10: Tower mode 2 – fore-aft

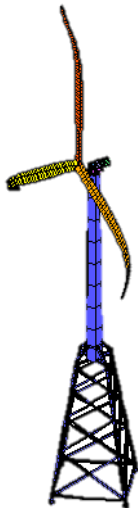


Figure 5.2-11: Blade mode 1 – asymmetric flapwise

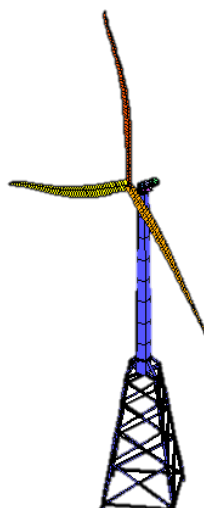


Figure 5.2-12: Blade mode 2 – asymmetric edgewise

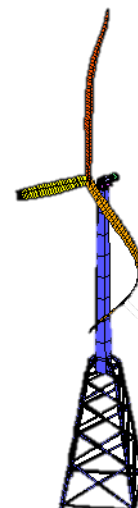


Figure 5.2-13: Tower mode 3 – Torsion

### Reference control for the reference turbine

In a first approach, the reference control, which was released in October 2013, was used in simulations. The following graphs show the principle controller behaviour with respect to power, rotor speed, torque, and pitch angle. A more detailed description of the controller can be found in [OLD04].

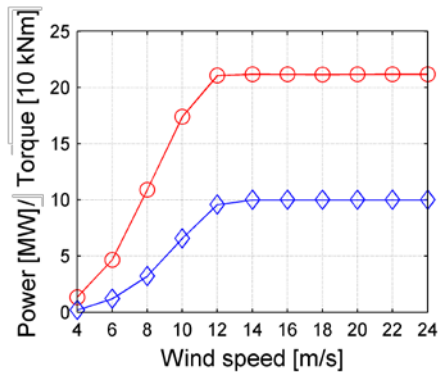


Figure 5.2-14: Power (blue diamonds) and Torque (red circles) over wind speed

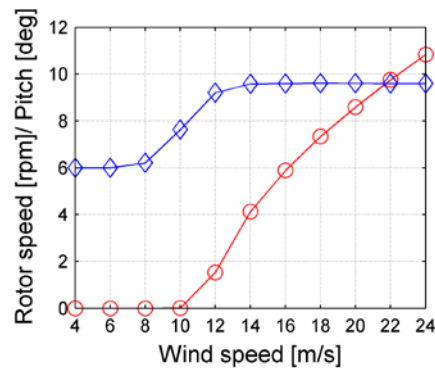


Figure 5.2-15: Rotor speed (blue diamonds) and pitch angle (red circles) over wind speed

As can be seen in Figure 5.2-14 and is further elaborated in the following Campbell diagram, the blade passing frequency ( $3\Omega$ ) in the lower wind speed region targeted by the initial controller coincides with the first lateral and longitudinal natural frequencies of the tower. Severe resonances can be expected, leading to highly increased fatigue loads for the wind speeds of 4 to 8 m/s. The effect in aero-elastic simulations is evaluated in the following.

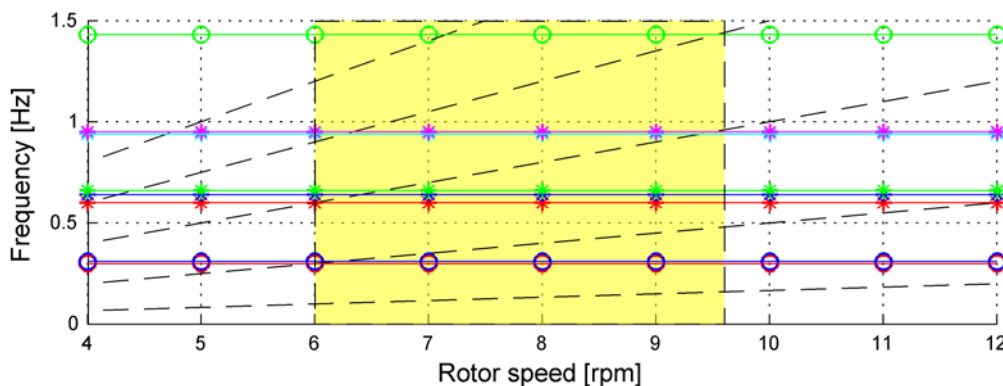


Figure 5.2-16: Campbell diagram for the INN WIND.EU reference turbine and support structure including coupled tower (circles) and blade (star) modes - operational region indicated by the yellow box

### Aero-elastic simulations of the reference structure in GH Bladed

The aero-elastic simulations are carried out in GH Bladed, which offers the possibility to combine aerodynamic modelling based on the BEM algorithm with multi-body structural dynamics. It is a widely used tool for simulation of wind turbines especially for certification purposes and validated with numerous measurement data.

The simulations are, if not defined otherwise, carried out with turbulent Kaimal wind fields with wind speed steps of 2 m/s and 6 turbulence seeds per wind bin. Only load cases according to IEC 61400-3 [OLD05], “Normal power production with turbulent wind”, are considered in the following.

The evaluation of the wind turbine loading is done under use of the rainflow counting method, leading to damage equivalent loads and moments which are representative for the fatigue damage of the given component. In all simulations, if not specified otherwise, the reference number of cycles is  $1E07$  and the time series from the aero-elastic simulation is extended to 20 years lifetime to compare single wind speed bins. The results are not weighted, according to the occurrence per wind speed bin per year, with the Rayleigh distribution.

The first comparison is done for equivalent loads at the transition piece for wind speeds from cut-in, 4 m/s, up to cut-out wind speed, 24 m/s. The controller used for the simulations is the old reference controller which was released in October 2013 and is further described in [OLD04]. In Figure 5.2-17 the tower base moments in fore-aft direction at the transition piece are shown, whereas Figure 5.2-18 illustrates the DEL at the same position in sideways direction.

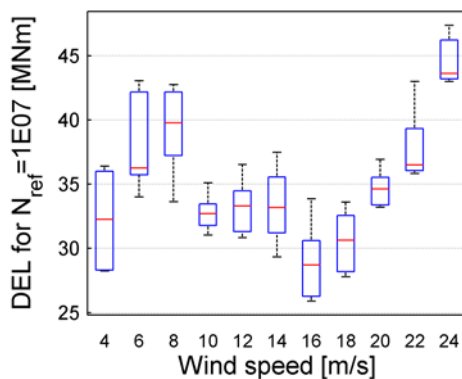


Figure 5.2-17: Damage equivalent load at transition piece in fore-aft direction

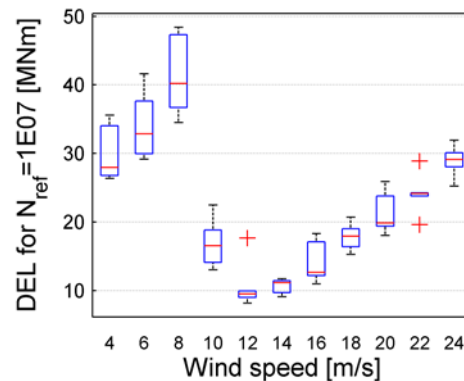


Figure 5.2-18: Damage equivalent load at transition piece in sideways direction

As can be seen for both fore-aft and sideways direction, the loads in the partial load range up to 8 m/s are highly increased compared to the usual load envelope of a wind turbine. Especially for the side-to-side direction, the loading is highly enhanced in comparison to the other wind speeds, which can be reasoned by the missing aerodynamic damping in this direction.

The issue of highly promoted loads in the lower wind speed and therefore rotational speed region can be reasoned by resonances of the blade passing frequency with the tower and support structure natural frequency. As can be seen in Figure 5.2-16 in the Campbell diagram, this was already expected and could be proved in aero-elastic simulations to be a crucial challenge for the fatigue loading of the tower and support structure. A newer release of the reference control tackles this issue by decreasing the minimal rotor speed from 6 rpm to 5 rpm and excluding the rotational speed with a window around 6 rpm. The results are shown and compared in the section “comparison of old and new reference control”.

### Influence of natural frequency on fatigue loading

The increased loading in the partial load range proved that resonances are an important factor when analysing an integrated wind turbine design with tower and support structure. Therefore, many requirements are to be considered when designing the support structure. One important parameter is the natural frequency which has to match a certain frequency bandwidth which can be shown with the Campbell diagram in Figure 5.2-16. A poorly designed support structure leads to a significant change in dynamic behaviour of the overall system and, consequently, to massively promoted loads. In the following, a parameter study with the natural frequency is presented. Therefore the material parameters of the support structure variations were used to receive tuned natural frequencies. Simulations were carried out for 6 m/s wind speed and 6 seeds. The rotor speed is 6 rpm, which means that the 1P excitation is at 0.1 Hz and the 3P excitation at 0.3 Hz. The 3P, therefore, coincides with the corresponding first natural frequency at 0.3 Hz and leads to resonances. As it can be seen the fatigue loads in this region are highly increased.

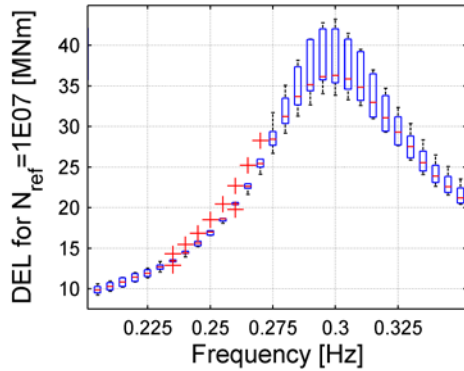


Figure 5.2-19: DEL over frequency for 6 m/s wind speed at tower base in fore-aft direction

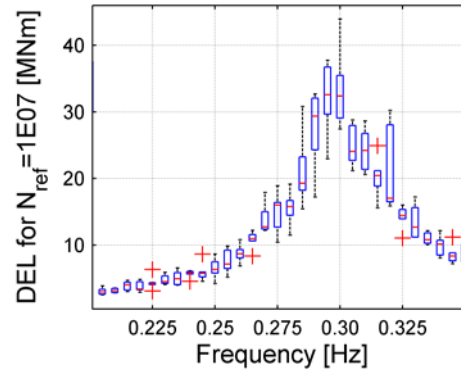


Figure 5.2-20: DEL over frequency for 6 m/s wind speed at tower base in sideways direction

Several aspects can be seen while analysing the data. First of all, the closer the excitation (or its multiples) to natural frequency, the higher the damage equivalent loads. Increases of around 350% are found. Furthermore, the closer the excitation (or its multiples) to the natural frequency, the larger is also the spread of loading among different wind speed seeds. In addition, it seems that lower natural frequencies (soft configuration) lead to significantly lower fatigue loads than an increase of the natural frequency towards a soft-stiff configuration. In other words, the peak of fatigue load seems to be asymmetric with respect to the excitation frequency.

For the sideways fatigue loads one can conclude that the peak is as expected also present as the sideways natural frequency is the same as in fore-aft direction. However it can clearly be seen that the principal fatigue level is generally lower for natural frequencies apart from the rotor speed. In a case of a natural frequency close to the excitation frequency this loads are, however, also increased by 1000%. It can further be seen that the width of the peak is remarkably smaller than the one of the fore-aft tower base moment. The reason for the larger increase in amplitude and smaller width can be found in the lack of aerodynamic damping and therefore lower overall damping in sideways direction. This study shows clearly the need for additional, omni-directional damping to overcome resonance caused fatigue issues like presently facing in this project with the reference turbine and support structure.

### Share of wind and wave loading of the overall fatigue damage

Another reason for excitation of the support structure is the stochastic wave loading. Therefore the question for the following investigation was to estimate the share of wind to wave loading for the support structure. A study was carried out to have a closer look at the distribution.

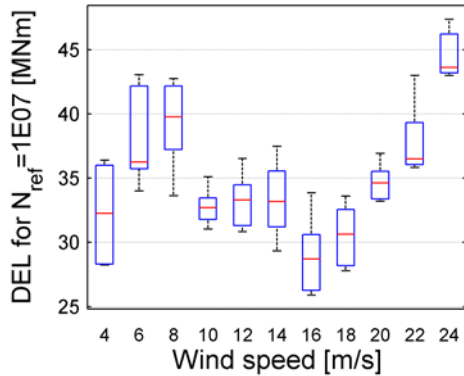


Figure 5.2-21: Damage equivalent loads at transition piece in fore-aft direction with pure wind excitation

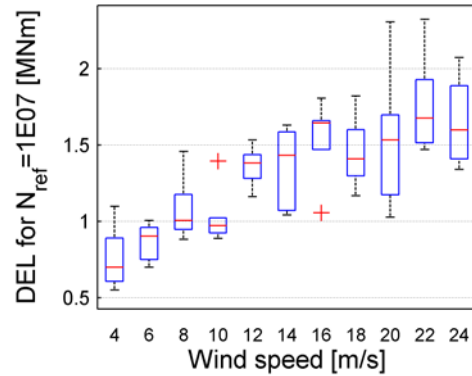


Figure 5.2-22: Damage equivalent loads at transition piece in fore-aft direction with pure wave excitation

Figure 5.2-21 and Figure 5.2-22 compare the bending moments in fore-aft direction (wind and waves aligned an approaching from  $0^\circ$ ). As can clearly be seen, the loading is smaller by one order of magnitude. What can be noticed in addition is that the effect of increasing wind speed on the wave height (see design basis [OLD06]) leads to an analogous increase of loads with increasing wind speed due to wave excitation. The moment due to wind loads is, however, strongly connected to the operational status of the turbine and, therefore, related to the wind turbine control.

As the DELs due to wave loading are an order of magnitude lower than due to wind excitation, the share of wave loads by geometric combination of the loads as described by Kuehn [OLD07] is negligibly low at the transition piece.

Over the whole wind speed range, the share of wave loading for the fatigue loads is less than 1.5% in both fore-aft and sideways direction, as can be seen in Figure 5.2-23.

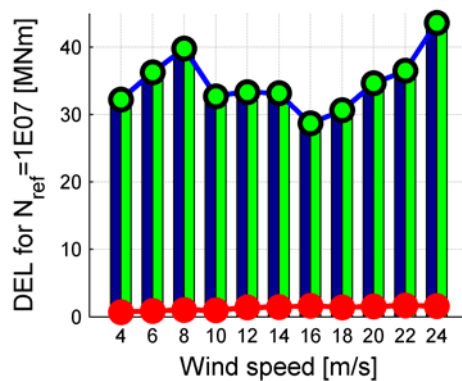


Figure 5.2-23: Wind (blue) and Wave (red) loads as well as integrated simulation results (green) at the transition piece in fore-aft direction

The wind and wave share was also analysed at two further sections, namely the lower leg and a lower brace, see Figure 5.2-3. The Figure 5.2-23 and Figure 5.2-24 show the results.

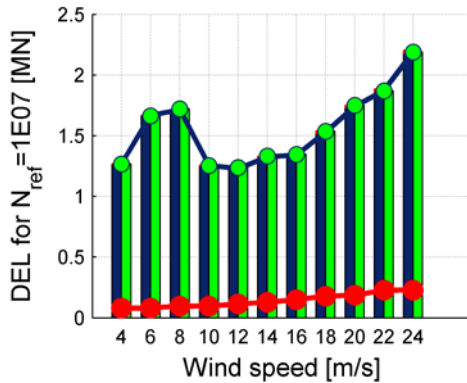


Figure 5.2-24: Fatigue load in axial direction at lower leg

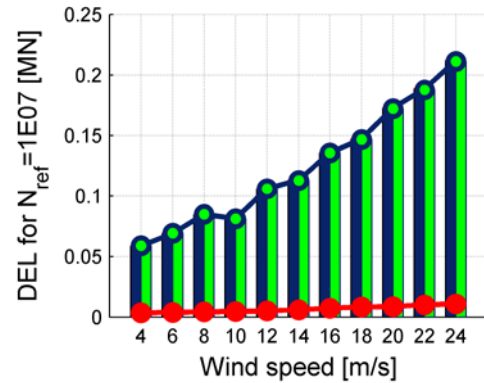


Figure 5.2-25: Fatigue load in axial direction at lower brace

Especially the loads in the jacket leg show very comparably characteristics as in the transition piece. The share of wave loading is again negligible for this wind turbine – support structure configuration.

## 5.2.2 Identification of Innovations

As seen in a first comparison of tower base moments over wind speed for the first version of the reference control, there is a need for improvements and innovations in terms of control adjustments and for load mitigation. As stated in the description of the reference support structure design [OLD02], the fatigue loads in the lower legs and braces is increased to such an extent that the requirement of 20 years lifetime could not be fulfilled. A discussion in Deliverable D4.1.1. [OLD08] already listed manifold innovations on control or structural side to induce additional damping or to dissipate loads. In the following, possible concepts will be listed. Some of them were already investigated and are presented in the following sections. Some of them are analysed at the moment and will be presented in the upcoming deliverables.

### Tower fore-aft damping

Damping of the tower fore-aft motion by collective pitch is state-of-the-art and applied in industry. This feature is included meanwhile in the updated reference control of the INN WIND.EU reference turbine. It is only affecting the fore-aft loads in full load range. As is shown in Figure 5.2-28, the partial load range is due to the high occurrence during life time in combination with the relatively high fatigue loads much more critical than the full load range. The effect of the tower fore-aft damper on pitch activity, tower bottom fatigue loads and power quality has therefore to be assessed.

### Speed exclusion window

The speed exclusion window is one of the main improvements from the original reference to the updated reference control. It should already lead to very large reduction of fatigue loads in the partial load range where the fatigue loads are highly increased due to resonances of the rotor speed with natural frequency of the tower. The results are found in section “Comparison of old and new reference control”.

### Mitigation of sideways excitations

Sideways excitation could be mitigated by generator torque control or individual pitch control. Both concepts have advantages and disadvantages as described in [OLD08]. However, these two concepts might have a relevant impact on the sideways excitation. The will be investigated for the next deliverable. In addition, a trade-off study when to apply controls for load mitigation is important and will there be shown.

Two additional concepts, which are more on the structural than on the control side, are also evaluated.

### Natural frequency variation of the support structure and tower

As mentioned earlier, the main challenge in partial load is the excitation of the natural frequency of the tower and support structure system. To understand the basic principle and to estimate the impact and magnitude, a natural frequency variation was carried out. The results are shown in the section “Influence of natural frequency on fatigue loading”.

### Passive, semi-active and active dampers

Passive dampers, namely tuned mass dampers integrated in the nacelle, are one of the structural possibilities to dissipate energy and therefore mitigate loads. The concept is about to be evaluated at the moment and will be presented in the upcoming deliverables. More advanced structural interferences such as semi-active and active structural control will also be investigated and contributed to the next deliverables.

## 5.2.3 Preliminary studies of innovations on component level

### Comparison of old and new reference control

In a second iteration, the controller was adjusted to the final reference support structure design. The rotor speed was excluded to not excite the tower natural modes. A comparison of old and new control is shown in the following.

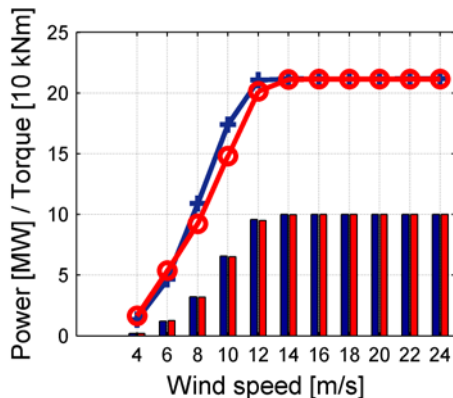


Figure 5.2-26: Comparison of old (blue/cross) and new (red/circle) reference control for power (bars) and torque (lines)

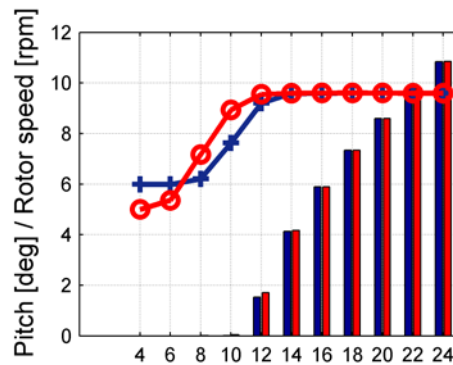


Figure 5.2-27: Comparison of old (blue/cross) and new (red/circle) reference control for pitch angle (bars) and rotor speed (lines)

The main difference between the old and new reference control is the torque-rotor speed relation. The minimal rotor speed is decreased and, in addition, the rotor speed for the wind speeds from 8-12 m/s is increased. Therefore, the torque over wind speed is reduced consequently. The power as seen in Figure 5.2-26 is minimally decreased which will have an impact on the annual energy yield. Simulations were carried out to estimate the impact of the changes in the reference control on the wind turbine loads.

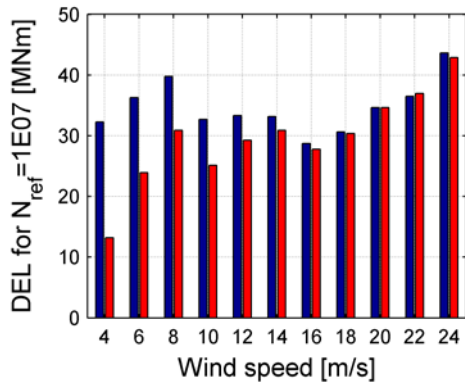


Figure 5.2-28: Comparison of old (blue) and new (red) reference control for fore-aft DELs at tower base

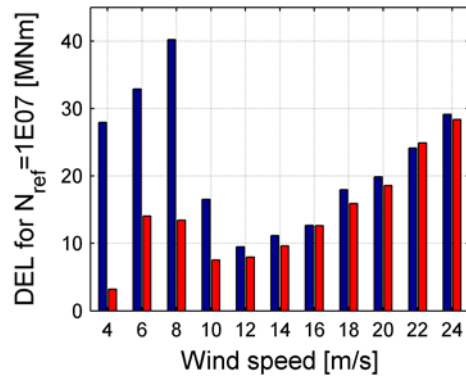


Figure 5.2-29: Comparison of old (blue) and new (red) reference control for sideways DELs at tower base

As can be seen, the reduction of minimal rotor speed at cut-in and the fast ride-through or exclusion strategy of natural frequency range already leads to significant reductions in fore-aft as well as side-to-side fatigue loads at the transition piece. Whereas figure 4-28 illustrates the fore-aft reduction over the wind speed range from 4-14 m/s, the reduction in sideways fatigue loading is made very clear in figure 4-29. Especially the sideways fatigue loads are reduced by over 2/3 of the original value.

### Control features

The updated controller furthermore includes the possibility to use tower acceleration signals for collective pitch control to mitigate fore-aft accelerations. However this feature could not be tested due to issues with the reference control. The investigation will be presented in the next deliverable.

The comparison shown in the following covers the updated control with constant torque control objective in the full load region and constant power.

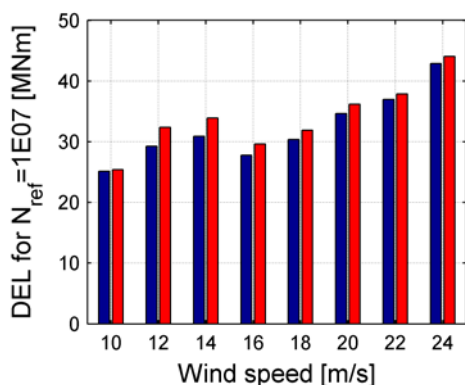


Figure 5.2-30: Fore-aft fatigue loads for constant torque (blue) and constant power (red) strategy

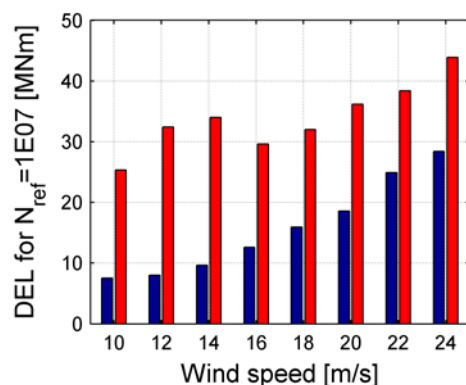


Figure 5.2-31: Sideways fatigue loads for constant torque (blue) and constant power (red) strategy

As shown in Table 5.2-5, the influence of varying torque in full load range on fore-aft fatigue loads is minor whereas the effect on the sideways loading is crucial. Increases of up to 300% are reached when aiming for constant power instead of constant torque in the full load region.

**Table 5.2-5: Relative change of fatigue loads of old and new reference control**

		Wind speed [m/s]							
		10	12	14	16	18	20	22	24
Increase in DEL	Sideways	3.36	4.06	3.53	2.35	2.01	1.95	1.54	1.55
	Fore-aft	1.01	1.11	1.10	1.07	1.05	1.04	1.02	1.03

### 5.2.4 Interim conclusion and assumed impact of innovations on component level

After the investigation of the fatigue loads acting on the reference turbine and support structure, the following aspects can be concluded:

- The design of the control with respect to the rotor speed is crucial for the wind turbine loading
- A redesign of the rotor and drive train might be one option to overcome the actual resonant design, caused by the support structure requirements
- The selection of constant torque against constant power control strategy has a major impact on fatigue loads in the full load range
- Further evaluation of the control concepts for mitigation of fore-aft and side-to-side loads are necessary [OLD08] and on the agenda for the next deliverable
- Structural control strategies might be advantageous as the main excitation is due to resonance effects for this turbine-support structure configuration

### References

- [OLD01] Deliverable D1.21, “D121-DTU10MWReferenceWindTurbine.xls”, Internal teamsite, uploaded 2013-09-06, accessed 2014-08-12
- [OLD02] INN WIND.EU Design report – Reference Jacket, “InnWind\_DesignReport\_ReferenceJacket\_Rev00.docx”, Internal teamsite, uploaded 2014-01-16, accessed 2014-08-12
- [OLD03] Popko, W.; Vorpahl, F.; Zuga, A.; Kohlmeier, M.; Jonkman, J.; Robertson, A.; et al, “Offshore Code Comparison Collaboration Continuation (OC4), Phase I – Results of Coupled Simulation of Offshore Wind Turbine with Jacket Support Structure.”, The Proceedings of the Twenty-Second (2012) International Offshore and Polar Engineering Conference, 17–22 June 2012, Rhodes, Greece. Vol. 1, pp. 337-346. International Society of Offshore and Polar Engineers (ISOPE), (<http://www.nrel.gov/docs/fy12osti/54124.pdf>.)
- [OLD04] Deliverable D1.21, “D121ControllerDescription-LandVersion.pdf”, Internal teamsite, uploaded 2013-09-06, accessed 2014-08-12
- [OLD05] International Electrotechnical Commission, “IEC 64100-3: Wind turbines Part 3: Design requirements for offshore turbines”, 2009
- [OLD06] Fischer, T.; de Vries, W.; Schmidt, B., “Upwind Design Basis (WP4: Offshore Foundations and Support Structures)”, 2010

- [OLD07] Kühn, M., “Dynamics and Design Optimisation of Offshore Wind Energy Conversion Systems”,2001
- [OLD08] Kuhnle, B.; et. al, “Deliverable D4.11 – State of the art on component level”, 2013

### 5.3 Load-mitigating controls (FhG-KS)

#### 5.3.1 Speed exclusion zone

This paragraph mainly cites [FhG-KS01]. Speed exclusion zones, also called rotational speed windows or tower resonance bridging, can be useful when the rotor speed (1P) or blade passing frequency (3P) excites a structural resonance at a certain operating point, see e.g. [FhG-KS03, FhG-KS04]. Such resonances can be avoided by choosing the turbine's natural frequencies outside the operational excitation ranges. However, sometimes this is not possible. This is shown in the Campell diagram in Figure 5.3-1, where the frequency of the 1<sup>st</sup> tower mode lies within the operational rotor speed range. At the red dot, the 1P-line cuts the dash-dotted line indicating the natural frequency. That is, when the system operates near this operating point, a vibration with the 1<sup>st</sup> tower frequency will be excited.

A speed exclusion zone can be employed in order to avoid this phenomenon. This means that the control system is modified such that the critical speed range includes no stable operating points. Thus, the rotor speed will rapidly drive through the critical speed range without severely exciting the natural frequency. Usually, this is implemented by modifying the speed-torque curve of the generator, see [FhG-KS03] and [FhG-KS05] for two implementation alternatives.

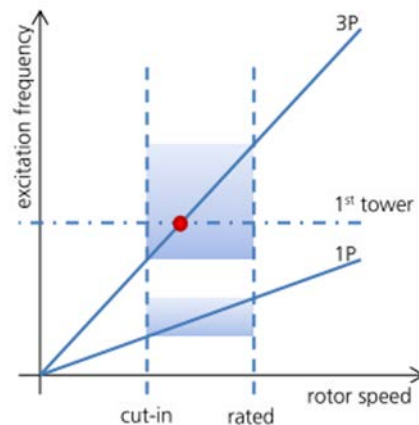


Figure 5.3-1: Campell diagram. The red dot indicates an operating point where the 1<sup>st</sup> tower mode is excited by the rotor speed (1P).

#### 5.3.2 Peak Shaving

Following the standard operating strategy (speed-torque curve below rated and speed regulation with collective pitch above rated), the steady state thrust force on the rotor plane peaks at rated wind speed, see the dashed line in the middle plot in Figure 5.3-2. This usually causes high bending moments in the tower bottom and is critical both in terms of fatigue and extreme loads.

Applications so called “Peak shaving” or “thrust clipping” is a strategy that reduces the maximum steady state thrust force. The basic idea is to begin pitching the blades slightly below rated wind speed, see the solid line in the left plot in Figure 5.3-2, which reduces the thrust force in the critical range.

Simultaneously to shaving the thrust force peak the power capture in the transition region is reduced (right plot). Therefore, the design of a peak shaver is strongly subject to the trade-off between load mitigation and energy yield. Since its implementation is very simple it is often used as a last resort e.g. for meeting site-specific requirements. For offshore sites with considerable wave excitation, the reduction of aerodynamic damping must also be taken into account.

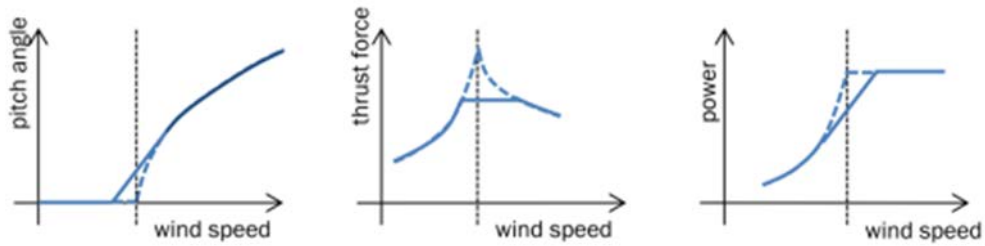


Figure 5.3-2: Steady operating points with peak shaving (solid line) and without (dashed line).

Reducing the maximum steady state thrust force by pitching the blades slightly below rated wind speed is applied as follows. Figure 5.3-3 shows the recommended pitch angle plotted against the generator moment. In this connection two variables are introduced namely the maximum peak shaving pitch angle (value between 0° and 5°) and the peak shaving gain (value between 0.6 and 0.9) multiplied by the nominal generator moment.

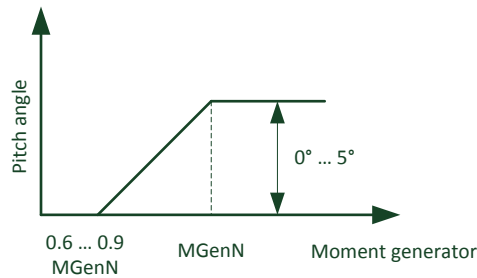


Figure 5.3-3: Recommended pitch angle plotted against the generator moment

Figure 5.3-4 shows the bending moment (tower foot) plotted against wind speed. The array of curves start at peak shaving gain value 0.9 and decrease stepwise with 0.05 to 0.6. At value 0.7 the curve is nearly flat. So, in this example the maximum peak of tower foot bending moment is reduced to 80 %.

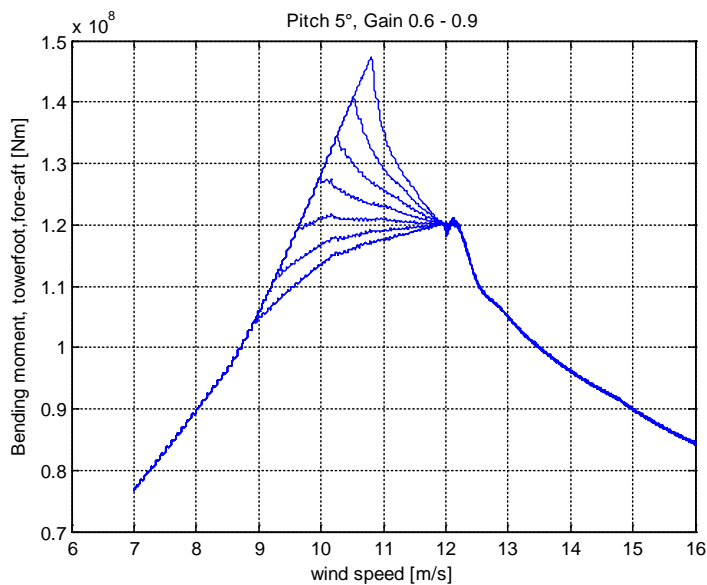


Figure 5.3-4: Bending moment, tower foot

Figure 5.3-5 shows the numeric results for different pitch angles with peak shaving gains also obtaining peak-free bending moment curves. As mentioned above, the design of a peak shaver is strongly subject to the trade-off between load mitigation and energy yield. Corresponding to Figure 5.3-5, the energy yield is shown in Figure 5.3-6. With knowing the wind conditions at the on- or offshore location one may optimize the peak shaving procedure.

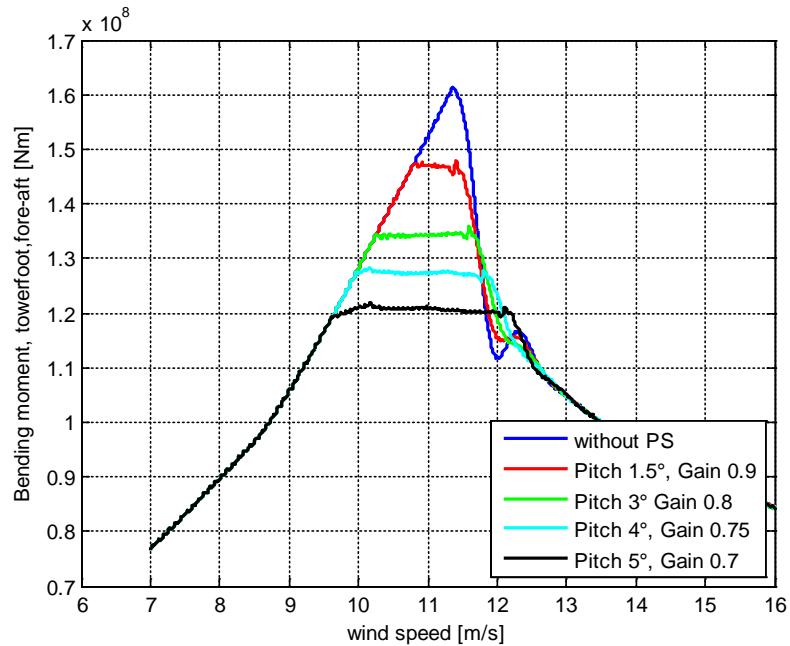


Figure 5.3-5: Bending moment, tower foot, peak-free

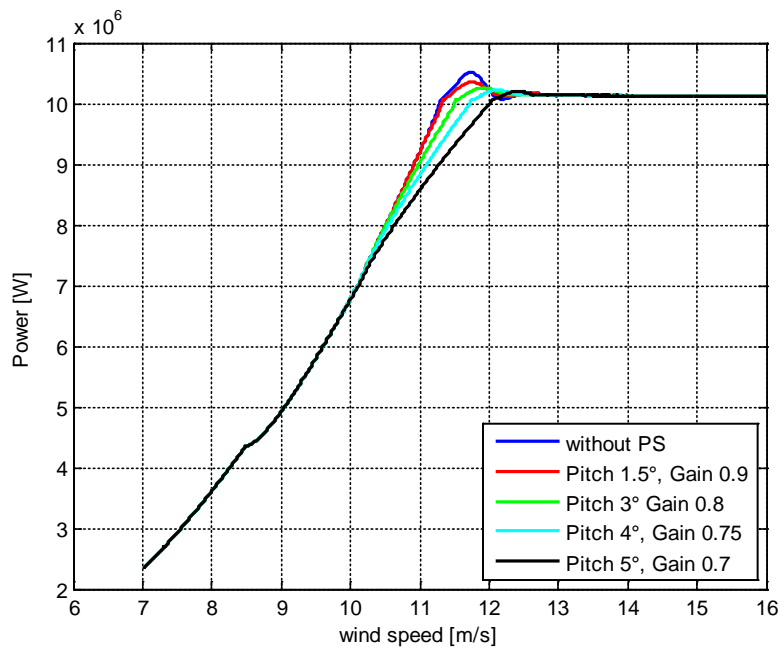


Figure 5.3-6: Power, peak-free

### 5.3.3 Active tower damping

The following sections mainly cite [FhG-KS01] and [FhG-KS02]. Controlling the pitch angles and generator torque allows for the active damping of vibrations of the support structure. This can be done in the fore-aft as well as in the side-side direction. The actuators are used in a feedback control loop to generate counter-acting forces and moments that reduce the motions of the structure. Usually, the motions are measured by accelerometers mounted on the tower top. To realize a damping effect it is necessary to generate a force that is inversely proportional to the velocity. Hence, the design of the closed loop system includes a filter design to assure an appropriate phasing.

Because the resulting control signals are added to those of the normal operating control loops, the coupling between the different control loops must be taken into account. This is not trivial especially when actuator amplitude and rate constraints are active. Furthermore, active load mitigation is in general subject to a “waterbed effect”: When loads in a certain range in the frequency domain are reduced they will be increased in another range. And, more generally, when loads at a certain part on the turbine are reduced they will be increased on other parts. Consequently, different objectives must be balanced, and the application of mitigation strategies for the support structure requires a broad knowledge of the overall turbine design, see also the subsection on integrated design below.

A classification of different variants regarding actuator and motion direction is given in Table 5.3-1. These are discussed in detail in the following. Figure 5.3-7 shows how the different actuators affect forces and moments on the tower top.

Table 5.3-1: Different variants for active tower damping

<b>Collective pitch angle</b>	✓	✗
<b>Individual pitch angle</b>	✓	✓
<b>Generator torque</b>	✗	✓

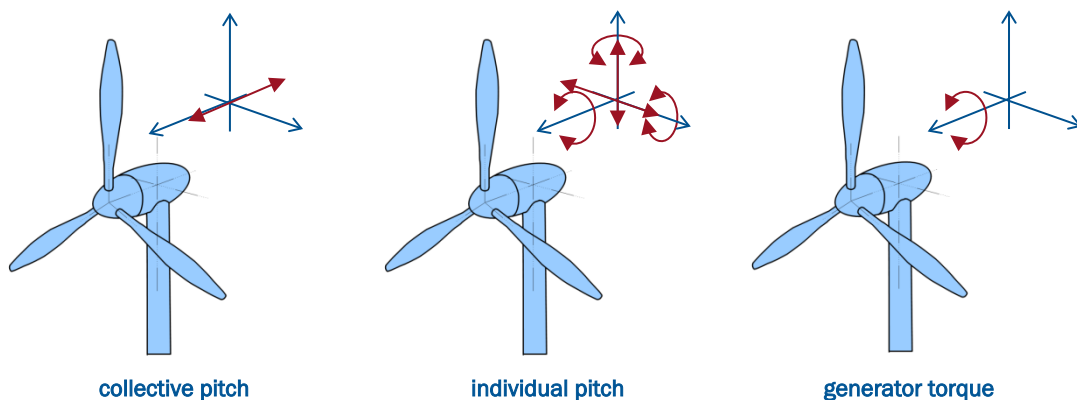


Figure 5.3-7: Different actuators for active tower damping and their effective force/moments on the tower top (red arrows).

The most widely spread variant is the damping of the 1<sup>st</sup> fore-aft tower mode for fatigue load reduction. For that purpose the fore-aft acceleration is fed back to the collective pitch angle using an appropriate filter. Consequently, a counter-acting thrust force on the rotor plane damps the tower vibration, see Figure 5.3-7. Changing the collective pitch angle also has an influence on the normal rotor speed regulation. But, this is usually not a major issue because the frequency of pitch angle variations due to the active tower damping is in most cases greater than the bandwidth of the properly designed rotor speed control loops. More critical is the potential coupling with blade flap modes, see [FhG-KS07].

Depending on the specific turbine design, it might be beneficial to mitigate not only the vibrations related to the 1<sup>st</sup> tower mode. For example, in [FhG-KS08] it is shown that also tower loads related to 3P harmonic excitation can be reduced using the same feedback structure. Another variant is dedicated to the 2<sup>nd</sup> tower mode. This is especially interesting for offshore turbines because this mode is easily excited by the waves. However, controlling the pitch angles individually is sometimes superior in this case: Depending on the actual shape of the 2<sup>nd</sup> mode, the tilting of the nacelle might be dominant. Then, an individual pitch control strategy that generates a tilt moment is more effective.

The so called “Individual pitch control” (IPC) has been heavily discussed in literature for quite some time, see e.g. [FhG-KS09, FhG-KS10]. It has been suggested for the reduction of loads on various components, which also includes the support structure. As shown in the middle of Figure 5.3-7 it offers a wide range of forces and moments on the tower top. The measurements used for feedback include tower top acceleration in side-side direction, blade bending moments, or bending moments measured on the mainframe.

The most obvious idea for the support structure is the damping of the side-side motion [FhG-KS11 – FhG-KS13]. This motion is being counteracted by a side-side force or a roll moment on the nacelle. For onshore turbines the tower side-side fatigue loads are usually less important as compared to those in fore-aft direction. In contrast, the support structure of offshore turbines can experience significant fatigue loads in the side-side direction. Especially wind-wave-misalignment induces side-side motion because of the low aerodynamic damping [FhG-KS06].

From the overall control system’s point of view the coupling with the rotor speed control loop has to be considered. Furthermore, because the blades are actuated independently, either multivariable control design or a preliminary decoupling by a transformation must be carried out. The non-linear mapping, known under different names as “d-q axis-”, “Coleman-”, or “multiblade-” transformation, transforms rotating quantities into a non-rotating frame. In both cases significant amount is necessary for addressing issues like extreme loads induced by rotor asymmetry during shut-downs [FhG-KS14] and pitch system amplitude and rate constraints [FhG-KS15]. The latter can be an issue mainly in the operating regime around rated wind speed because large pitch angle variations are necessary.

The active side-side damping is also possible modifying the generator torque [FhG-KS18]. To this end, the side-side acceleration is fed back to the demanded generator torque using an appropriate filter. The generator torque is supported by the main frame and, thus, leads to a counter-acting roll moment on the tower top (Figure 5.3-7). Due to the couplings between the various subsystems the interaction with the rotor speed control loop and the tower fore-aft loads has to be taken into account.

The enormous number of papers dealing with results from simulation studies contrasts with the little number of field-tests described in the literature. Some creditable exceptions include [FhG-KS14, FhG-KS17 – FhG-KS20]. These studies have been carried out on onshore turbines. Nevertheless, the reported results demonstrate the efficacy of the investigated load mitigation strategies by showing compliance with results obtained from simulations.

Figure 5.3-8 shows a block schematic of the overall system. There are two distinct control loops:

- The usual rotor speed controller that feeds back the generator speed to the collective blade pitch for the region above rated wind speed, and
- the tower damping controller that feeds back the tower top acceleration in fore-aft direction to the collective blade pitch.

The wind speed is a disturbance input of the closed loop system. Three additional outputs are used for performance evaluation, i.e. the tower bottom bending moment in fore-aft direction, the actual collective blade pitch, and the collective out-of-plane blade bending moment of the blade roots. The user has to provide linear models of the wind turbine and the rotor speed controller for each operating point.

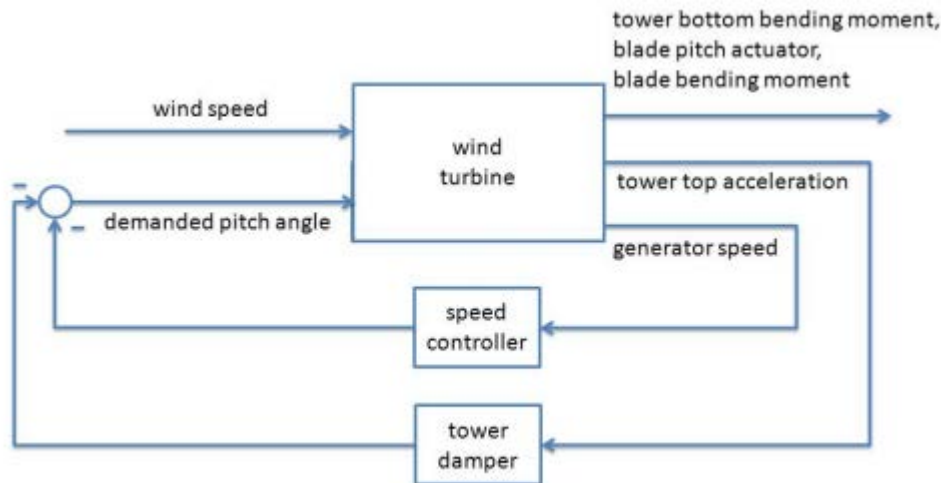


Figure 5.3-8: Block schematic of the overall control system.

The implemented structure of the tower damping controller consists of a series connection of

- a differentiator,
- three first-order low pass filters,
- a time delay, and
- a notch filter:

$$F_R(s) = k_R \cdot F_{3p}(s) \cdot e^{-T_d s} \cdot \frac{s}{(\frac{1}{2\pi f_1} s + 1)(\frac{1}{2\pi f_2} s + 1)(\frac{1}{2\pi f_3} s + 1)}$$

The bandwidths  $f_i$  of the low pass filters can be used to accurately tune the phase response. The notch filter is used to mitigate 3p activity of the pitch system. While the notch frequency is fixed  $1/T_f$  with respect to the rotor speed at the given operating point, its width and depth is shaped using two parameters:

$$F_{3p}(s) = \frac{T_f^2 s^2 + T_f k_{bw} k_{gain} s + 1}{T_f^2 s^2 + T_f k_{bw} s + 1}$$

The time delay is not a design parameter. It can be used e.g. to reflect delays of the communication etc.

In the scope of the numerical simulation with focus on the first tower frequency, three operating points are investigated namely for wind speed 8m/s (partial load operation), 12m/s and 16m/s. The notch filter remains unused because in this case there was no improvement in tower damping achieved.

Figure 5.3-9, Figure 5.3-10 and Figure 5.3-11 show the transfer functions from wind speed to tower acceleration by using an active tower damper. In all three operating points nearly -6dB magnitude loss is achieved at the frequency range about 0.3 Hz. A further increase of first tower mode damping leads to steady rise of close-by peak at 0.5 Hz.

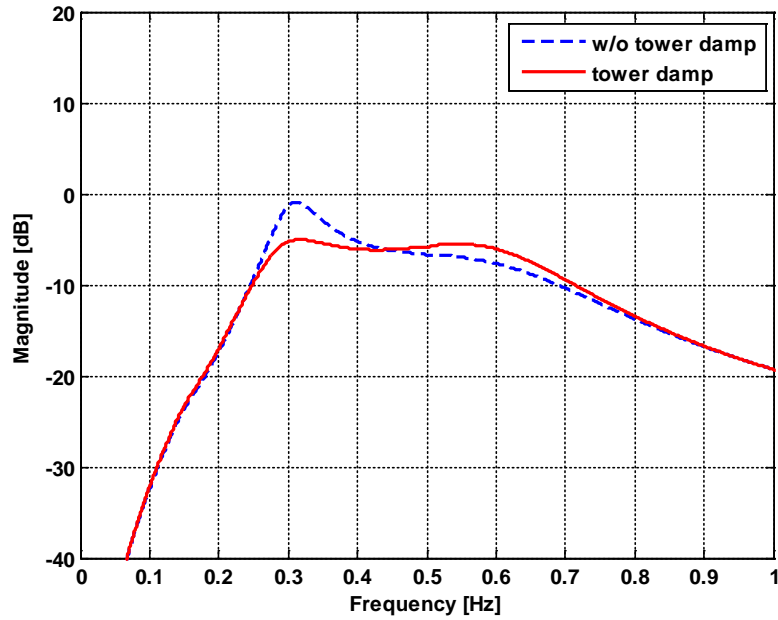


Figure 5.3-9: Active tower damping, first tower mode, wind speed 8 m/s

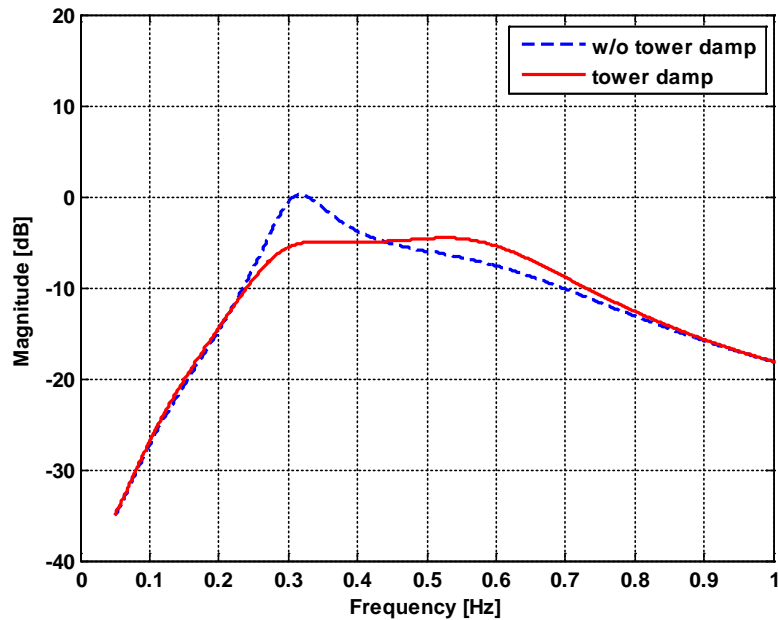


Figure 5.3-10: Active tower damping, first tower mode, wind speed 12 m/s

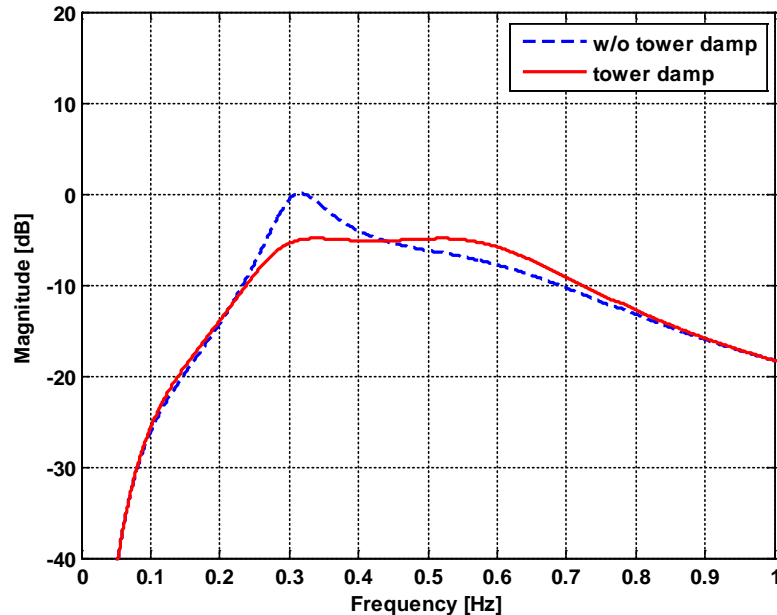


Figure 5.3-11: Active tower damping, first tower mode, wind speed 16 m/s

## References

- [FhG-KS01] B. Fischer, M. Shan, "A survey on control methods for the mitigation of tower loads", Project report, Kassel, 2013.
- [FhG-KS02] B. Fischer, "GUI for Tower Damping Controller Design", Kassel, 2013.
- [FhG-KS03] T. Burton, D. Sharpe, N. Jenkins, and E. Bossanyi, Wind energy handbook, 2nd ed. Chichester: Wiley, 2011.
- [FhG-KS04] S. Siegfriedsen, "Method for operating offshore wind turbine plants based on the frequency of their towers" US 6891280 B2. 2001.
- [FhG-KS05] P. Schaak, G.P Corten, and E.L van der Hooft, "Crossing resonance rotor speeds of wind turbines," in EWEC 2003, Madrid, 2003.
- [FhG-KS06] T. Fischer and W. de Vries, "Final Report Taks 4.1: Integration of support structure and wind turbine design: Deliverable D 4.1.5 (WP4: Offshore Foundations and Support Structures)," 2011.
- [FhG-KS07] W. E. Leithead, S. Dominguez, and C.J. Spruce, "Analysis of Tower/Blade interaction in the cancellation of the tower fore-aft mode via control," in EWEC 2004, London, 2004.
- [FhG-KS08] Weiwei Shan and Martin Shan, "Gain Scheduling Pitch Control Design for Active Tower Damping and 3p Harmonic Reduction," in EWEA 2013, Proceedings, 2013.
- [FhG-KS09] P. Caselitz, W. Kleinkauf, T. Krüger, J. Petschenka, M. Reichardt, and K. Störzel, "Reduction of fatigue loads on wind energy converters by advanced control methods," in EWEC 1997: Proceedings of the European Wind Energy Conference, Dublin, 1997, pp. 555–558.

- [FhG-KS10] E. A. Bossanyi, "Individual Blade Pitch Control for Load Reduction," *Wind Energ*, vol. 6, no. 2, pp. 119–128, 2003.
- [FhG-KS 11] S. Wortmann and T. Krüger, "Method for operating a wind energy system" W02009/083085 (A1). 2008.
- [FhG-KS 12] D. Duckwitz and M. Geyler, "Active damping of the side-to-side oscillation of the tower," in *DEWEK 2010: 10th German Wind Energy Conference*, Bremen, 2010.
- [FhG-KS 13] Felix Hess and Boris Buchtala, "Method and Device for Preventing a Lateral Oscillation of a Wind Power Installation" US20130209254 A1. 2011.
- [FhG-KS 14] M. Shan, J. Jacobsen, and S. Adelt, "Field Testing and Practical Aspects of Load Reducing Pitch Control Systems for a 5 MW Offshore Wind Turbine," in *EWEA 2013, Scientific Proceedings*, 2013, pp. 101–105.
- [FhG-KS 15] Stoyan Kanev and Tim van Engelen, "Exploring the Limits in Individual Pitch Control," in *EWEC 2009*, 2009.
- [FhG-KS 16] T. van Engelen, E. van der Hooft, and P. Schaak, "Development of wind turbine control algorithms for industrial use," in *EWEC 2001*, Copenhagen, 2001.
- [FhG-KS 17] M. Rossetti and E. Bossanyi, "Damping of tower motions via pitch control – theory and practice," in *EWEC 2004*, London, 2004.
- [FhG-KS 18] M. Städler, "Controls for Load Reduction," in *DEWEK 2008: 9th German Wind Energy Conference*, Bremen, 2008.
- [FhG-KS 19] Ervin Bossanyi, Alan Wright, and Paul Fleming, "Controller field tests on the NREL CART2 turbine: Upwind Project, Deliverable 5.6.1," 2010.
- [FhG-KS 20] Svenja Wortmann and Henning Leweke, "REpower Field Test of Active Tower Damping: Upwind Project, Deliverable 5.6.3," 2011.

## 6 MANUFACTURING (RAMBOLL)

The objective of the first part of this chapter is to describe different Jacket Transition Piece Concepts and their advantages as well as disadvantages with respect to fabrication costs. Several studies have been performed in order to determine governing parameters and their influence on the TP's structural behaviour as well as on the jacket. Further technical studies as well as cost evaluations are required in order to establish an efficient cost optimisation strategy.

The second part of this chapter refers to a cost optimisation of the jacket fabrication process. Three examples of possible fabrication strategies are presented and evaluated. Furthermore, the share of the four main fabrication cost contributors – namely material, welding, coating and assembly costs - is shown based on an example jacket structure. It is expected that the ongoing process of improving the developed cost evaluation tool can further decrease the fabrication costs of future jacket structures.

### 6.1 Jacket Transition Piece Concepts

#### Introduction

Jacket foundations are characterized by a number of legs, which are stiffed by braces. The Transition Piece (TP) connects the tower with the jacket and transfers the loads from the tower bottom to the jacket. Consequently, TPs are primarily designed to resist the loads and comply with the Operation & Maintenance (O&M) as well as manufacturing requirements. However, it is a challenge to find the best fit for a given project; different TP concepts influence the structural behaviour of the Jacket. Furthermore, the secondary steel and O&M requirements must be taken into account.

In order to compare different TP concepts, several studies have been performed for determining governing parameters and their influence on the structural behaviour and on other requirements of the jacket. These parameters have been separated into *hard* and *soft* parameters which are characteristic for the respective TP concept, see Figure 6.1-1. Hard parameters have a measureable effect, e.g. the mass of TP, the total length of the welds and the surface area for coating). Soft parameters have no – at least not a straightforward - measurable effect and are often linked to O&M requirements and the level of manufacturing. Potential patent issues might in some cases play a role as well.

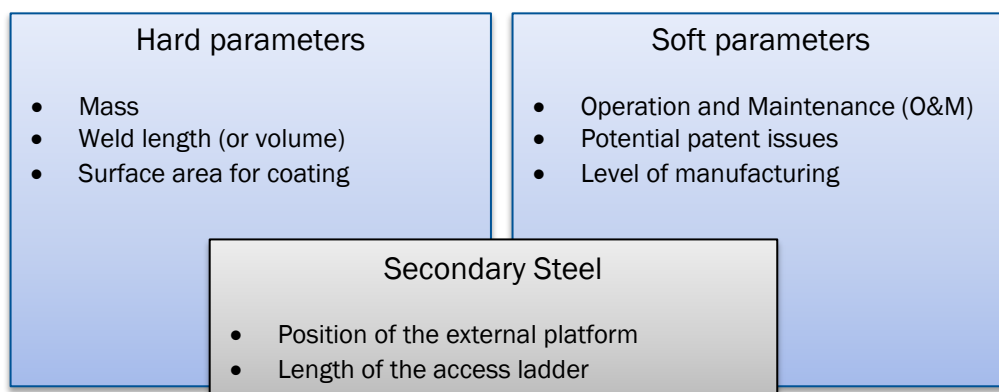


Figure 6.1-1: Identification of different parameters influencing the TP design

In the following, an overview of the most common TP concepts is given (section 0) followed by a more detailed evaluation of the respective TPs' characteristics (section 6.1.1). In this evaluation the "box girder model", the "strut model" and the "I-extreme model" will be considered.

## Overview

In this section an overview of different TP concepts is given. The most common concepts are the “box girder model”, the “strut model” and the “I-extreme model”. Each concept can be realised with a considerable amount of variations and subsets. The focus of this evaluation is on the simple concepts, which are described and evaluated in the following. Some possibilities to improve the concepts are evaluated in Chapter 6.2.

### Simple “box girder model”

The simple box girder model relies on horizontal and vertical girders which are connected with the bottom tower section and the jacket legs. The bending moment at the tower bottom is transferred into a pair of axial forces at the upper jacket legs. The connection between the centre can section and jacket legs is designed with a box girder consisting of a bottom flange, a top flange and two web plates, see Figure 6.1-2. All connections are welded.

Depending on the height-to-length ratio of the girders, the box girder concept model leads to high bending moments at the girders. This can be regarded as potentially inefficient since the load transfer relies heavily on bending which is the most inefficient way of transferring loads (compared to a load transfer via axial forces).

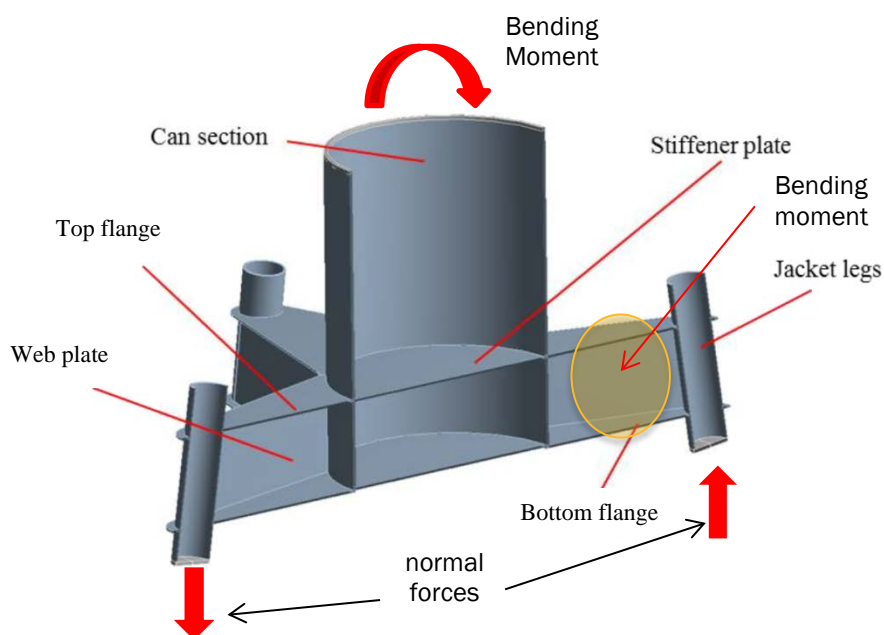


Figure 6.1-2: Simple box girder

The main advantage of the box girder model lies in its O&M characteristics: The external platform is usually placed on the top of the top flange, see Figure 6.1-3; since there are no struts and beams on the top of the external platform, the O&M staff has a larger area for carrying out their work. Furthermore, the crane which is located at the external platform can rotate without constrains.

Regarding the access to the external platform, it has to be considered that the length of the access ladder is determined by the distance measured from the sea level to the external platform. A rest-platform is required if the length of the access ladder exceeds a certain limit. Since the installation of a rest platform raises costs, the positioning of the external platform must be considered thoroughly. Finally, the position and overall concept of the external platform depends on the individual customer’s requirements and priorities.

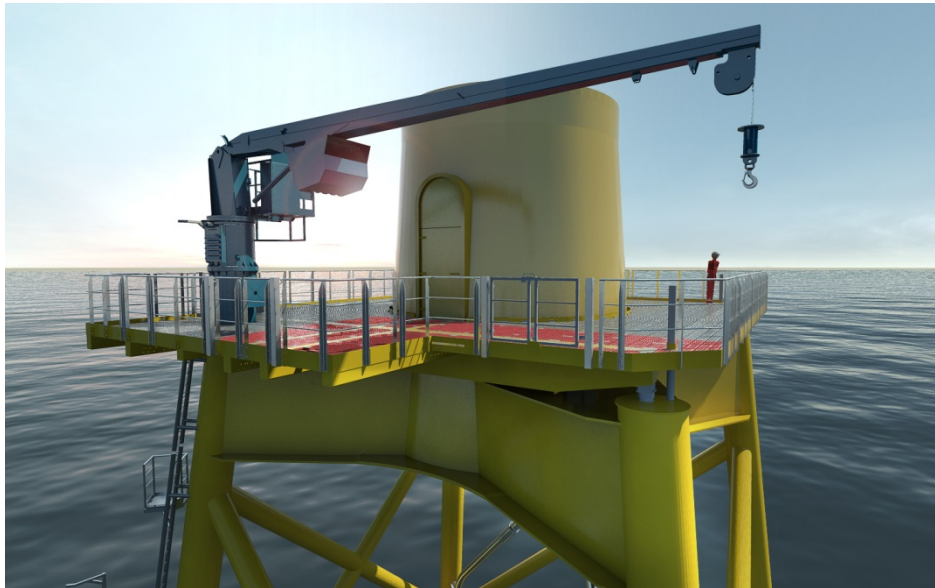


Figure 6.1-3: Box girder model with external platform placed on top of the top girder [Belwind Jacket]

### Simple strut model

The simple strut model consists of horizontal and inclined struts (lower and upper braces), see Figure 6.1-4. The connections to the centre can and chords are welded. The connections between the chord and the jacket legs are welded as well. Stiffener plates are usually added at the elevation of the lower braces in order to increase the torsional stiffness of the TP. Ring stiffeners can be introduced at the centre can where the upper braces introduce pushing shear.

While the overall load transfer of the box girder model is dominated by bending at its girders, the load transfer of the simple strut model is mainly governed by axial loads. Since the load transfer through axial forces is generally more efficient than the load transfer through bending moments, the strut model is expected to yield smaller material costs compared to the box girder model. On the other hand, additional costs may arise due to the stiffener plates and ring stiffeners at the centre can.

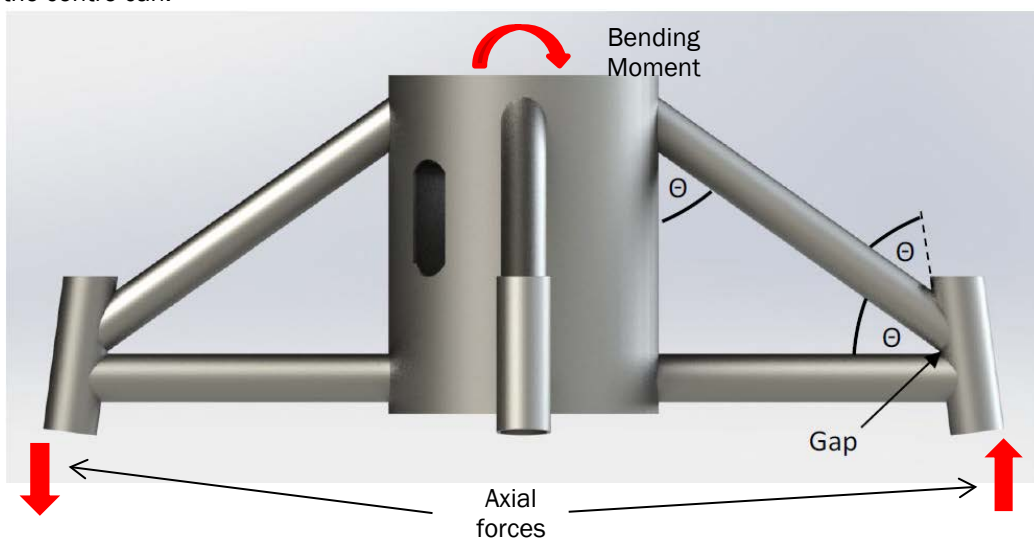


Figure 6.1-4: Simple strut Model

There are several options for placing the external platform: One option is offered by positioning the external platform on the top of the chords, see Figure 6.1-5.

In contrast to the box girder model, the strut introduces a major impact on the O&M requirements because there is generally not enough space for a full rotation of the crane due to the presence of the inclined upper braces. Other possible positions of the external platform are on the top of the lower braces and above the ring stiffeners. However, the access distance from the sea level to the external platform should be kept as short as possible in order to avoid additional costs.

Since the connection of the upper brace to the centre can must be located above the TP door, there is a minimum angle between the lower brace and upper brace. Consequently, the strut model generally requires a greater height compared to a box girder TP.



**Figure 6.1-5: Simple strut model with external platform to be placed on top of the TP chords [Fife Jacket]**

#### Simple “I-extreme model”

The simple I-extreme model consists of I-cross sections with a horizontal shear plate stiffener at the bottom and an inclined top flange, see Figure 6.1-6. All connections between the steel components are welded. Due to an increase of the girders’ height-to-length ratio the load transfer through the girder relies more on favourable axial forces than on bending, similar to what can be observed for the strut model. Consequently, the I-extreme model offers a solution requiring less steel than the box girder model. Additionally, it is expected that the connection of the girders to the centre can is facilitated when compared to the strut model concept.

The external platform is placed on top of the horizontal girder. The position of the external platform could introduce a problem in terms of O&M similar to the strut-model concept because the crane’s rotation might be limited and there is only a small opening inside the I-girder in order to walk around the centre can.

By using two web plates instead of only one I-cross section, an extension of the I-extreme model concept is offered (box-extreme). This extension corresponds to a box girder concept with inclined top flanges.

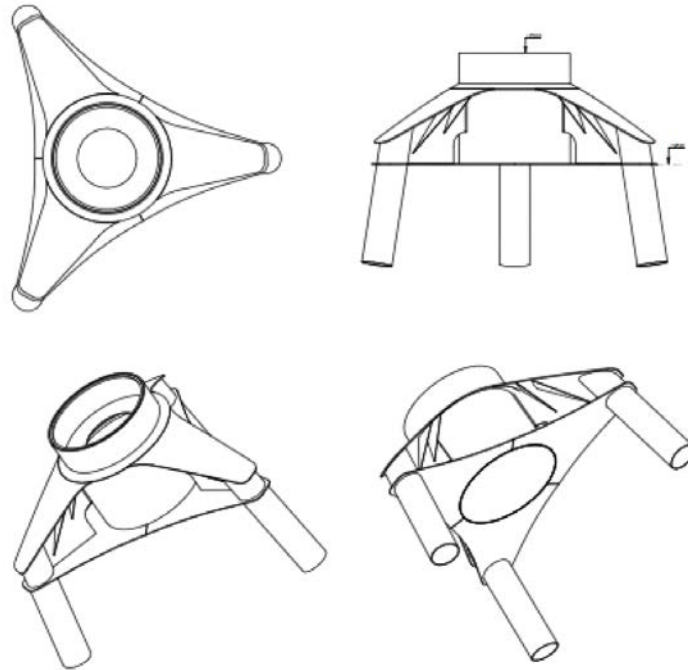


Figure 6.1-6: Simple I-extreme

### 6.1.1 Evaluation

The differences between the TP concepts are shown in this section. In a first step, CAD-models of the TP concepts were made using nearly the same wall thickness and global dimensions (e.g. TP top and bottom width). These CAD-models allow a comparison between certain hard parameters of the TPs which are described in the section below. Soft parameters are described at the end of this section.

#### Hard Parameters

TJs have a large number of measurable parameters like geometry parameters. Especially, the TJ mass and the total length of the welds are important because these parameters have a huge influence on the fabrication costs. The surface area for coating is a hard parameter as well. However, coating cost is not a large cost contributor. Table 6.1-1 shows a summary of hard parameters which have an influence on the fabrication costs.

The evaluation of the fabrication costs is derived from experience gained by setting up the cost model for jacket structures, see section 6.2.1. Fabrication costs consist of material, coating, welding and assembly costs. Material costs are expected to be approximately at the same level as welding costs. The length of weld can be used as an indicator for the welding costs. Material costs are not comparable by using the cost model for jacket structures because the box girder and I-extreme do not consist of tubular members. However, it is assumed that the lightest TJ concept generally leads to the lowest material costs.

When comparing the three TJ models, the strut model shows the least welding and material costs.

However, it must be noted that Table 6.1-1 is not the result of a detailed design review. Especially the TP mass could change by using a detailed design review. For a more detailed comparison of the TP concepts it is planned to perform finite element computations by using one consistent set of ULS and FLS loads. In that way it is possible to determine the detailed dimension of the TP concepts.

A lack of experience with assembling TPs makes it difficult to perform a precise cost evaluation for the assembly procedure. A simplified method for estimating assembly costs is offered by comparing the number of assembly components of the TP. The concept which has the least number of components would probably lead to the lowest assembly costs. Coating costs are expected to be only a minor cost factor.

### Soft Parameters

Soft parameters cannot be directly evaluated. Table 6.1-1 shows soft parameters, namely patent problems and level of manufacturing. The evaluation of soft parameters often depends on individual customer requirements: For example the box girder model could be preferred by the client because dropped objects cannot hit inclined braces (strut model) or inclined top flanges (l-extreme). Patent issues might lead to uncertainties about whether a concept is prone to introducing legal issues.

**Table 6.1-1: Parameter for comparison**

	Box girder	Strut model	l extreme
Platform	Top	Integrated	Integrated
Length of weld	Medium	short	long
Surface area for coating <sup>3</sup>	Low	Low	High
Weight of unity	Medium	Low	N/A
Patent problems	Yes	Yes	No
Level of manufacturing	Easy	Easy	Hard

### 6.1.2 Concept Study

This chapter gives a more in depth evaluation of the mechanical properties of the TP concepts simple box girder model, strut model and l-extreme model using a preliminary finite element model computation. The focus lies on the load transfer and the local hot spot stresses. Furthermore, the influence on the natural frequency of the overall structure and the load path within the jacket are evaluated.

#### Simple “box girder model”

The load transfer in the simple box girder model is dominated by bending moments at its girders. A load transfer through bending moments creates higher and lower utilized cross-sectional areas. The load transfer through axial forces would be more efficient because the whole cross-sectional area would be loaded uniformly. Typically, the maximum stresses in a beam loaded with bending moments are to be found at the flanges. Hot spot stresses are typically found at the connections of the girder and the TP can section, see Figure 6.1-7.

<sup>3</sup> Without secondary steel

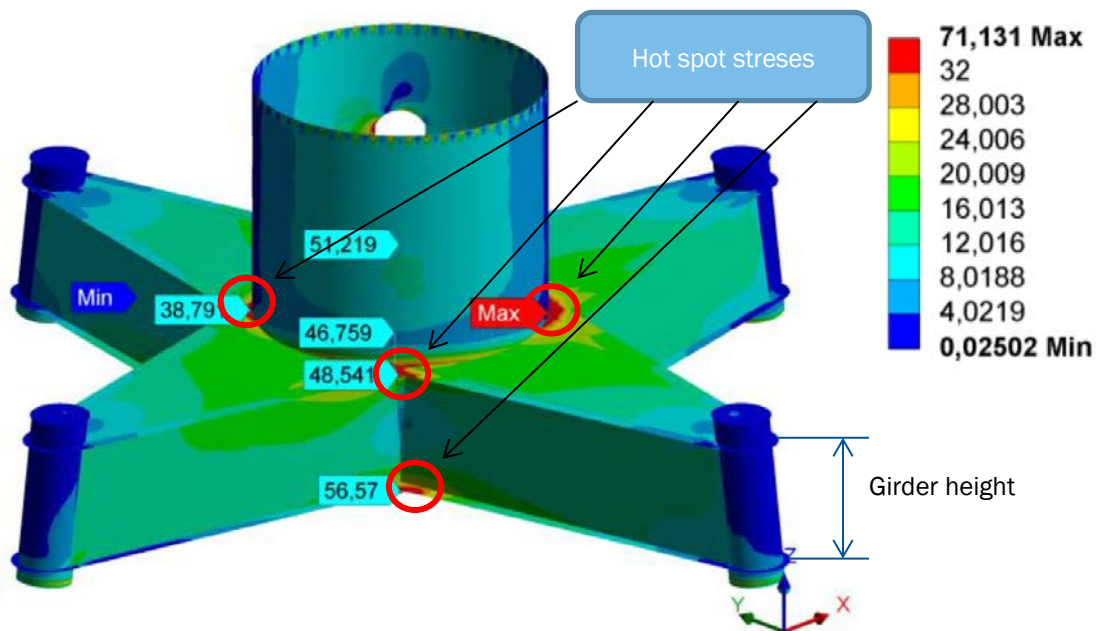


Figure 6.1-7: Simple box girder - fatigue analysis

### Simple “strut model”

The load transfer in the simple strut model is mainly governed by axial forces in its braces. As already explained, this is a potential advantage over the simple box girder model. Highly utilized areas are located at the connections of the upper strut and the TP can section as well as the connection of the web plate, see Figure 6.1-8. Another large utilized area is the bottom plate, see Figure 6.1-9.

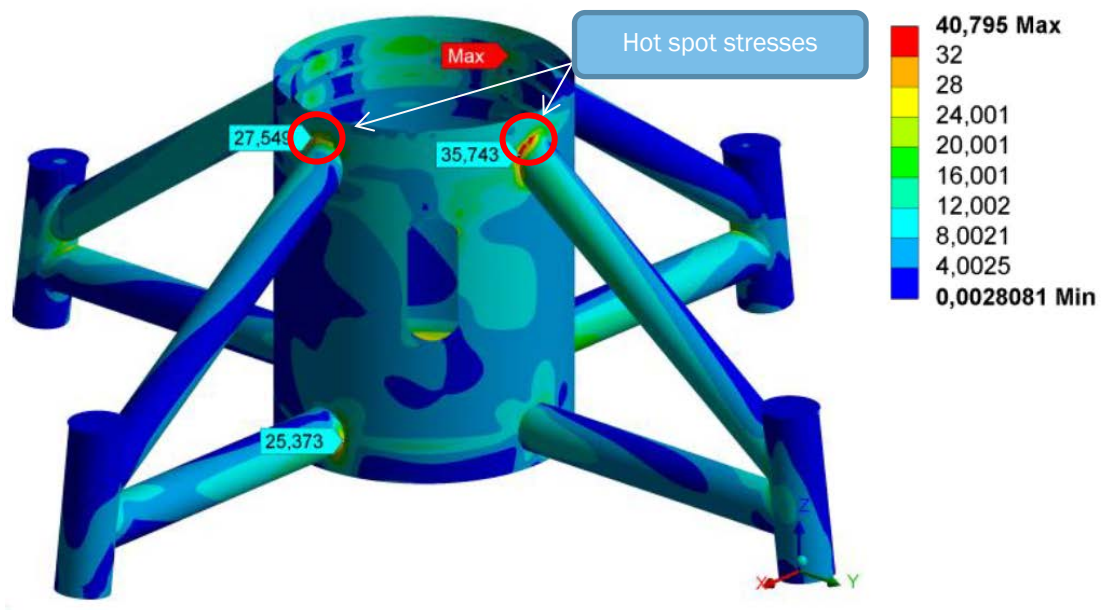


Figure 6.1-8: Strut model - fatigue analysis

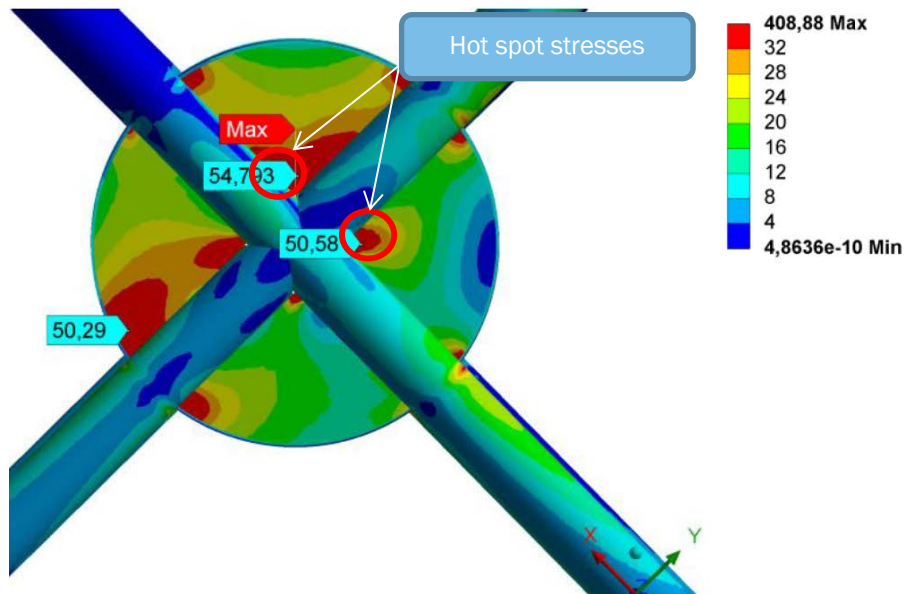


Figure 6.1-9: Bottom view of the strut model - fatigue analysis

#### Simple “I-extreme model”

The simple I-extreme model concept is designed for a three-legged jacket. Hence, the I-extreme concept cannot be compared directly with the strut model and the box girder concept which are both based on a four-legged jacket. However, this section is supposed to give only a general impression of important aspects of the simple I-extreme model concept. In the next stage of this project, detailed computations of the three TP concepts are planned by considering an identical load set-up and jacket structure.

With regard to hot spot stresses, large utilized areas can be found at the connections between the top plate and the can section. Other large utilized areas are the inner ring stiffener and the web plate, see Figure 6.1-10.

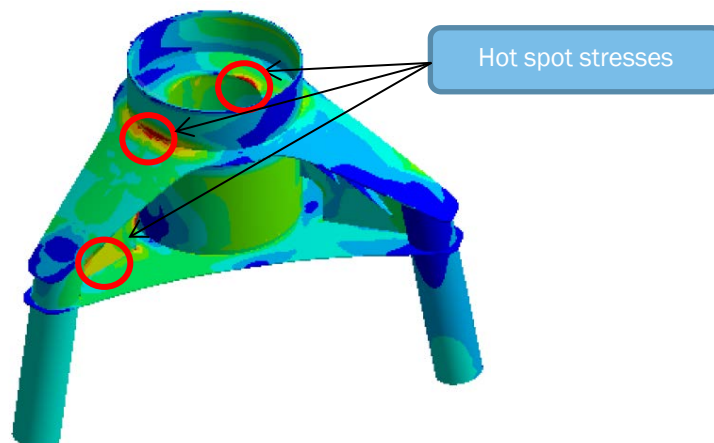


Figure 6.1-10: I extreme concept – fatigue analysis

Since the hot spot stresses have an important impact on the optimisation process of a TP model, further investigations of how to mitigate the stresses in these areas are necessary. Usually, ring stiffeners and/or stiffener plates are used in order to influence the loads transfer and to reduce

the hot spot stresses. The position and dimension of these stiffeners as well as their impact on the overall fabrication costs shall be investigated at a later stage of this project.

### **Influence on the jacket**

In general, there is a correlation between the first natural frequency of the overall foundation structure and the TP's lateral stiffness. A laterally stiffer TP increases the stiffness of the overall foundation structure. As a consequence, the natural frequency of the overall structure will increase as well. Compared to the strut model, the box girder model generally leads to a smaller natural frequency of the overall structure due to its smaller stiffness.

Furthermore, the stiffness of the TP has an influence on the load transfer in the upper part of the jacket: The load transfer of a less stiff TP causes less axial forces but higher bending moments in the jacket legs. The load transfer of a stiffer TP generates higher axial forces in the jacket legs but less axial forces in the braces.

When comparing the simple box girder and the simple strut model, the strut model is generally the laterally stiffer TP. Consequently, the simple strut model causes a higher utilization in the jacket legs, compared to the simple box girder concept. The simple box girder model tends to show higher utilizations in the upper jacket braces compared to the simple strut model. This behaviour can most probably be explained by the different lateral stiffness characteristic of the TP models.

However, a considerable influence of the different TPs on the jacket's load transfer can only be determined within the upper part of the jacket. Thus, there is no TP model concept which has the potential of reducing the amount of jacket steel significantly.

### **6.1.3 Conclusion**

The transition piece (TP) is an important part of the substructure design connecting the tower to the jacket. This evaluation considers three different TP concepts, namely the box girder model, the strut model and the I-extreme model. The focus of this evaluation is on the advantages and disadvantages of each concept.

The box girder shows the most flexible option for placing the external platform. Especially the surface area of the external platform and the crane range are important factors in this respect.

The strut model and the I-extreme concept show a more efficient load transfer by mainly relying on axial forces. This indicates that these concepts are most likely the preferred options when a mass reduction of TPs is aimed at. The I-extreme model is probably offering the lightest solution, but this should be confirmed by a more detailed calculation to be performed at a later stage of this project.

Furthermore, the evaluation of the different TP models confirms the impact of the TP on the jacket structure: Correlations between the first natural frequency of the whole structure and the lateral stiffness of the TP can be determined. Additionally, the TP has a considerable influence on the load distribution in the upper part of the jacket. However, the influence of the TP on the jacket decreases with increasing distance to the TP.

In order to evaluate the different TP concepts with respect to costs, a cost model is required which takes into account the main fabrication cost drivers. This could be done similarly as already achieved for the jacket structure.

## 6.2 Jacket Assembly Concepts and Cost Optimization

The optimization of jacket structures aims at a cost reduction. Three of the main cost contributors for jacket costs are fabrication, installation and transportation. The focus of this section lies on the fabrication costs. The fabrication costs consist of welding costs, material costs, assembly costs and coating costs. The goal is to minimize the fabrication costs by varying the geometry parameters of the jacket and to find the least expensive assembly strategy.

### 6.2.1 Fabrication cost model

This fabrication cost model includes the main cost contributors welding costs, material costs, assembly costs and coating costs. Each of the cost contributors has an influential parameter. The influential parameters are depended on geometrical parameters. Hence, it is possible to optimize the jacket by varying its geometrical parameters. An overview of the cost model set-up is shown in Figure 6.2-1.

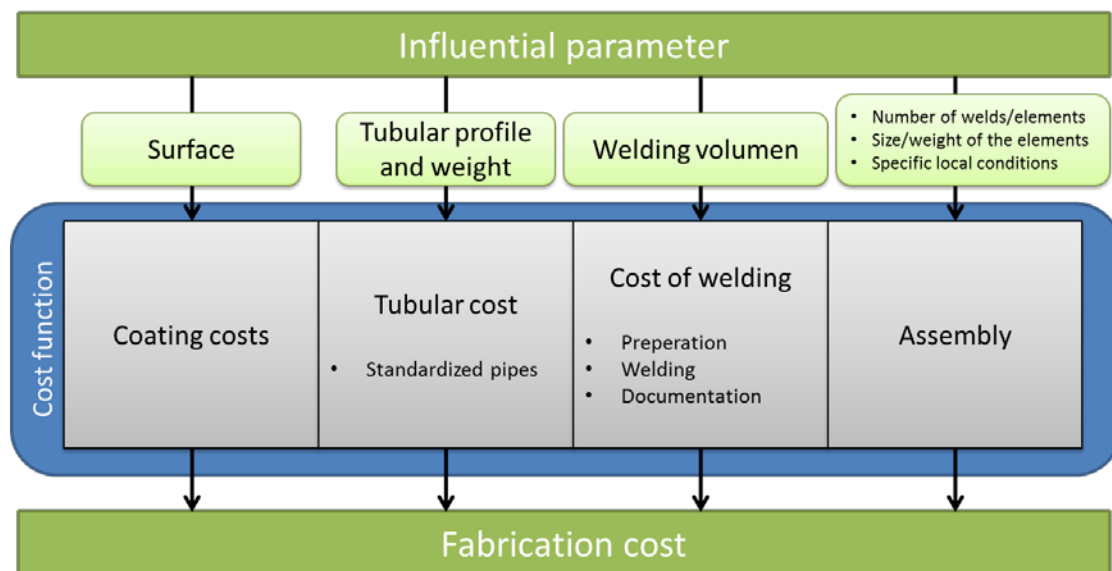


Figure 6.2-1: Structure of the fabrication cost model

#### Costs of tubular members

The costs for tubular members consist of their material and processing costs. Different tubular cross-sections cause different processing costs due to different manufacturing processes, e.g. due to standardized or individual manufacturing. Consequently, each tubular cross-section has a specific cost factor depending on its dimension and manufacturing characteristics. Hence, the tubular cost of each pipe is the product of its weight and a specific cost factor.

#### Coating costs

Coating is for protection from corrosion and depends on the surface area of the jacket. Coating cost is the smallest share of the fabrication costs and remains virtually unchanged by varying the geometrical parameters.

#### Cost of welding

Cost of welding includes the preparation of the welds, the welding, the documentation and the man hours. This cost depends on the welding volume and the welding process. A special distinction must be made between manual and automated welding. Automated welding is less expensive than manual welding, but not every weld can be performed by automated welding. The costs of welding are generally of the same order as the costs for the tubular members. In order to

quantify the welding costs, cost factors are introduced which are multiplied by the volume of the respective weld.

#### **Assembly costs**

Special attention must be paid to the assembly costs. Assembly costs mainly depend on the number of tubular members to be welded. Furthermore there are dependences on the specific local conditions (e.g. size of the assembly hall, location of the assembly hall). The calculation of this cost – which is only indicative - is based on the fabricator's experience.

#### **Assembly strategies**

Assembly strategy describes the assembling in terms of what types of welds are used, the geographical location of assembly and the possibility of pre-assembled elements.

Currently, the construction of jacket structures aims at a weight reduction. Hence, the cross sections of the tubes are as small as possible and thickness transitions are made at tubular joints where utilizations are typically highest. This leads to a lot of different tubular cross-sections and a high number of welds. This assembly strategy is named version A and its main advantage is to be found in the reduction of material costs. Its main drawback can be seen in the fact that the welding and assembly costs are relatively high.

An alternative assembly strategy aims at reducing the number of welds by using the same cross-sections along the whole jacket brace and/or leg. Hence, the mass of the jacket increases while the number of tubular members and the number of welds are decreased.

## 6.2.2 Assembly concepts

This section describes three examples of possible assembly strategies. Furthermore, the share of the four fabrication cost contributors – namely material, welding, coating and assembly costs - is shown based on an example jacket structure.

### Version A

Version A is the classical solution and is aiming at a mass reduction of the jacket. Since the design of jackets is mainly governed by the hot spot stresses at the tubular joints, wall thicknesses of chord cans and brace stubs typically require the highest values. In order to reduce the mass of the structure, the adjoining jacket braces and leg members show reduced wall thicknesses. Consequently, this requires intensive welding effort in order to facilitate this high number of thickness transitions and leads to a high number of members which need to be assembled. Typically, all welds are performed manually at the fabricator's site. Figure 6.2-2 shows 3 different assembly strategies; red pipes indicate a larger wall thickness compared to green pipes.

### Version B

The goal of version B is to reduce the number of welds and the number of tubular members in order to reduce assembly costs. On the other hand, the mass of the jacket increases due to the large wall thicknesses used for the entire members. All welds of the jacket are assumed to be welded manually at the fabricator's site.

### Version C

Version C is designed in a similar manner as version A. The difference is that the tubular joints are assumed to be prefabricated by the manufacturer who is using automated welding techniques which reduces costs compared to manual welding. The other connections between the tubular members are assumed to be manually welded by the fabricator.

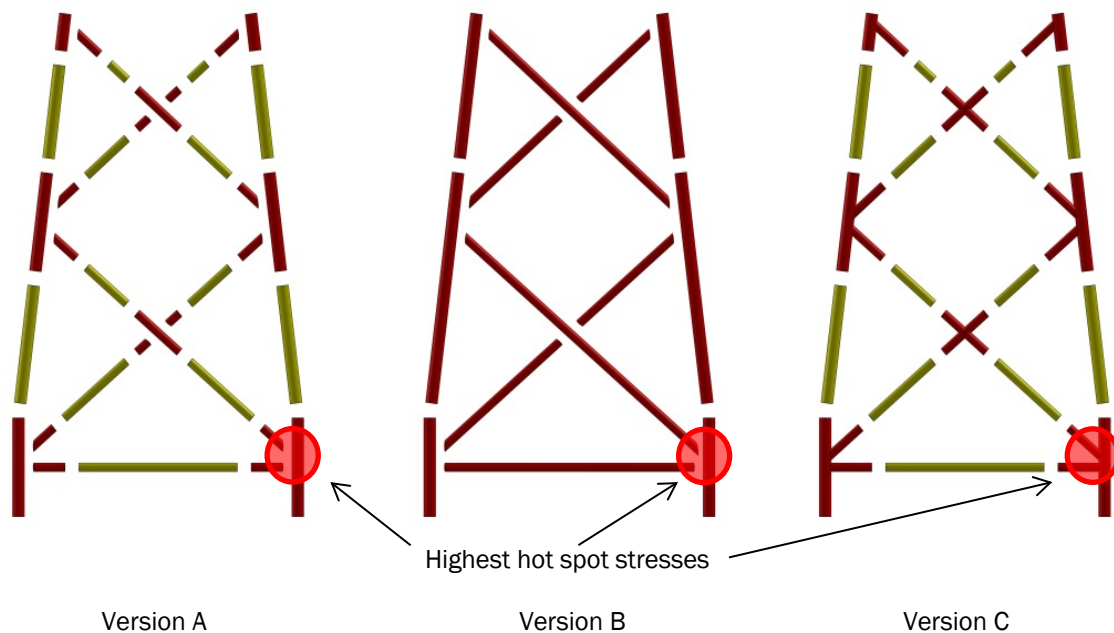


Figure 6.2-2: Three different assembly strategies.

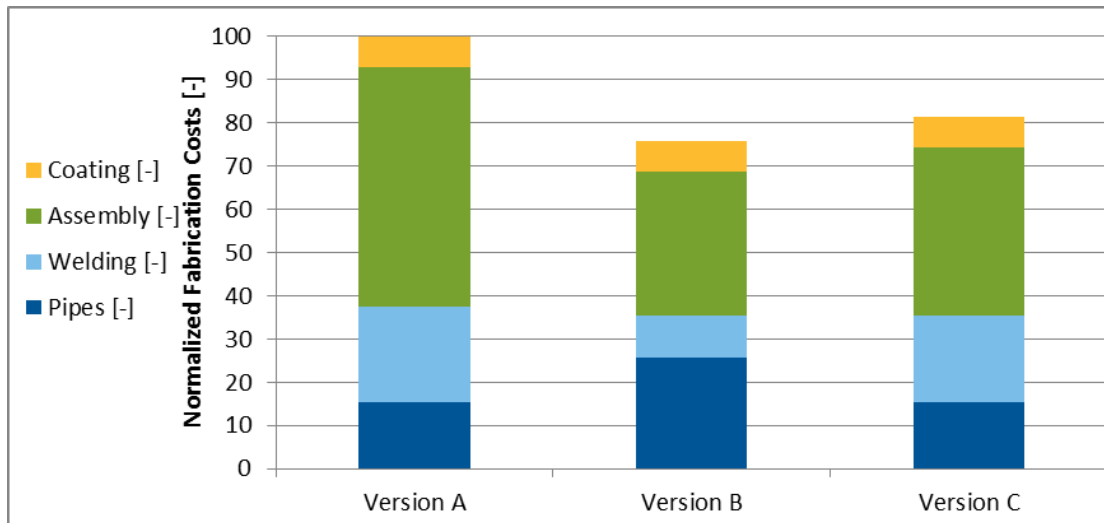


Figure 6.2-3: Fabrication cost distribution caused by different assembly strategies

### 6.2.3 Conclusion

Fabrication costs are mainly composed of the contributors material, welding, assembly and coating cost. The objective of this project is to detect the share of each of these cost drivers by setting up a cost model which enables the designer to find the most cost efficient solution.

From the findings gathered so far, the coating costs seem to be is the smallest share of the fabrication costs. Therefore, the main focus of the fabrication cost minimization is on the material costs, the welding costs and assembly costs. A mass reduction of the jacket does not necessarily lead to a cost optimization since a mass reduction also implies a large number of different cross-sections to be welded. This will raise assembly and welding costs.

In general, it is not possible to minimize all of the cost contributors by choosing one assembly strategy. Chapter 6.2.2 shows the result of the fabrication costs for different assembly strategies. The result shows that the reduction of the number of tubular members and welds (version B) is the less expensive strategy, although this raises the structural mass of the jacket. A further investigation of version B shall clarify how the fatigue behaviour – especially of the braces – is influenced by the increased mass of the tubular members. This might lead to a slightly higher mass than the value shown in Figure 6.2-3.